uOttawa

L'Université canadienne
Canada's university

FACULTÉ DES ÉTUDES SUPÉRIEURES ET POSTOCTORALES

uOttawa

L'Université canadienne
Canada's university

FACULTY OF GRADUATE AND POSDOCTORAL STUDIES

Martin Vachon

AUTEUR DE LA THÈSE / AUTHOR OF THESIS

M.Sc. (Physics)

GRADE / DEGREE

Department of Physics

FACULTÉ, ÉCOLE, DÉPARTEMENT / FACULTY, SCHOOL, DEPARTMENT

Optical Properties of Single Quantum Dots in High Magnetic Field

TITRE DE LA THÈSE / TITLE OF THESIS

Dr. S. Raymond

DIRECTEUR (DIRECTRICE) DE LA THÈSE / THESIS SUPERVISOR

CO-DIRECTEUR (CO-DIRECTRICE) DE LA THÈSE / THESIS CO-SUPERVISOR

EXAMINATEURS (EXAMINATRICES) DE LA THÈSE / THESIS EXAMINERS

Dr. X. Bao

Dr. E. Fortin

Dr. B. Campbell

Gary W. Slater

Le Doyen de la Faculté des études supérieures et postdoctorales / Dean of the Faculty of Graduate and Postdoctoral Studies

OPTICAL PROPERTIES OF SINGLE QUANTUM DOTS IN HIGH MAGNETIC FIELD

Martin Vachon

Thesis submitted to the
Faculty of Graduate and Postdoctoral Studies
In partial fulfillment of the requirements
For the Master of Science degree in physics

Department of Physics
Faculty of Science
University of Ottawa

Your file Votre référence
ISBN: 978-0-494-50929-6
Our file Notre référence
ISBN: 978-0-494-50929-6

This page intentionally left blank.

Table of Contents

Table of Contents iii
Abstract v
Acknowledgements vi
List of Tables and Figures viii
List of Abbreviations x
Legend xi

Chapter I: Introduction 1

Chapter II: Theory 7

2.1 Quantum Dot Structure 8
2.1.1 Material Structure 8
2.1.2 Electronic Structure 13

2.2 Electronic Transitions in Quantum Dots 18
2.2.1 Photon Excitation and Emission 18
2.2.2 Electronic Structure in Magnetic Field 25

Chapter III: Quantum Dot Spectroscopy 32

3.1 Dot Ensemble Photoluminescence 33
3.1.1 Experimental Technique 33
3.1.2 Rapid Thermal Annealing 37
3.1.3 Results and Discussion 38

3.2 Single Dot Photoluminescence 42
3.2.1 Experimental Technique 42
3.2.2 Results and Discussion 45

Chapter IV: Quantum Dot Properties in Magnetic Field 53

4.1 Magneto-Photoluminescence 54

4.1.1 Experimental Technique 54

4.1.2 Ground State Emission 57

4.1.3 Excited State Emission 64

4.2 Spin-Orbit Interaction 74

4.2.1 Spin-Orbit Model 74

4.2.2 Discussion 80

Chapter V: Conclusion 85

Bibliography 88

Appendix A: Images of Magnet Setup 94

Appendix B: Codes for Data Processing 95

Appendix C: Code for Spin-Orbit Model Calculations 97

Abstract

The photoluminescence of quantum dots is studied in a high magnetic field regime where the cyclotron frequency is comparable to the confinement energy. Applying a magnetic field perpendicular to the lateral potential plane lifts the shell degeneracy and magneto-photoluminescence spectroscopy therefore provides a probe to investigate the energy shell structure of quantum dots. By isolating a single quantum dot, the inhomogeneous broadening from a distribution of dot sizes and compositions is eliminated and the fine structure of the spectrum is revealed. The orbital splitting of angular momentum states is shown to follow the Fock-Darwin scheme. However, it is also apparent that each angular momentum branch consists of two distinct lines whose magnetic field evolution cannot be explained by a simple Zeeman spin splitting. The dependence of line splitting on orbital state can be described by the addition of spin-orbit coupling to the Fock-Darwin model. Accordingly, a quantitative measurement of the spin-orbit coupling strength in self-assembled quantum dots is obtained for the first time.

Acknowledgements

This project was undoubtedly difficult to undertake at times, but more importantly it has been a very interesting and enriching experience. As with any challenge in life, the help and support of others is crucial to succeed. To that effect, I would like to first thank my family and friends for their continuous support and encouragement. Despite my unsuccessful attempts to demystify the concepts of quantum mechanics, you have remained interested in discussions about my project. In particular, I thank my parents for all their help and for teaching me the values of hard work and perseverance.

The NRC has provided me with a great learning environment during my studies. This is in large part due to the group of students with which I had the pleasure of sharing the infamous M-50 basement. I would also like to thank the other students and employees who have made the NRC a friendly and pleasant place during my stay. I am particularly grateful to Carolyne for facilitating my arrival at the NRC.

This project would not have been possible without the help of many colleagues and researchers. The samples were grown by Zbig Wasilewski and the post-growth processing was performed by Jean Lapointe, both from the Institute for Microstructural Sciences at the NRC. The RTA technique was taught to me by the annealing expert Carolyne. The magnetic field experiments were performed with the assistance of Adam Babinski. Thanks for all the help Adam. I am also grateful to all the others who helped us with the equipment in Grenoble, and in particular to Marek Potemski for always being very welcoming during my stays at the GHMFL. The work performed at the NRC also required the help of many people. Thanks to all of those who helped me in the lab and all of the technicians who keep things working, in particular Will for all the little jobs you did for me. I am also grateful to Pawel Hawrylak and Marek Korkusinski for the informative discussions.

Last and most importantly, I would like to thank my supervisor Sylvain Raymond. Thanks for taking the time to teach me so much, for being available when I needed help and for doing it all with great enthusiasm. Thanks for giving me the opportunity to travel and to work abroad. Thanks for making this an interesting project and for all your guidance along the way.

List of Tables and Figures

Table

IV-1 Parameters in the SO model. 80

Figure

II-1 Stranski-Krastanow growth of QD. 10

II-2 Profile of a semiconductor sample with a QD layer. 10

II-3 Structure and growth conditions of the 3 wafers fabricated with the objective of performing single dot spectroscopy. 12

II-4 Semiconductor valence and conduction bands. 15

II-5 Vertical confinement in a two-dimensional well layer. 15

II-6 DOS for structures of different dimensionality. 16

II-7 Electronic transitions in a semiconductor with QD potential. 21

II-8 FD model describing the energy states at zero Tesla and the evolution of energy levels in magnetic field. 29

II-9 FD shell notation 29

III-1 Standard PL setup. 34

III-2 PL spectra before and after RTA. 38

III-3 Dot ensemble PL spectra for different excitation powers 39

III-4 Nano mask pattern and optical isolation of a SQD in a nano hole 43

III-5 Micro-PL setup. 45

III-6 PL spectra of many dots and a few dots 46

III-7 PL spectra of a SQD 48

III-8 High resolution SQD PL spectrum at low excitation power 49

III-9 Power dependence of high resolution PL from a SQD. 51

IV-1 M-PL setup. 55

IV-2 Images of piezo-stages and optical fiber setup. 56

IV-3 Magnetic field evolution of the ground state emission from a SQD. 58

IV-4 Effect of magnetic field on the ground state spin. 63

IV-5 High excitation power PL of SQD. 65

IV-6 Waterfalls of high excitation power M-PL spectra 66

IV-7 Contour plot of high excitation power M-PL. 67

IV-8 Medium power PL spectrum of SQD without an external magnetic field. 69

IV-9 Contour plot of M-PL with medium excitation power taken at every 1 T. 70

IV-10 Contour plot of M-PL with medium excitation power taken at every 2 T. 71

IV-11 Power dependence of PL from a SQD in magnetic field 73

IV-12 Calculated and experimental QD emission energy in magnetic field. 81

IV-13 Theoretical evolution of the QD emission energy in magnetic field showing the effect of adding SO coupling to the FD model. 82

IV-14 Intensity of QD emission from theoretical calculations including many-body effects. 83

List of Abbreviations

AFM – atomic force microscopy

BP – band-pass

BIA – bulk inversion asymmetry

CCD – charge-coupled device

DOS – density of states

FD – Fock-Darwin

LWP – long-wave-pass

LA – longitudinal acoustic (phonon)

LO – longitudinal optical (phonon)

M-PL – magneto-photoluminescence

Micro-PL – micro-photoluminescence

PL – photoluminescence

QD – quantum dot

RTA – rapid thermal annealing

SAQD – self-assembled quantum dot

SI – semi-insulating

SWP – short-wave-pass

SQD – single quantum dot

SO – spin-orbit

SIA – structure inversion asymmetry

WL – wetting layer

Legend

$u_{\vec{k}}(\vec{r})$ – Bloch function

ω_c – cyclotron frequency

δ – dot deformation ratio

λ_D – Dresselhaus SO strength

g^* – effective g-factor

m^* – effective mass

E_c – energy at the bottom of the conduction band

E_v – energy at the top of the valence band

E_g – energy gap

M – exciton spin projection

Ω – Fock-Darwin oscillator frequency

g – g-factor

H – Hamiltonian

ω_0 – harmonic oscillator frequency

B – magnetic field

$\vec{\mu}$ – magnetic moment

E_0 – offset energy

l – orbital angular momentum from atomic orbitals

L – orbital angular momentum from QD orbitals

λ_R – Rashba SO strength

σ – spin angular momentum

J – total angular momentum from spin and atomic orbitals

Ψ – wavefunction

k – wavenumber

$\vec{k}$ – wavevector

Chapter I: Introduction

The ever growing need for more powerful computers and for transmitting and storing information requires the constant development of smaller and faster optoelectronic devices. Over the past few decades, computer performance has grown at an amazing rate. As described by Moore's Law [1], performance has roughly doubled every couple of years. The advances are essentially due to the miniaturization of circuit components which makes it possible to integrate more of them into a single microchip, thus increasing the computational power. However, the miniaturization process is now reaching a limit.[2-4] For one, there is a technological limit as power dissipation, design complexity and tunnelling currents become an issue, but there is also a physical limit as quantum mechanical effects are manifested and classical analysis is no longer valid. In fact, dimensions of only a few hundred nanometres and switching charges containing 1000 or less electrons are already found in today's state-of-the-art components.[2] Further miniaturization to the scale of tens of nanometres would alter the electronic properties of the components as quantum size effects come into play. Hence, device technology will soon reach a quantum threshold below which components will cease to function in the same manner. Although components can be redesigned to work with quantum effects, further progress will eventually require an alternative technology whose components will be based on quantum effects rather than being designed to work despite of them. One of the most promising candidates for use in nanometre-scale computer devices is quantum dot (QD) technology.

In fact, the potential of QD structures for a range of nanotechnology applications has motivated considerable research on their fundamental properties. QDs are built using a variety of techniques and materials. However, they can all be defined as a low potential region surrounded by a region of higher potential. The particles inside the QD are therefore trapped in all directions by a potential barrier. Since the size of the structure is comparable with the de Broglie wavelength,

quantum phenomena emerge and the material properties are changed dramatically. The QD material exhibits characteristics which are not found in the same substance at the micro or macro scales. One of the fundamental properties of QD structures is the quantization of energy. As such, only discrete energy states can be occupied by the trapped particles, giving QDs unique transport and optical properties compared to larger structures. Another important feature of QDs is that they can be engineered by controlling the geometrical size, shape, and the strength of the confinement potential. Furthermore, QDs are scalable, which is important from a technological point of view. Because of their advantageous characteristics, their scalability and the ability to tune their properties, QDs are expected to provide the basis for future generations of device technologies. On the other hand, the physics of QDs shows many parallels with the behaviour of naturally occurring quantum systems in atomic and nuclear physics. Unlike these systems however, QDs are fabricated nanostructures which can be controlled, and their optical and transport properties can be readily measured. Therefore, QDs are not only promising candidates for many applications, but they're also a good venue for studying the physics of confined carriers and many-body effects.

Initially, studies of QD systems were motivated by possible improvements to already used devices such as semiconductor lasers and amplifiers. In fact, the concept of quantum confinement in semiconductor heterostructures was first introduced in the early 1970s when R. Dingle and C. H. Henry [5] realized the advantages of using quantum wells as the active layer in semiconductor lasers. Even greater benefits were subsequently predicted for lasers with QD active layers [6,7], such as lower threshold current, less temperature dependence and very narrow gain spectrum. Nowadays, almost all commercial laser diodes use quantum wells as the active layer. Just as the efficiency of quantum wells required improvements in growth techniques and structure design, the full promise of QDs must await further progress in the understanding of material growth, confinement potential and carrier dynamics.

Today, QDs have proven to offer much more potential than improvements to lasers and amplifiers. The scope of QD uses has actually broadened to include applications which were not even conceived a few decades ago. In fact, QDs could lead to novel device applications in fields such as optics and optoelectronics, but also quantum cryptography, quantum computing and even biophysics as they offer improved brightness and stability compared to the traditional organic dyes currently used as biological sensors. QDs can be used either as a source of single photons or entangled photons for quantum cryptography, a technique that enables two parties to securely produce a key for encryption and decryption of messages. A first quantum cryptography protocol using the polarization of single photons was proposed by C. H. Bennett and G. Brassard [8] in 1984. Under this scheme, the information is encoded in non-orthogonal states using two conjugate pairs of states, usually the rectilinear and diagonal polarization states of light. Each pair of orthogonal states is used as a basis to send bits of information. If the basis is chosen randomly, the receiver cannot distinguish between the 4 possible states as they are not all orthogonal. The receiver must chose a basis and only the bits which are sent using that basis will be measured correctly. The states which are received in the other basis will randomly return a state in the measured basis. Once all information is sent, the sender and receiver can communicate to each other the basis with which each photon was sent and measured. The bits of information which used a different basis are discarded, leaving a shared key that can be used to encrypt and decrypt messages which are then transmitted over a standard communication channel. However, if a third party has gained any information about the photons, the act of measurement will have disturbed the state according to the Heisenberg uncertainty principle, and errors will be introduced in the receiver's measurements. Therefore, any eavesdropping will be detected and quantum cryptography can guarantee secure communication. A second proposal [9] uses the correlation between the polarizations of a pair of entangled photons. Even if the photons are in different locations, the measurement of one photon will give the ability to deduce the polarization of the other photon. However, if one of the photons is previously measured by a third party, the correlations will weaken and

eavesdropping will be detected. Today, the idea of quantum cryptography has been successfully implemented and there are currently three companies offering commercial systems. The concept of entanglement is also utilized in quantum computers, in which the algorithmic computation is based on quantum mechanics.[10,11] However, a first generation of quantum computers will more likely have classical algorithms and information processing based on components that behave according to quantum mechanics. To this end, both the charge and spin of carriers in QDs can be used as quantum bits in quantum information processing.[12,13] While the carrier charge may offer easy coherent manipulation [14-16], the spin state has a longer coherence time due to its insensitivity to electronic noise. In view of that and other advantages such as miniaturization and reduced power consumption, the quantum spin state has provided the basis for the new emerging technology of spin-based electronics, also known as spintronics.[17] The birth of spintronics is considered to be the discovery of giant magnetoresistance, an effect which is used to read data on compact hard disks. In recent years, the technology lead to a drastic miniaturization of hard disks such as those used in laptops and music players. The very weak magnetic areas used to store information on disks can now give rise to a major difference in electrical resistance, which is then converted into a change in the electrical current emitted by the read-out head. The effect was independently discovered in 1988 by A. Fert and P. Grünberg, who were both awarded the Nobel Prize in Physics in October 2007.[18]

Therefore, QD carriers have a spin degree of freedom which can be exploited in device applications. In order to exploit the spin state, one must be able to change or influence it through various mechanisms. Among these is the interaction between the orbital angular momentum and the spin angular momentum of the particle, which is known as the spin-orbit (SO) interaction or SO coupling. Possible devices to control and manipulate spin states include prominently the Datta-Das proposal [19] for a spin-field-effect transistor. This device is based on the energy splitting between spin-up and spin-down states which occurs in the absence

of any external magnetic field as the result of SO interaction. It would accordingly exploit the fact that the electron spin can be manipulated by an external electric field through the Rashba [20] SO interaction. A more recent proposal exploits both the Rashba and Dresselhaus [21] coupling by tuning the Rashba SO intensity via gate voltages such that both coupling terms have equal strengths, effectively cancelling each other out. The electron spin is then independent of its angular momentum and the transistor is not affected by scattering to different states. This therefore allows one to build a diffusive version of the transistor.[22] The basic understanding of QD properties is necessary in order to fully exploit their application potential. In particular, all SO effects must be understood for full control of spin-flip mechanisms. While the effects of SO interaction on the electronic properties of quantum wells and quantum wires has been extensively studied theoretically [23,24] and experimentally [25-27], investigations of SO interaction in QD systems have only received notable interest in recent years [28-30] due to the emerging field of spintronics. In addition, the SO interaction was only studied in electrostatic QDs. Although these systems are interesting for research purposes, the true potential of QD structures more likely lies in self-assembled quantum dots (SAQDs). In fact, the smaller size of SAQDs results in a stronger confinement potential and these systems can still operate at room temperature. They can also be easily fabricated in large numbers, contrarily to electrostatic QDs which require post-growth processing. Finally, SAQDs are durable, which is technologically important as it allows applications to have a long life.

In view of that, this project aims to advance knowledge on the fundamental properties of SAQDs. To this effect, the basic concepts and models required to understand and interpret the experimental results are first introduced in chapter II. The experimental techniques which were used to study the energy structure of the QDs are then presented in chapter III along with measurement results. In particular, measurements were performed on a single quantum dot (SQD). In previous studies of large ensembles of QDs [31], the inhomogeneous distribution of dot sizes and compositions produced a considerable broadening which prevents the observation

of more subtle effects. As a result, an important goal of the project is to eliminate this inhomogeneous broadening by isolating a SQD. Furthermore, an emphasis will be put on the study of excited states. Previous studies of SQDs in magnetic field focused on the ground state. However, the excited states have different angular momentum and SO coupling can thus be revealed. Finally, the measurements in magnetic field are presented in chapter IV. By studying the energy spectrum in magnetic field, it is possible to analyse the energy shell structure of QDs as the magnetic field lifts the degeneracy of states. Similar studies were recently published for magnetic fields up to 14 T [32] and 20 T [33], but for the first time, experiments were carried out to measure the photoluminescence (PL) of the excited states of a single SAQD in magnetic fields up to 26 T. By doing so, it was possible to observe effects which have never before been reported. In fact, a quantitative measurement of the SO coupling strength in SAQDs is obtained for the first time.

Chapter II: Theory

A QD can be generally defined as a region of semiconductor material with a low electronic potential compared to the surrounding material. By reducing the size of this region to nanostructure dimensions, the motion of confined particles becomes restricted. Since the electronic confinement is in all three dimensions, the envelope wavefunctions of the particles are completely localized and QDs are thus referred to as zero dimensional structures. Another well-known potential that confines particles in all three dimensions is the Coulomb potential of atoms. In fact, the physics of QDs shows many parallels with the naturally occurring quantum systems of atoms. As such, QDs are also known as artificial atoms. In both systems, the confined particles only have access to discrete energy states. However, the confinement potential of QDs does not necessarily have spherical symmetry and the confined particles do not move in free space, but rather in a semiconductor material.

This chapter will present the concepts and the models required to understand and interpret the experimental results of the subsequent chapters. First, a description of the growth process will be presented along with the electronic properties of the resulting QD. The energy structure of the QD can be readily analyzed using optical spectroscopy. As a consequence, the processes involved during such an experiment will be examined. In particular, more consideration will be given to the transition energies in photon emission processes. Finally, a model will be derived to explain the energy spectrum of QDs in magnetic field.

2.1 Quantum Dot Structure

The confinement of charged particles within a semiconductor nanostructure can be induced by a material interface, by electrostatic potentials, or by a combination of both. In lithographically defined QDs, a thin quantum well layer provides the confinement along the growth direction while the lateral confinement is provided by an electrostatistically induced potential barrier. In this project, the carriers are confined in all three dimensions by the interface between different materials. Unlike lithographically defined QDs, these nanostructures can be easily fabricated as they form spontaneously during the epitaxial growth process. In order to understand the origin of the confinement potential in these self-assembled structures, one must consider the band theory of solids. In this section, the mechanisms involved during the self-assembled growth will be explained and the electronic properties of the resulting structure will be described.

2.1.1 Material Structure

The samples studied in this project were grown by molecular-beam epitaxy, a technique in which the elements are randomly deposited onto a crystalline substrate to form thin epitaxial layers.[34,35] The InAs/GaAs QD samples are said to be made of III-V type semiconductors since all elements are from the group III or V. The group III elements (gallium and indium) are thermally evaporated from elemental sources and deposited in the form of molecular beams. The cell temperature of each element can be adjusted to produce the desired molecular beam flux and a shutter can prevent the beam from reaching the substrate. As for the group V element arsenic, it is present in a gaseous form in the growth environment and it binds with the group III elements as they are deposited onto the substrate.

The investigated QDs were formed spontaneously during the growth process. In epitaxial growth, the substrate initially acts as a seed crystal for the

deposited material. As such, atoms will assemble in a very ordered manner and the deposited layer will take on a lattice constant and orientation identical to those of the substrate. This ordered growth will occur as long as the deposited material has a lattice constant similar to that of the underlying layer. A heterostructure can therefore be formed by varying the material during the growth. Depending on the growth kinetics, the interface energies and the lattice mismatch, three different modes are frequently encountered during such a heteroepitaxial growth: a layer-by-layer growth (Frank-van der Merwe), island growth (Volmer-Weber) or layer-by-layer plus islands (Stranski-Krastanow).[36] A thermodynamic criterion for the growth mode was developed by Bauer.[37] The criterion states that, under equilibrium conditions, the growth mode is determined by the following energy difference :

$$\Delta\sigma = \sigma_f + \sigma_i - \sigma_s \qquad \text{II-1}$$

where σ_s is the surface free energy of the substrate (or underlying film), σ_i is the free energy of the interface and σ_f is the surface free energy of the deposited film. If $\Delta\sigma \leq 0$, the adatoms are more strongly bound to the substrate than to each other and the film tends to wet the substrate in order to minimize the total energy. Such a condition will consequently result in a complete wetting of the substrate and a layer-by-layer growth will occur. If $\Delta\sigma > 0$, the adatoms are more strongly bound to each other than to the substrate and island growth is favourable. When there is a lattice mismatch between the materials, the film free energy will have a contribution from the strain energy, which increases with film thickness. It is thus possible for $\Delta\sigma$ to be negative until a critical thickness is reached and then positive above this coverage. Such a condition will result in layer-by-layer plus islands growth. A schematic representation of the Stranski-Krastanow growth process is illustrated in Figure II-1. The InAs material has a longer lattice constant than the GaAs material on which it is deposited. For the first layer, the total energy is minimized by wetting the GaAs surface. As the InAs layer becomes thicker, a large strain energy is accumulated and the system can lower its energy by forming isolated islands in

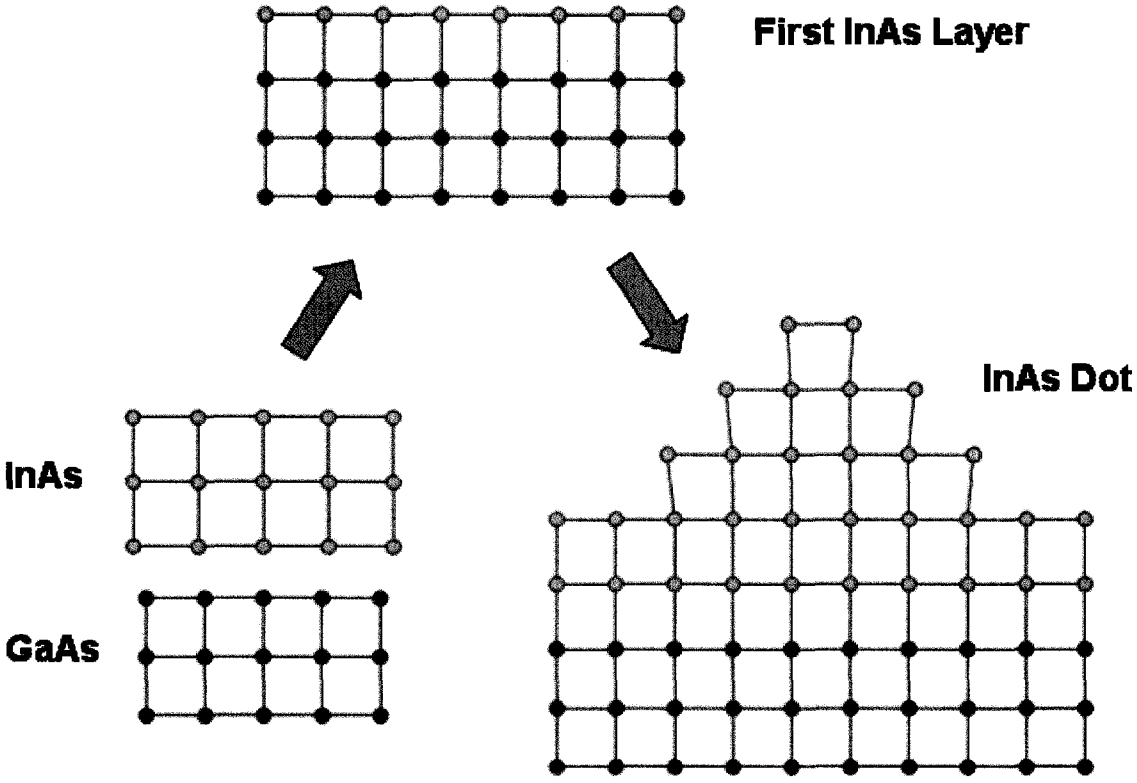

Figure II-1 Stranski-Krastanow growth of QD. The initial growth mode is layer-by-layer, but when enough strain energy is accumulated, the InAs material forms isolated islands in which the strain is relaxed.

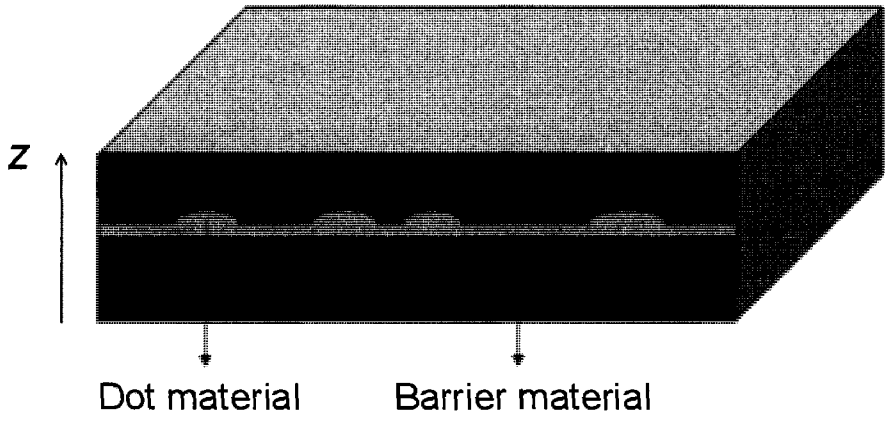

Figure II-2 Profile of a semiconductor sample with a QD layer. The dots can vary in size and composition, with typical dimensions having a height of ~5 nm and a base diameter of ~25 nm.

which the strain is relaxed. The InAs is subsequently covered by more GaAs material. As shown in Figure II-2, the Stranski-Krastanow growth process results in a thin InAs quantum well from the two-dimensional wetting layer (WL), while the islands form the InAs QDs. The strain relaxed islands initially have a lens shape. However, the upper layers of the dots are removed during an indium flush process [38] and the resulting dots have a flat disk shape. This process is once again a manifestation of the interplay between the different interface and strain energies. Once the islands are completely formed, they are partially capped with a thin GaAs film. Since the top of the islands has relaxed to match the InAs lattice constant, that surface is not energetically favourable for GaAs, and the film will accordingly form around the islands. In this material distribution, the InAs islands are also not in an energetically favourable structure. In fact, the InAs deposition followed a Stranski-Krastanow growth mode, which implies that island formation minimizes the total energy only once the WL has accumulated enough strain energy. Since the islands are now surrounded by a GaAs film, it is actually favourable for the indium to migrate on top of the GaAs film to form a partial WL. The InAs material remaining in the island structure is now expected to have a lateral lattice constant nearly equal to GaAs, and the overgrowth of the disk with GaAs can now happen. Finally, the surface indium can be desorbed by increasing the substrate temperature and additional GaAs can be deposited in order to complete the capping.

In view of the objective to isolate a SQD for spectroscopic measurements, 3 wafers were grown with the intention of obtaining a low dot density. The details of the structures and their growth conditions are described in Figure II-3. All of the wafers have a semi-insulating (SI) GaAs substrate on which a 200 nm undoped GaAs buffer layer was deposited and annealed at 630 °C for 300 sec. The temperature was then lowered to 490 °C for the growth of the InAs dot layer. For the V0250 wafer, an additional 5 nm of GaAs was deposited on the buffer layer at the InAs growth temperature. With the same molecular beam flux of indium, the deposition time was 27.5 sec for V0246 and 27.0 sec for both V0249 and V0250. The height of the dots was controlled by an indium flush at 5 nm and the dot layer

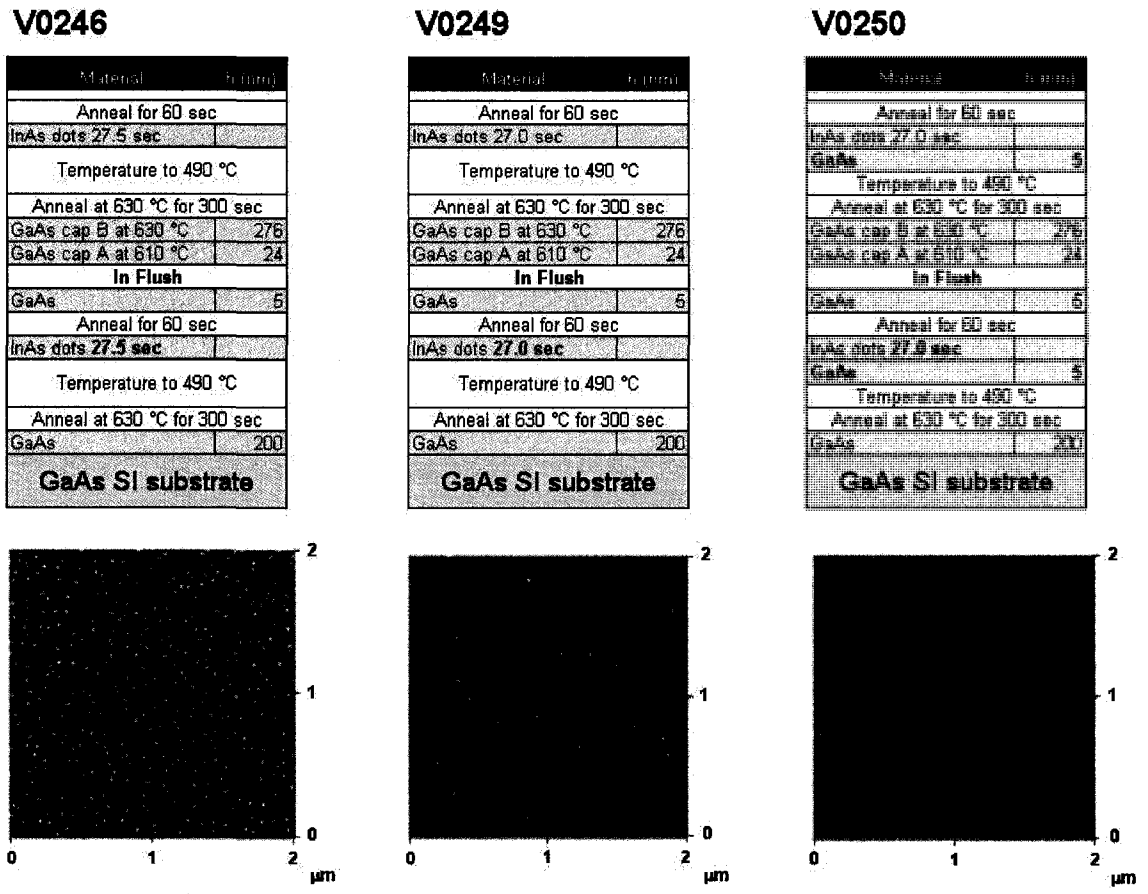

Figure II-3 Structure and growth conditions of the 3 wafers fabricated with the objective of performing single dot spectroscopy. The 2x2 µm AFM images reveal that the V0246 wafer has the highest dot density while the V0250 wafer has a low dot density which is propitious for the isolation of a single dot.

was capped with a 300 nm GaAs layer. For atomic force microscopy (AFM) measurements, another uncapped QD layer was subsequently deposited on each wafer. Since this surface dot layer is grown under the same conditions, the AFM images illustrated in Figure II-3 provide an estimate to the dot density in the active layer. It is therefore apparent that the V0246 wafer has the highest dot density. Since the dot layer growth time was slightly longer for that wafer, more dot material was deposited which consequently lead to the formation of more dots. The AFM images also suggest that the additional growth of a GaAs buffer layer at the dot growth temperature results in the formation of fewer dots. In fact, the measurements on the surface dot layer indicate that the V0250 wafer has the lowest dot density.

Although samples from all three wafers were studied, the longer dot spacing of V0250 make it more propitious for the isolation of a single dot and the results presented hereafter are thus from that wafer.

2.1.2 Electronic Structure

In a single isolated atom, the electrons occupy atomic orbitals which form a discrete set of energy levels. When atoms are grouped together to form a solid, the outer shell electrons behave as nearly free particles who all share the entire bulk space. As a consequence of the Pauli exclusion principle, the atomic orbitals must split into enough discrete energy levels to hold all electrons. These energy levels are very close together and they form bands of energy which have a near continuum of allowed energies for the electrons. However, electrons cannot occupy any energy level in the solid. In fact, the energy bands are separated by forbidden regions called band gaps, and the energy gap between the highest filled band and the lowest empty band is denoted by E_g. A pure semiconductor at absolute zero has a valence band which is completely filled and it behaves as an insulator. It becomes a conductor if impurities are present or if electrons are excited into the conduction band.

In the nearly free electron model, the electrons are treated as being only weakly perturbed by the periodic potential of the ion cores.[39] The wavefunction of an electron inside the solid is therefore the plane wave of a free particle, but modulated by a Bloch function $u_{\vec{k}}(\vec{r})$ which has the periodicity of the crystal potential. The Bloch functions also carry the atomic part of the wavefunction. For III-V semiconductors, the valence band is formed from p-shell atomic orbitals and $u_{\vec{k}}(\vec{r})$ therefore carries a p-type symmetry, while s-shell atomic orbitals split into the conduction band and $u_{\vec{k}}(\vec{r})$ then carries an s-type symmetry. The Bloch theorem states that the solutions of the Schrödinger equation for a periodic potential must have the form:

$$\Psi_{\vec{k}}(\vec{r}) = u_{\vec{k}}(\vec{r})\, e^{i\vec{k}\cdot\vec{r}} \qquad \text{II-2}$$

where $\vec{k}$ is the particle wavevector. The dispersion relation between the energy E and the wavenumber k depends on the electron-ion interactions. However, III-V semiconductors have a direct energy gap and the particles which must be considered during optical processes are at the top of the valence band and at the bottom of the conduction band. Near those $k = 0$ extrema, the dispersion relation is approximately parabolic and the energy is given by:

$$E = E_{v,c} + \frac{\hbar^2 k^2}{2m^*} \qquad \text{II-3}$$

where $E_{v,c}$ is the energy at the top (bottom) of the valence (conduction) band and m^* is the effective mass of the particle. In this approximation, electrons can be treated as free particles for which the mass has been altered by the effect of the periodic potential. Figure II-4 illustrates the band structure of a semiconductor in terms of the parabolic dispersion relation of the effective mass model and an energy band diagram. It turns out that the effective mass of an electron near the top of the valence band is negative. Since the valence band is nearly full, it is more convenient to treat it by viewing the empty states at the top of the band as being occupied by holes, with positive effective mass and charge. From this point on, the electronic structure will be discussed in terms of both types of charge carriers: valence band holes and conduction band electrons.

When a thin layer of a semiconductor material is embedded in between another semiconductor material that has a larger energy gap, the charge carriers in the middle layer are confined between energy barriers that result from the difference in energy gaps. The middle layer therefore acts as a potential well. Once the charge carriers are captured in the well layer, the probability to escape is limited by the height of the barriers. If the thickness of the well layer is made to be only a few

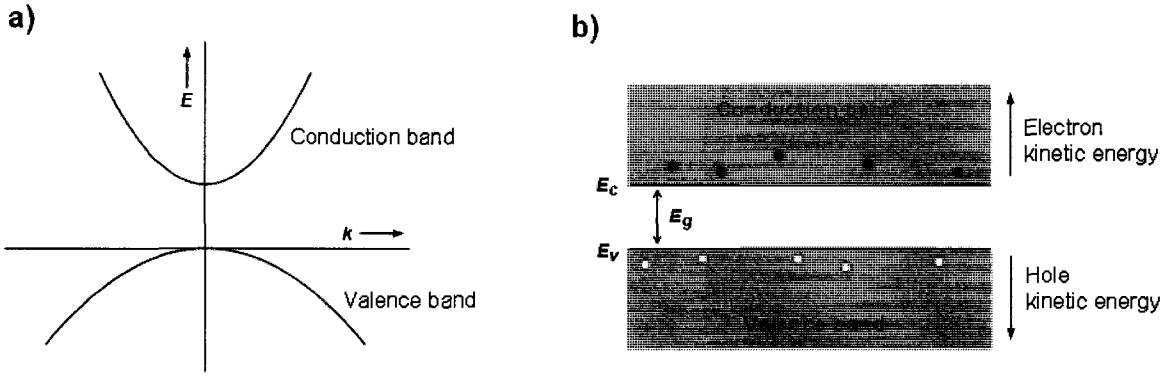

Figure II-4 Semiconductor valence and conduction bands represented by a) the parabolic dispersion relation of the effective mass model and b) an energy band diagram.

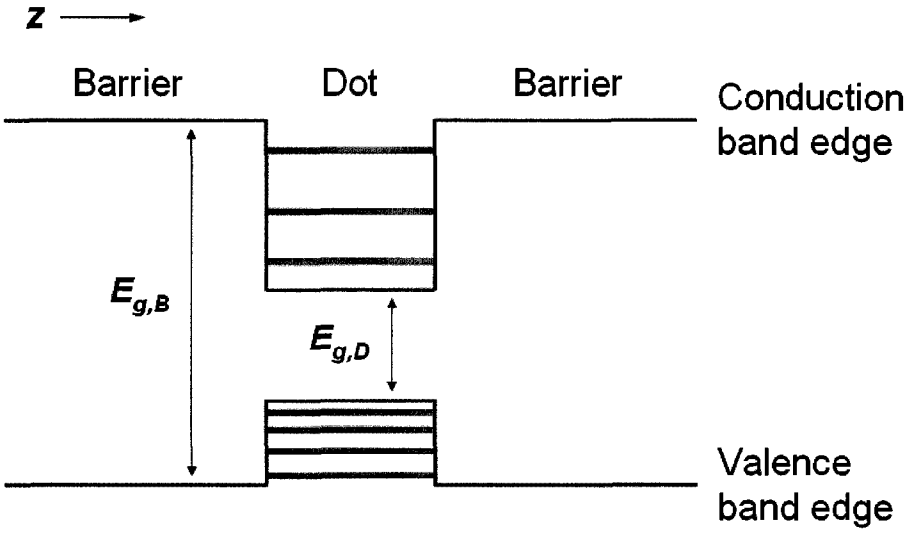

Figure II-5 Vertical confinement in a two-dimensional well layer. The charge carriers have allowed energy sub-bands inside the well potential as a result of the narrow confinement.

atomic layers, the movement of charge carriers is then restricted to a two-dimensional plane. The available energies are thus quantized inside the well, similarly to a particle inside a one-dimensional potential well. As shown in Figure II-5, the quantization results in sub-bands with energies that depend on the height and width of the well. Since the carriers are free to move in the two unconfined

dimensions, there is formation of narrow energy sub-bands rather than discrete energy levels as in the case of the one-dimensional potential well.

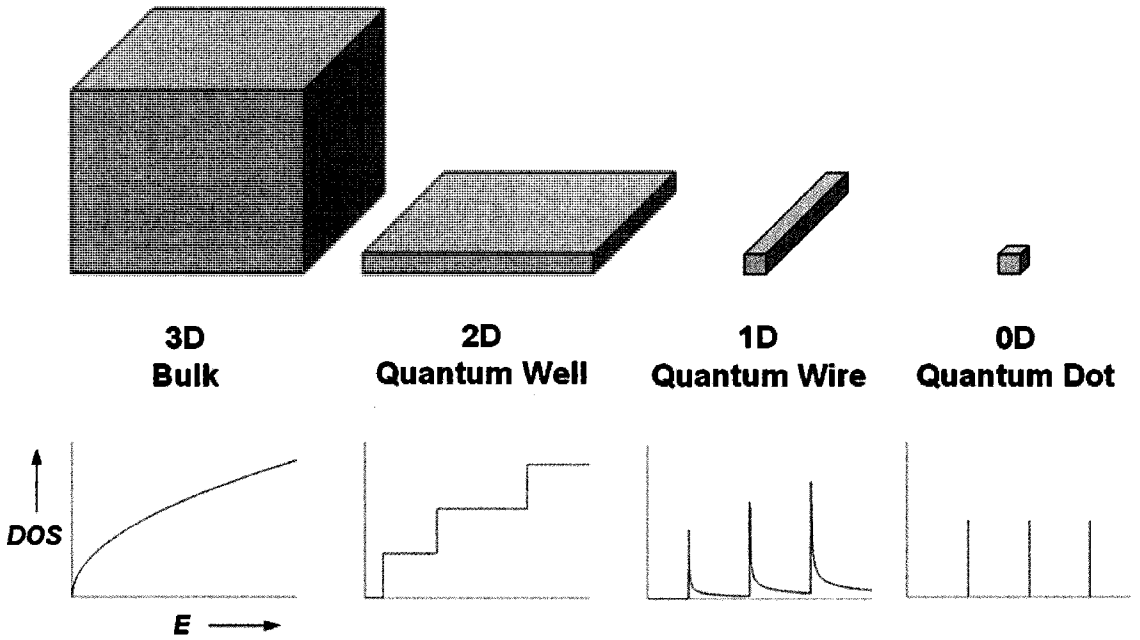

Figure II-6 DOS for structures of different dimensionality. The DOS becomes progressively more discontinuous as the dimensionality decreases, with zero-dimensional structures having a delta-like function.

The quantum well model illustrates how confinement in one dimension affects the energies which are available to a particle. Further confinement restricts the particle motion even more and, as a result, fewer energies are accessible. The effect of particle confinement in semiconductor structures can be described through the concept of density of states (DOS), which defines the number of states available per unit energy. Figure II-6 shows the shape of the DOS as the dimensionality of the structure is reduced. In a bulk semiconductor, the DOS is continuous and increases monotonously. If one of the dimensions is confined, the DOS becomes a step function. For a quantum wire structure, the DOS decreases as $E^{-1/2}$ instead of being continuous between energy steps. In a zero-dimensional structure, the momentum is quantized in all directions and the available states exist only at

discrete energies. The DOS is accordingly represented by a delta-like function. The conclusion that the DOS becomes progressively more discontinuous as the dimensionality decreases is independent of the structure's shape. In fact, zero-dimensional structures of any shape will have discrete energy levels.

2.2 Electronic Transitions in Quantum Dots

In order to gain information on the electronic properties of QDs, one must be able to probe their electronic structure. The interaction of light with matter provides a way to investigate the energy levels within the QD potential. In fact, charge carriers can make transitions between states by interacting with the electro-magnetic field, either by gaining energy through photon absorption or by converting energy into emitted photons. The spectroscopic technique by which light is utilised in such a way will be explained in the next chapter. In this section, the electronic processes involved in photon absorption and emission will be described. Starting with the excitation of charge carriers, a series of radiative and non-radiative processes occur prior to the occupation of QD levels. Once the carriers have relaxed within the QD potential, they have a certain probability of recombining radiatively, with the energy of the emitted photons providing information with respect to the electronic structure of the QD. When analysing the energy spectrum of the emitted photons, one must consider that the transition energies can be altered in various ways. When other particles are present in the QD potential, the transition energies are changed as a result of many-body effects. Another way to modify the transition energies is by applying an external magnetic field. In fact, the energy levels are strongly shifted by the presence of a magnetic field, and studying the electronic structure of QDs in field provides additional information. For instance, the degeneracy of states is lifted and the energy shell structure is revealed. A solution to the confined energy states within the QD potential will be derived, with the resulting Fock-Darwin (FD) spectrum giving a description of the evolution of energy levels in magnetic field.

2.2.1 Photon Excitation and Emission

At low temperature, electrons cannot acquire enough thermal energy to be excited above the energy gap. As a result, the conduction band of a pure

semiconductor is empty as the electrons remain in the completely filled valence band. In order to excite electrons into the conduction band, one must provide energy to the system. One way of achieving this is to shed light onto the semiconductor. When photons are absorbed by electrons, they are converted into energy which is transferred to the electron. The optical excitation can be either resonant or non-resonant. With a resonant excitation, the wavelength of the incident photons corresponds to the energy needed to excite carriers directly into QD states and the carriers occupy a specific state immediately after absorbing the photon. With non-resonant excitation, the carriers are excited into an energy continuum above the discrete energy levels of the QD. As such, they are promoted either to the quantum well sub-band of the WL or to the conduction band of the bulk material.

When electrons are excited into the conduction band, they leave an unoccupied state in the nearly filled valence band. The quantization of these hole states in the QD potential is more complicated than electron states as a consequence of the nature of the atomic orbitals forming the bands. The conduction band is formed from s-type orbitals ($l=0$) which do not contribute any angular momentum. On the other hand, the valence band originates from the bounding of p-type orbitals ($l=1$) which have non-zero orbital angular momentum. As a result, there are actually three different valence bands. In the absence of SO coupling, these bands are degenerate at $k=0$. Taking into account the twofold spin degeneracy of the charge carriers, the valence band would accordingly have a sixfold degeneracy. However, SO coupling occurs in all bulk III-V semiconductors [40] and the degeneracy is lifted. This bulk SO coupling originates from the crystal's lack of inversion symmetry, and is often referred to as the Dresselhaus SO coupling. In this case, a description of the hole states can be given in terms of the Kane model [40,41] which uses a basis of states near $k=0$ to resolve the Schrödinger equation of particles in the semiconductor. The states which form this new basis are the eigenstates of the total angular momentum operator $J=l+\sigma$ (where l is the orbital angular momentum and σ is the particle's intrinsic angular momentum) and its projection operator J_z along the growth axis. The conduction

and valence band states can accordingly be defined in terms of these quantum numbers. As such, the addition of $l=0$ and $\sigma=\frac{1}{2}$ can only give $J=\frac{1}{2}$, and the conduction band is consequently twofold degenerate with $J_z=\pm\frac{1}{2}$. For the valence band, $l=1$ and $\sigma=\frac{1}{2}$ results in the two possible values $J=\frac{1}{2}$ and $J=\frac{3}{2}$. Moreover, $J=\frac{3}{2}$ is fourfold degenerate with projection values $J_z=\pm\frac{1}{2},\pm\frac{3}{2}$. The dispersion relation of the $|J,J_z\rangle$ hole states depends on the magnitude of the angular momentum projection. In fact, the curvature of the dispersion relation is less pronounced for the $J_z=\pm\frac{3}{2}$ states, and the $|\frac{3}{2},\pm\frac{3}{2}\rangle$ states are accordingly associated to the heavy hole band while the $|\frac{3}{2},\pm\frac{1}{2}\rangle$ are associated to the light hole band. Although these states are normally degenerate at $k=0$, the presence of strain in the QD material lifts the degeneracy of the light and heavy hole valence bands.[42] In III-V semiconductors, the split-off band with the $|\frac{1}{2},\pm\frac{1}{2}\rangle$ states is always lower in energy than the other valence bands and it does not contribute to radiative recombination of electron-hole pairs. The split-off band will therefore not be given further consideration beyond this point. Moreover, the hole occupies the heavy hole state at low temperature and, unless otherwise noted, a hole state will hereafter refer to the heavy hole state.

Now that the hole states have been explained, the electronic transitions between the different states can be described. Figure II-7 illustrates the processes involved when charge carriers are optically excited non-resonantly. As the electron is excited to the conduction band, it leaves a hole in the valence band and an electron-hole pair is created. Since the hole carries a positive charge, the electron is attracted to it by the Coulomb force. As a result, the electron effectively binds to the hole forming a quasiparticle known as an exciton, which has slightly less energy than the unbound electron and hole. At low temperature (when kT is less than the exciton binding energy), the electron-hole pair remains bound as the exciton propagates in the material. If the incident photon energy is greater than the energy

gap of the barrier material, the charge carriers will be excited into the energy continuum of the bulk material. The excitons will then lose energy as they propagate arbitrarily in the sample. This energy relaxation occurs as a result of various mechanisms such as inelastic collisions with other particles as well as emission of phonons and photons. Since the excitons are occupying a continuum of energy states in the bulk material, there are many direct and indirect processes through which the exciton can lose energy and the excitons can rapidly relax into the QD potential, either via the WL continuum or not. Once the excitons occupy the QD states, they can still make transitions to lower energy states through the same relaxation mechanisms. However, the excitons now have a limited number of available states which restricts the possible processes. These intra-band transitions will now be discussed in more detail.

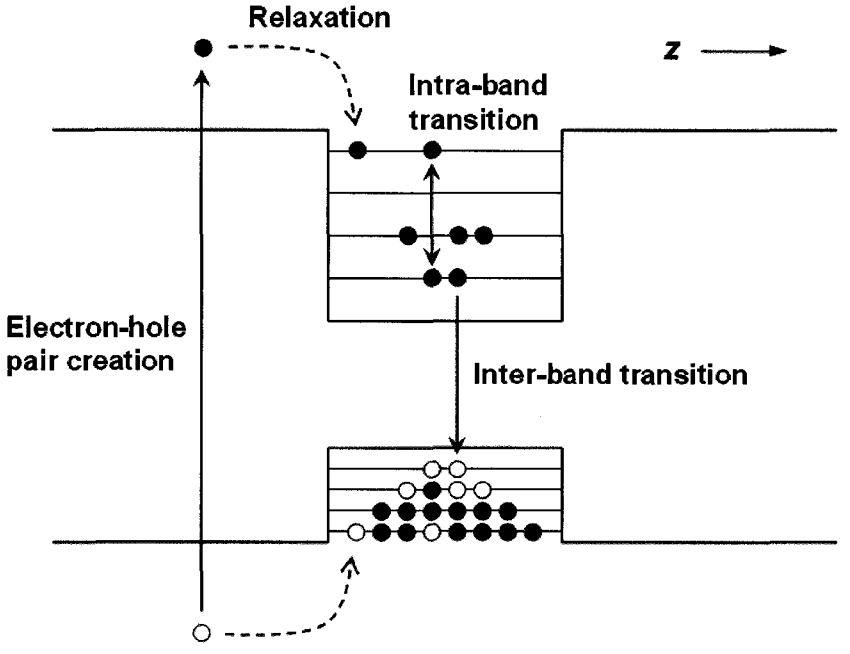

Figure II-7 Electronic transitions in a semiconductor with QD potential. The electron is excited non-resonantly to the conduction band, leaving a hole in the valence band. Through various mechanisms, the charge carriers can then relax into the QD potential. Once they occupy the QD energy levels, electron-hole pairs can recombine radiatively.

A first mechanism through which charge carriers can lose energy in the QD is by interaction with other particles. In these Auger processes [43], the energy is exchanged through inelastic carrier-carrier scattering. Usually, the particle in the QD will transfer its extra energy to a particle in the neighbouring barrier material. A second mechanism is the interaction with longitudinal optical (LO) and longitudinal acoustic (LA) phonons. Only the longitudinal phonons contribute to the energy relaxation of the charge carriers since the scattering with transverse phonons is elastic.[44] Although the LO phonons are the most efficient channel of relaxation in bulk material [45], energy relaxation through emission of a single phonon becomes rather inefficient in QDs. In fact, this first-order process is likely to be forbidden since it requires a precise fitting of the distance between two discrete energy levels and the phonon energy. If the smallest inter-level spacing is greater than the LO phonon energies, or if it falls in the phononic gap between LA and LO branches, the interaction of excitons with phonons is only possible through higher-order processes, such as the simultaneous emission of LO and LA phonons. Finally, the excitons can also relax to lower energy levels through the emission of a low-energy photon. However, the emitted photons carry angular momentum and a restriction is imposed on the possible transitions. As such, the total angular momentum must vary by ±1 between initial and final states.

The final process which is illustrated in Figure II-7 is the inter-band transition in which the conduction band electron returns to the valence band. Effectively, this transition corresponds to the recombination of the electron-hole pair. Since a single phonon has much less energy than the band gap, phonon-mediated inter-band transitions are forbidden in first order and only the higher order processes involving multiple phonons are possible. The probability of having an electron-hole recombination by means of phonon emission is therefore negligible compared to the direct interaction with photons, and inter-band transitions are more likely to be radiative processes. Considering that the interaction between charge carriers and the electromagnetic field is small, one may use perturbation theory to solve the Schrödinger equation. As a result, it is found that the probability of having a

radiative inter-band transition can be evaluated by Fermi's golden rule.[46] With the energy E_i of the initial state $|i\rangle$ being superior to the energy E_f of the final state $|f\rangle$, the transition rate is given by:

$$R_{i\to f}(\omega)=\frac{2\pi}{\hbar}\left|\langle f|V|i\rangle\right|^2\delta\left(E_f-\left(E_i+\hbar\omega\right)\right) \qquad \text{II-4}$$

where $\hbar\omega$ is the energy of the emitted photon and V is the perturbation potential. The δ-function expresses the fact that energy must be conserved, while the conditions for allowed inter-band transitions are obtained from the matrix element of V between the initial and final states. For the QD states $|n_x,n_y,n_z\rangle$, with the n indices representing the quantum number in each confined direction, one obtains the following selection rules: [47]

$$n_x^e=n_x^h \;;\; n_y^e=n_y^h \;;\; n_z^e=n_z^h \qquad \text{II-5}$$

Equation II-5 requires that the transitions occur between states with the same set of quantum numbers. This condition will be considered when building the excitonic spectrum of the QD.

Until now, the transition energies have only been treated in terms of single-particle energies. However, the presence of other charge carriers in the QD affects the transition energies. In non-resonant excitation experiments, there is a statistical fluctuation of the number of carriers within the QD and many-body effects must be taken into consideration. Many-body effects include the direct Coulomb interaction, the exchange interaction and the correlation effects. A qualitative understanding of these many-body effects can be given in terms of the Hartree-Fock method [48], which provides an approximation to the ground state energy of a quantum many-body system. By denoting the direct Coulomb interaction between carriers in levels

i and j by J_{ij}, and the exchange interactions as K_{ij}, the energy corresponding to the recombination of a single exciton is expressed as: [49]

$$E_{e_0h_0}^{1\to0} = \left(\varepsilon_{e_0} - \varepsilon_{h_0}\right) - J_{e_0h_0} \qquad \text{II-6}$$

where ε_{e_0} and ε_{h_0} are the energies of the single-particle levels. In the presence of N_s electrons and holes, the recombination energy becomes:

$$E_{e_0h_0}^{N\to N-1} = E_{e_0h_0}^{1\to0} + \left[\sum_{e_s}^{N_s}\left(J_{e_0e_s} - J_{e_sh_0}\right) + \sum_{h_s}^{N_s}\left(J_{h_0h_s} - J_{e_0h_s}\right)\right] - \left[\sum_{e_s}^{N_s} K_{e_0e_s} + \sum_{h_s}^{N_s} K_{h_0h_s}\right] \qquad \text{II-7}$$

where e_s and h_s represent the spectator electrons and holes such that $\sum_{e_s}^{N_s} = \sum_{h_s}^{N_s} = N-1$. The first term in brackets represents the direct Coulomb interaction between all carriers. This interaction has a significant impact on the energies of a system whose particles have the same charge, for example in transport experiments [50] where the QD is filled with electrons. However, in optically excited QDs, the effect is greatly reduced by the fact that most charge carriers are grouped in charge-neutral excitons. In fact, the term can vanish completely in equation II-7 since only excitons are considered and no extra charge particles are present in the system. This will be the case if the hole and electron wavefunctions are perfectly overlapped, as the repulsion will then be cancelled by an equal attraction. Nonetheless, it should be noted that optically excited QDs can contain extra charged particles. In fact, the results presented in the next chapter will reveal exciton recombination energies which are altered by the presence of an extra charged particle. The second term in brackets represents the exchange interaction which increases or decreases the energy of the system depending on the spin orientation of the carriers. In fact, the exchange interaction results in a repulsive energy between particles with unparallel spins and an attractive energy between particles with parallel spins.[51] In a simple two electron system, the exchange

energy can be expressed by adding a spin-spin interaction term $-JS_1 \cdot S_2$ to the Hamiltonian of the system, where S_1 and S_2 represent the spin operators of the two electrons. However, it should be noted that the exchange energy is not the result of a spin-spin interaction, but rather the manifestation of the Coulomb interaction between indistinguishable fermions. The exchange interaction can therefore produce a splitting of transition energies. Finally, transition energies are also shifted by correlation effects. In order to calculate the precise transition energy between two states, one must consider the mixing with other configuration states. The correlation effects result in a significant lowering of the transition energies as the final state is mixed with configurations of higher energy. For example, this will reduce the transition energy of the biexciton state with respect to the transition energy of the exciton state. In fact, the final state of the single exciton recombination is an empty dot with no possible mixing of other configurations. Conversely, an exciton recombination in the initial biexciton state will leave an exciton in the QD. The final state is therefore an admixture of different configurations which include the exciton in excited states. It should be noted that a detailed description of all many-body effects requires complex calculations which are beyond the scope of this thesis. Nonetheless, the brief overview presented in the above discussion should make it clear that single-particle energies are altered by the presence other charge carriers within the QD.

2.2.2 Electronic Structure in Magnetic Field

The QDs studied in this project were self-assembled by Stranski-Krastanow growth mode and their height was controlled with an indium flush process. The resulting QDs have the shape of flat disks with a thickness considerably smaller than the lateral dimension. In fact, the vertical confinement is strong enough that only the first quantum well sub-band is relevant. All the QD particles therefore occupy the lowest quantized state along the growth direction, and the vertical confinement can be represented by a constant shift in energy with respect to the

energy gap of the dot material. The vertical and lateral confinements are therefore decoupled and the electronic structure of the charge carriers can be described by their confinement in the lateral dimension.

In the cylindrically shaped dot, the motion of the electrons and holes in the x-y plane is subject to a parabolic lateral potential:

$$V(x,y)=\frac{m^*\omega_0^2}{2}\left(x^2+y^2\right) \qquad \text{II-8}$$

where (x,y) is the position of the particle, m^* is its the effective mass and ω_0 is the harmonic frequency describing the strength of the lateral confinement; the separation between energy levels being accordingly equal to $\hbar\omega_0$. Omitting the Zeeman term relating to the particle spin, the unperturbed Hamiltonian of the single particle is given by:

$$H_0=\frac{\vec{P}^2}{2m^*}+V(x,y) \qquad \text{II-9}$$

where $\vec{P}$ is the particle momentum.

When an external magnetic field is applied in the z vertical direction, the particle motion in the x-y plane is perturbed. This change in velocity can be accounted for by including the magnetic vector potential $\vec{A}$ such that $\vec{P}\rightarrow\vec{P}-q\vec{A}$.[52] With its curl being equal to the magnetic field ($\vec{B}=B\hat{z}=\vec{\nabla}\times\vec{A}$), the vector potential can take the form $\vec{A}=\frac{1}{2}By\hat{x}-\frac{1}{2}Bx\hat{y}$, and the Hamiltonian can thus be expressed as:

$$H=\frac{1}{2m^*}\left(P_x-\frac{qBY}{2}\right)^2+\frac{1}{2m^*}\left(P_y+\frac{qBX}{2}\right)^2+\frac{m^*\omega_0^2}{2}\left(X^2+Y^2\right) \qquad \text{II-10a}$$

$$H = \frac{1}{2m^*}\left(P_x^2 + P_y^2\right) + \frac{m^*\Omega^2}{2}\left(X^2 + Y^2\right) + \frac{\omega_c}{2}\left(XP_y - YP_x\right) \qquad \text{II-10b}$$

where $\omega_c = qB/m^*$ is the cyclotron frequency and a new oscillator frequency is defined as:

$$\Omega^2 = \omega_0^2 + \left(\frac{\omega_c}{2}\right)^2 \qquad \text{II-11}$$

The eigenstates and eigenenergies of such a Hamiltonian were determined analytically by Fock [53] and Darwin [54]. The first two terms in equation II-10b have the form of a two-dimensional harmonic oscillator equation, which suggests that the Hamiltonian can be re-written in terms of creation and annihilation operators. In fact, one can make use of the two pairs of circularly polarized creation-annihilation operators: [46]

$$a_+ = \frac{1}{2}\left[\beta(X - iY) + \frac{i}{\beta\hbar}\left(P_x - iP_y\right)\right] \;;\; a_+^\dagger = \frac{1}{2}\left[\beta(X + iY) - \frac{i}{\beta\hbar}\left(P_x + iP_y\right)\right] \qquad \text{II-12a}$$

$$a_- = \frac{1}{2}\left[\beta(X + iY) + \frac{i}{\beta\hbar}\left(P_x + iP_y\right)\right] \;;\; a_-^\dagger = \frac{1}{2}\left[\beta(X - iY) - \frac{i}{\beta\hbar}\left(P_x - iP_y\right)\right] \qquad \text{II-12b}$$

where $\beta = \sqrt{m^*\Omega/\hbar}$ has been introduced for clarity. Using the commutation relation for the position and momentum operators ($[X, P_x] = [Y, P_y] = i\hbar I$), the Hamiltonian can be written in the form:

$$H = \hbar\Omega_+\left(a_+^\dagger a_+ + \tfrac{1}{2}\right) + \hbar\Omega_-\left(a_-^\dagger a_- + \tfrac{1}{2}\right) \qquad \text{II-13a}$$

$$\Omega_{\pm} = \Omega \pm \omega_c = \left[\omega_0^2 + \left(\frac{\omega_c}{2}\right)^2\right]^{\frac{1}{2}} \pm \left|\frac{\omega_c}{2}\right| \qquad \text{II-13b}$$

The Hamiltonian is now expressed as a pair of independent harmonic oscillators having the familiar form [48] from which one can directly obtain the eigenenergies. As such, the single particle energy spectrum corresponding to the FD states $|n_+, n_-\rangle$ is:

$$E(n_+, n_-) = (n_+ + \tfrac{1}{2})\hbar\Omega_+ + (n_- + \tfrac{1}{2})\hbar\Omega_- \qquad \text{II-14a}$$

$$n_+ = 0,1,2,\ldots \;\; ; \;\; n_- = 0,1,2,\ldots \qquad \text{II-14b}$$

In the absence of magnetic field, $\Omega_+ = \Omega_- = \omega_0$ and the states are degenerate. This degeneracy is represented in the FD state diagram of Figure II-8 a). Each group of degenerate states is associated to a shell. Owing to the analogy between atomic and QD states, these shells are identified using the atomic shell notation s, p, d, etc. The FD shell notation is illustrated in Figure II-9. The number subscript given to a degenerate state refers to its orbital angular momentum. When an external magnetic field is applied in the growth direction, the levels split and the degeneracy is lifted. The evolution of energy levels in magnetic field is depicted in Figure II-8 b). New degenerate shells are formed when energy levels cross at periodic fields, giving the characteristic criss-cross pattern of the FD spectrum.

The single particle energies can now be extended into an excitonic model with energies corresponding to the difference between electron and hole levels. By setting the zero energy at the top of the valence band, the electron energies are given by:

$$E^e(n_+^e, n_-^e) = E_0 + (n_+^e + \tfrac{1}{2})\hbar\Omega_+^e + (n_-^e + \tfrac{1}{2})\hbar\Omega_-^e \qquad \text{II-15}$$

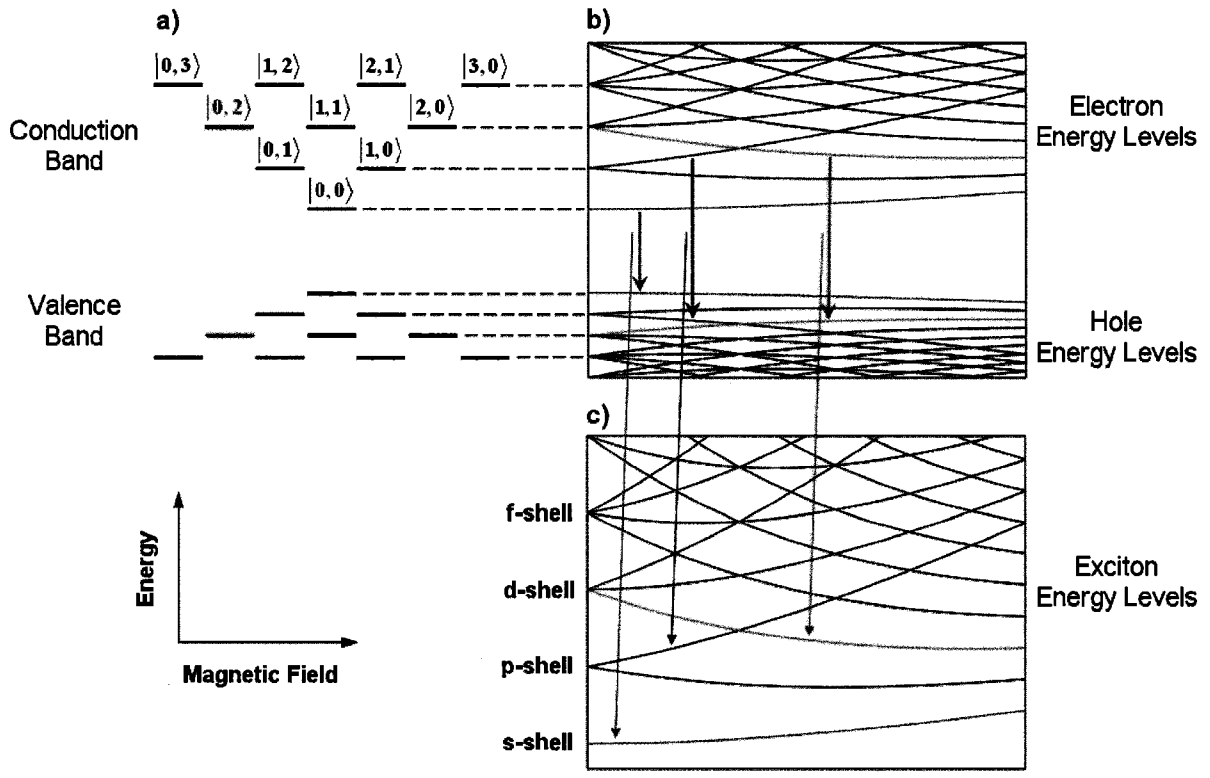

Figure II-8 FD model describing a) the energy states at zero Tesla and b) the evolution of electron and hole energy levels in magnetic field. The radiative recombination of electron-hole pairs results in c) the excitonic spectrum which is observed in optical spectroscopy.

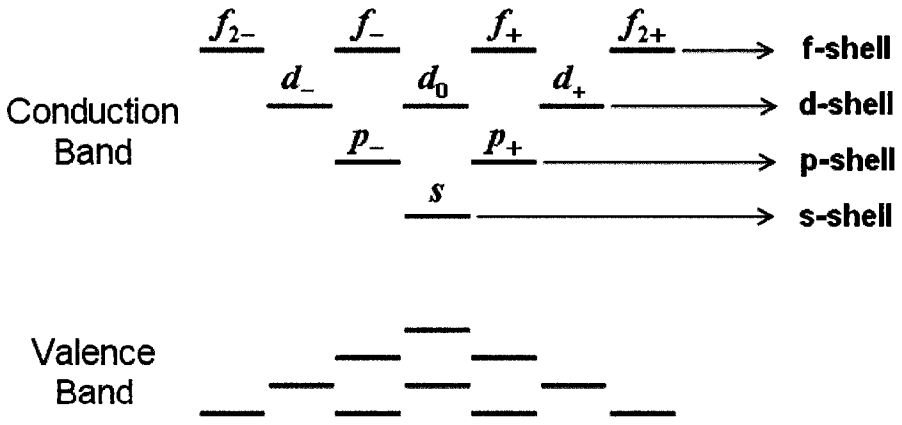

Figure II-9 FD shell notation. From the similarity between atomic and QD energy levels, the shells are labelled with the atomic shell notation s, p, d, etc. Degenerate states are given a number subscript referring to its orbital angular momentum.

where E_0 is the offset energy which includes the energy gap of the dot material and the shift created by the vertical confinement. The holes have opposite energies for the same set of quantum numbers:

$$E^h(n_+^h, n_-^h) = -\left[(n_+^h + \tfrac{1}{2})\hbar\Omega_+^h + (n_-^h + \tfrac{1}{2})\hbar\Omega_-^h\right] \qquad \text{II-16}$$

The excitonic spectrum observed in optical spectroscopy corresponds to the energy difference between electron and holes states $E^X = E^e - E^h$. From the previous discussion of transition rates governed by Fermi's golden rule, it was revealed that radiative inter-band transitions occur between QD states with the same set of quantum numbers. In the dipole approximation, the allowed transitions between Fock-Darwin states are therefore restricted by the selection rules $n_+^e = n_+^h$ and $n_-^e = n_-^h$. As illustrated in Figure II-8 c), the energy spectrum of the photons emitted by exciton recombination is therefore:

$$E^X(n_+^X, n_-^X) = E_0 + (n_+^X + \tfrac{1}{2})\hbar\Omega_+^X + (n_-^X + \tfrac{1}{2})\hbar\Omega_-^X \qquad \text{II-17a}$$

$$\hbar\Omega_\pm^X = \hbar\Omega_\pm^e + \hbar\Omega_\pm^h \qquad \text{II-17b}$$

The evolution of FD states in magnetic field can be described conceptually by considering the interplay between two physical phenomena. The first is the orbital shift caused by the different orbital angular momentum states. Since the particles have a charge, their orbital motion creates an effective magnetic field which interacts with the external field. This interaction will, for example, produce the splitting of the two opposite angular momentum states in the p-shell. The second effect is the diamagnetic shift which is caused by the fact that, in the external magnetic field, the charged particle will rotate at the cyclotron frequency. This motion creates another effective field which also interacts with the external magnetic field. Since the cyclotron motion is a result of the external field, the

diamagnetic shift is a second order effect which appears only at higher fields. As a consequence, all states tend to shift toward higher energies at high magnetic fields.

The theory presented thus far is sufficient to describe previous experiments which were performed on dot ensembles. However, this project aims to reveal more subtle effects by studying SQDs. In particular, the spin can be omitted from the FD model in order to describe dot ensemble measurements in magnetic field. In that case, the spin splitting cannot be resolved due to the inhomogeneous broadening from the distribution of dot size and composition. In the following chapter, SQD measurements will be introduced. In chapter IV, the evolution of different spin states in magnetic field will then be presented. In fact, a modified FD will need to be derived in order to describe the spin states. Moreover, the model will need to consider SO coupling. As mentioned in the description of the FD model, the excited states have different orbital angular momentum. The coupling between spin and orbit will consequently depend on the particular state. By studying the excited states in magnetic field, it will therefore be possible to reveal the effect of SO coupling.

Chapter III: Quantum Dot Spectroscopy

The experimental results presented in this thesis were all obtained using various techniques of optical spectroscopy. By spectrally dispersing the light emitted from a source, one can measure the intensity of the light as a function of energy. The previous chapter explained how carriers in QDs can emit photons through radiative recombination. The energy of the photons inherently depends on the structural and material properties of the QD. The spectroscopic study of the dot luminescence therefore provides an effective and non-destructive technique to characterize samples. When the electrons are excited to the conduction band using a light source, the spectroscopic experiment is referred to as PL.

In this chapter, PL experiments are presented for dot ensembles and SQDs. In the former case, the excitation light is focused on a sample area containing many dots. The luminescence from all the dots is collected and spectrally measured. In the latter case, a region of the sample containing only one dot is optically isolated such that the collected luminescence originates from a SQD. Section 3.1 will introduce the dot ensemble PL which is used to assess sample quality before the samples are processed in preparation for SQD spectroscopy. In particular, section 3.1.2 shows how samples must be annealed in order to shift the QD emission energy into the sensitivity range of the detector. Section 3.2 then presents 0 T SQD PL results in preparation for high magnetic field experiments.

3.1 Dot Ensemble Photoluminescence

A typical sample of SAQDs will have a dot density of roughly 10^{10} cm^{-2}, or ~100 per square micron. In the standard PL setup that was used to measure the dot ensembles, the excitation light source is a laser beam focused on the sample with a circular spot of diameter ~50 μm. The number of dots probed during a typical PL experiment is therefore on the order of 10^5. With such a large population of QDs, the fine structure of individual dots is not observable in the spectrum. A dot ensemble measurement provides information on the overall dot population of the sample.

3.1.1 Experimental Technique

The dot ensemble measurements were performed using a standard PL setup which is schematically described in Figure III-1. The excitation light source is a solid state laser emitting at 532 nm. The laser wavelength corresponds to a photon energy well above the barrier band gap and accordingly also above the confinement energy of the QD states. In this type of non-resonant excitation, the photons are absorbed in the barrier material and the carriers must relax into the QD states. As the carriers lose energy through different thermalization processes such as phonon emission and inelastic collisions, they move arbitrarily in the sample until they are captured in a QD. The carriers must then relax from the continuum of states in the barrier bulk material to the discrete states of the QD.

The laser beam passes through a rotating disc that intermittently blocks the light. The frequency at which this chopper rotates is fed to the lock-in amplifier and used as a reference signal. The purpose of the lock-in technique is to reduce the noise from parasite light reaching the detector. The technique is based on the orthogonality of sinusoidal functions.[55] The lock-in receives the signal from the detector and multiplies it by the reference signal before integrating it over a certain

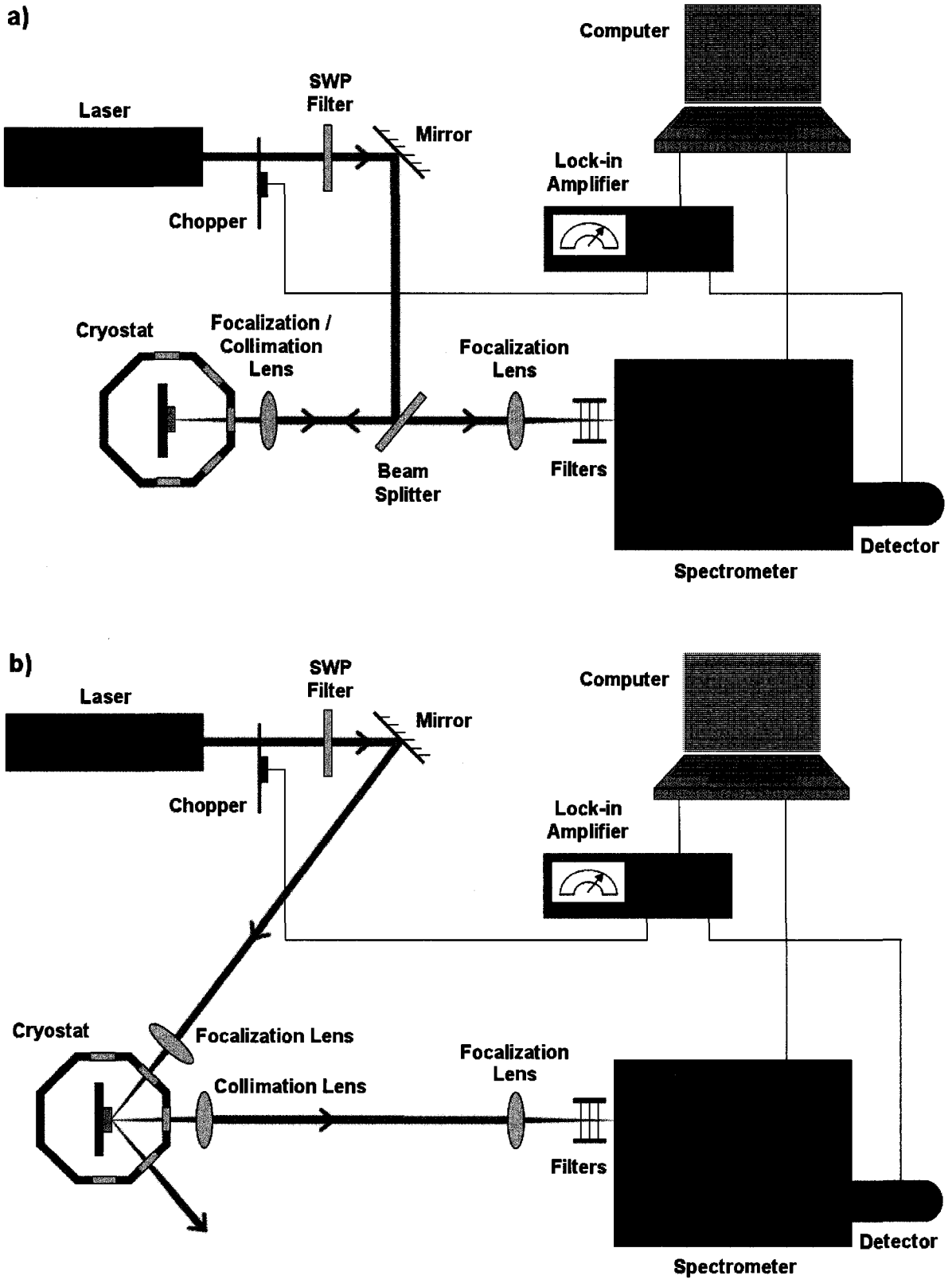

Figure III-1 Standard PL setup. a) The perpendicular configuration is used for non-resonant excitation while b) the incident light hits the sample at 45° in resonant excitation.

time period. When two sinusoidal functions multiplied together are integrated over a time much longer than the period of the two functions, the result is zero if the functions have different frequencies. Therefore, any part of the detector signal which does not have the same frequency as the reference signal from the chopper will be attenuated. The laser beam then passes through a short-wave-pass (SWP) filter with a cut-off wavelength between 532 nm and 1064 nm (typically 700 nm). The gain medium in the solid state laser is Nd:YVO_4, a crystalline material formed by adding neodymium ions to yttrium orthovanadate. The medium is pumped with diodes and the light emitted from the neodymium at 1064 nm resonates inside the laser cavity. However, a frequency doubling crystal placed within the cavity converts this light by combining photons to form new photons that have twice the energy and half the wavelength. This second harmonic generation produces a laser light with a wavelength of 532 nm. Nonetheless, a SWP filter removes any of the remaining first harmonic light from the laser beam. This is especially important when measurements are taken at or near the 1064 nm wavelength. The beam is redirected toward the sample with a 50/50 beam splitter. Before entering the cryostat, it passes through a convergent lens which focalizes the beam onto the sample surface. In this perpendicular configuration, the luminescence from the sample is collimated by the same lens and half of the collected light will pass through the beam splitter before being focalized onto the entrance slit of the 0.5 m CVI Digikröm 240 monochromator. The luminescence is dispersed by two gratings and only a small range of wavelengths can exit through the other slit of the monochromator. PL measurements were typically taken with 600 grooves mm^{-1} gratings, slit widths of 1 mm and a chopper frequency of 450 Hz. The light that passes through the exit slit enters a liquid nitrogen cooled germanium detector which then sends a signal to the lock-in amplifier. The signal, which is proportional to the light intensity, is amplified and filtered from some of the noise before a digital equivalent is sent to the computer. The computer then sends a signal to the monochromator in order to move the gratings and to measure another narrow wavelength range. This process is repeated until the desired spectral range has been covered. If necessary, optical density filters are placed at the monochromator

entrance in order to prevent saturation of the detector. In this perpendicular configuration, some of the scattered laser light will be collimated and it will follow the same path as the luminescence. Although the laser wavelength is relatively far from the spectral range of the QD luminescence, the second order of the grating will disperse the laser light within the luminescence range and a long-wave-pass (LWP) filter must therefore be used to prevent the laser light from entering the monochromator. In order to limit the thermal effects and improve the luminescence efficiency, the sample is cooled inside a cryostat. The sample is placed on a copper plate which is directly in contact with liquid nitrogen. Because of the good thermal conductivity of copper and since the vacuum inside the cryostat thermally isolates the sample from the outside environment, the sample can be cooled to nearly the temperature of liquid nitrogen, i.e. 77 K.

When such a non-resonant excitation is used, the laser light can be filtered before the monochromator and a perpendicular configuration such as the one shown in Figure III-1 a) can be used. However, if the sample is excited resonantly or near resonantly, a LWP filter will block some of the QD luminescence. For that reason, the cryostat is equipped with 5 windows and it is possible to configure the setup as in Figure III-1 b) where the incident light hits the sample at a 45° angle. Most of the incident light is then scattered at an angle and very little laser light will be captured by the collimation lens. The luminescence can thus be measured without the need for a LWP filter. Such a configuration requires precise alignment of the focalization and collimation lenses to ensure they both have their focus at the same point on the sample surface. Since the perpendicular configuration uses the same lens for both focalization and collimation, the optical alignment is more straightforward. For that reason, confocal geometry is favoured when using non-resonant excitation.

3.1.2 Rapid Thermal Annealing

Annealing is a heat treatment that alters the structure of a material. This technique can be applied to SAQD samples in order to change their electronic properties.[56-59] In view of the project goal which is to study SQDs in magnetic field, the samples were annealed for two reasons. First, the annealing shifts the luminescence energy into the sensitivity range of the silicon charge-coupled device (CCD) camera used in the SQD PL and magneto-photoluminescence (M-PL) experiments. On the other hand, the annealing reduces the energy spacing between the QD states. In the magnetic field evolution of states, this will cause crossings to occur at lower fields. With the same range of magnetic fields, more information can consequently be obtained from state crossings.

The annealing was performed in a rapid thermal annealing (RTA) system which uses an array of high-power quartz lamps as the heat source. The RTA chamber is flushed with a high purity nitrogen gas in order to remove any oxygen from the atmosphere and prevent oxidation of the sample. The sample is also capped with pieces of GaAs substrate in order to limit surface degradation. The proximity cap effectively reduces the diffusion of As into the atmosphere.[57] The sample is rapidly heated to a high temperature, providing enough thermal energy to the atoms for them to diffuse. It is believed that the main effect of the intermixing process is an increase in the lateral size of the QDs.[60] This flattening of the dot structure alters the confinement potential in two ways. The narrowing of the vertical dimension blueshifts the energy of the confined states whereas a wider lateral potential leads to a smaller energy spacing between the QD shells. Moreover, the significant blueshift can be attributed to a change in the QD material composition. As Ga atoms are introduced into the QD during intermixing, the band gap of the new InGaAs material is increased with respect to the initial InAs band gap. Another effect of the intermixing is a narrowing of the dot ensemble PL peaks. The Fick's diffusion equation, in the form of the error function solution, explains how thicker dot regions diffuse faster than thinner regions.[59] Dots that are structurally different will

therefore tend to be more similar after annealing. In effect, the inhomogeneous broadening is reduced and there is less variation in the emission energies of the dot ensemble. The effects of intermixing can be observed in Figure III-2 by comparing the PL of the as-grown sample V0250-9 with the PL of the same sample after annealing for 35 sec at 850 °C. The s-shell peak shifts by 99 meV toward higher energies, the energy spacing between the s and p shells is reduced from 58 meV to 34 meV and the FWHM of the p-shell decreases from ~38 meV to ~28 meV.

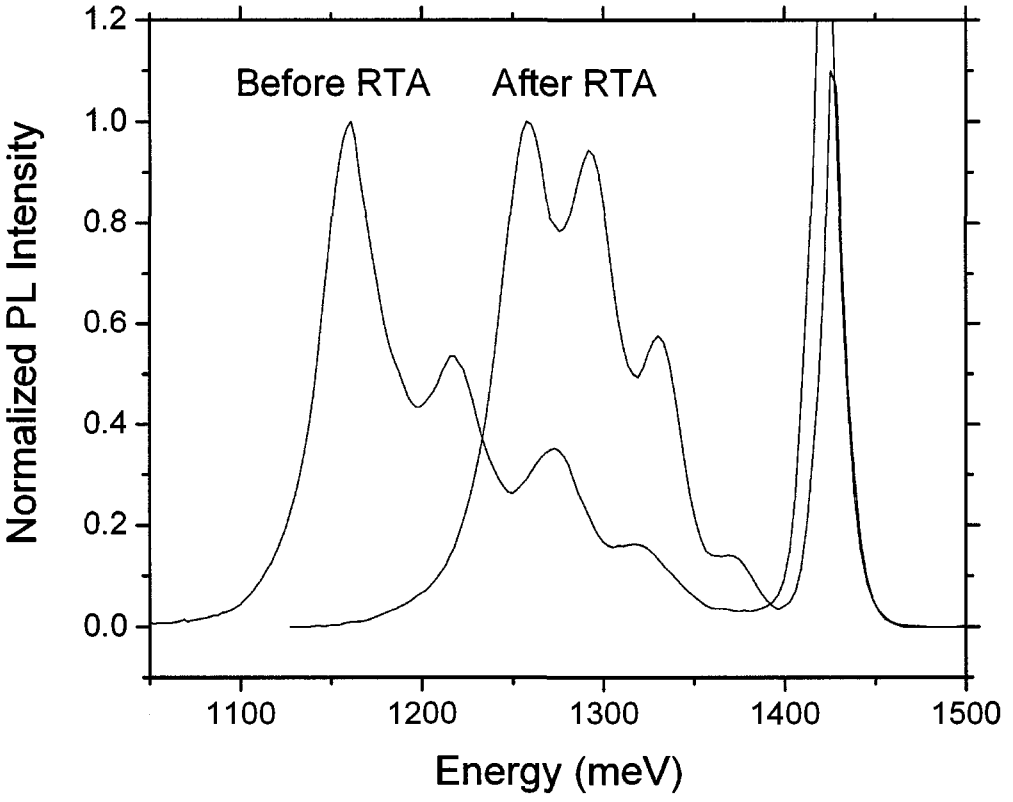

Figure III-2 PL spectra before and after RTA on sample V0250-9. The sample was annealed for 35 sec at 850 °C.

3.1.3 Results and Discussion

The results of the PL measurements on sample V0250-9 are presented in Figure III-3 for different excitation powers. The experiments were conducted with

the sample cooled to 78 K and the excitation source was the 532 nm light of a Nd:YVO_4 solid state laser. In Chapter II, the QD states were showed to be discrete because of the 3-dimensional confinement potential. The luminescence from QDs should therefore be expected to have discrete energies which would lead to sharp detection peaks in the PL spectra. However, the spectra in Figure III-3 reveal relatively large emission peaks. This is a result of the fluctuations in the dot population. The dots are not uniform; there are variations in size and composition which consequently lead to different electronic properties. The distribution of dots produces the inhomogeneous broadening that can be observed in dot ensemble measurements.

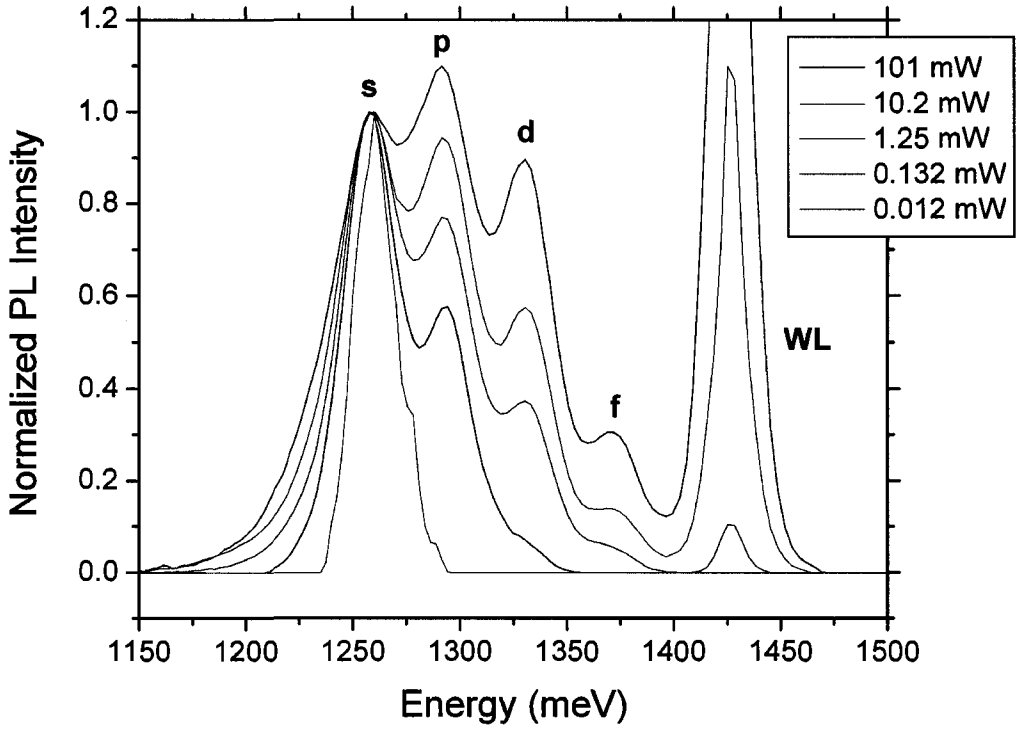

Figure III-3 Dot ensemble PL spectra for different excitation powers. The spectra reveal emission from the various QD shells. As the excitation power is increased, state filling leads to emission from excited states.

As the excitation power is increased, a higher concentration of excitons is created in the sample and more carriers will relax in the QD confinement potential

per unit time. A PL experiment is a dynamic equilibrium process in which there is a balance between the rate of exciton creation and the rate of exciton recombination (either radiative or non radiative). When the sample is excited with the lowest power, the spectrum is comprised of a single peak. In this case, the excitons get trapped in the QD confinement potential and are able to relax to the lowest energy state before recombining and emitting a photon. The single peak in the luminescence thus corresponds to the recombination of excitons in the ground state, or s-shell. As the excitation power is increased, the rate of exciton creation becomes greater than the rate at which excitons can recombine in the ground state. The lifetime of a particle in a particular state is described by Fermi's golden rule.[61] It is strongly affected by its interaction with other particles, which is expressed in the perturbating potential that scatters the particle. Since Pauli exclusion prevents carriers from occupying the same quantum state simultaneously, the ground state is limited to two excitons of opposite spin. When a third exciton is trapped in the QD potential, it cannot relax to the ground state if the other two excitons already occupy that state. The third exciton must stay in an excited state during which time it has a certain probability to recombine radiatively. Such a recombination in the first excited state will emit luminescence at a higher energy, which is depicted by the appearance of a second peak in the PL spectrum. Following the same principle, emission from higher excited states occurs when the lowest states are filled with carriers. If all of the QD states are filled, the exciton cannot relax in the QD potential and it will continue to diffuse in the sample. A high concentration of excitons therefore enhances the probability of radiative recombination in either the WL continuum or in the GaAs barrier material. In Figure III-3, the WL emission increases rapidly once the excitation power is above 1 mW. Based on the shell filling phenomenon [62-64], one can roughly estimate how many excitons are in the dot on average as a result of the dynamic equilibrium process. For example, when the incident light has a power of 0.132 mW, the spectrum reveals emission from the s and p shells, and a small shoulder from d-shell emission. The luminescence can be understood if the dots have about 6 excitons on average; 2 occupying the s-shell and the other 4 occupying the p-shell. Since this process is dynamic, the dot will

sometimes have more than 6 excitons and there is therefore a small probability of recombination in the d-shell.

When more than one exciton is present in the dot, the recombination energies are different from the energies of the single particle states in the confinement potential because of the many-body interactions. This leads to a second type of broadening which is observed in the PL spectra. As the excitation power is increased, there is luminescence from progressively lower energies. In fact, the lower energy limit shifts from 1235 meV at 0.012 mW to 1150 meV at 101 mW. This band gap renormalization [65] is a consequence of exchange and correlation effects. However, the effect of many-body interactions is more evident in SQD measurements since inhomogeneous broadening does not occur in that case.

3.2 Single Dot Photoluminescence

The previous section revealed how standard PL measurements of SAQD samples will probe many dots at once. This provides information on the overall dot population in the sample, but the fine structure of individual dots cannot be observed because of the inhomogeneous broadening. If a dot is optically isolated such that the collected luminescence is emitted by this single dot, it is then possible to eliminate this broadening and obtain the energy spectrum of a SQD.

3.2.1 Experimental Technique

The first step taken in order to isolate a single dot was to obtain a relatively long inter-dot distance by growing wafers of low dot density. However, the distance is still smaller than the laser spot diameter. In order to measure only one QD at a time, one must exploit post-growth processing methods that either remove or block the surrounding dots. After thermal annealing, a series of samples was thus processed using one of two patterning techniques: mesa structures and nano masks. In the first method, the sample is etched everywhere except on small areas that were protected using a resist. The etch depth is chosen to be below the InAs dot layer, meaning that only the protected areas, or mesas, potentially contain QDs. With nano masks, all of the QDs remain in the sample but they are shielded from the incident light by a 200 nm thick gold (Ti/Au) film. The mask covers the entire sample except for small window openings that allow optical access to the QD layer. In both cases, a pattern of different sized mesas or holes is created along the sample using electron-beam lithography. Although the mask obstructs some of the dot luminescence, it has the advantage of also blocking the incident light around the window. With the mesa structures, photoexcitation of carriers around the mesas produced a detrimental background emission from radiative recombination in the GaAs. The nano masks were accordingly used for the magnetic field measurements and the SQD results presented in the next section are from hole patterned samples.

The nano mask pattern that was evaporated on sample V0250-9 is illustrated in Figure III-4 along with a schematic view of a hole that demonstrates how the mask allows optical access to a single dot. The pattern is repeated on the sample surface until the sample is fully covered.

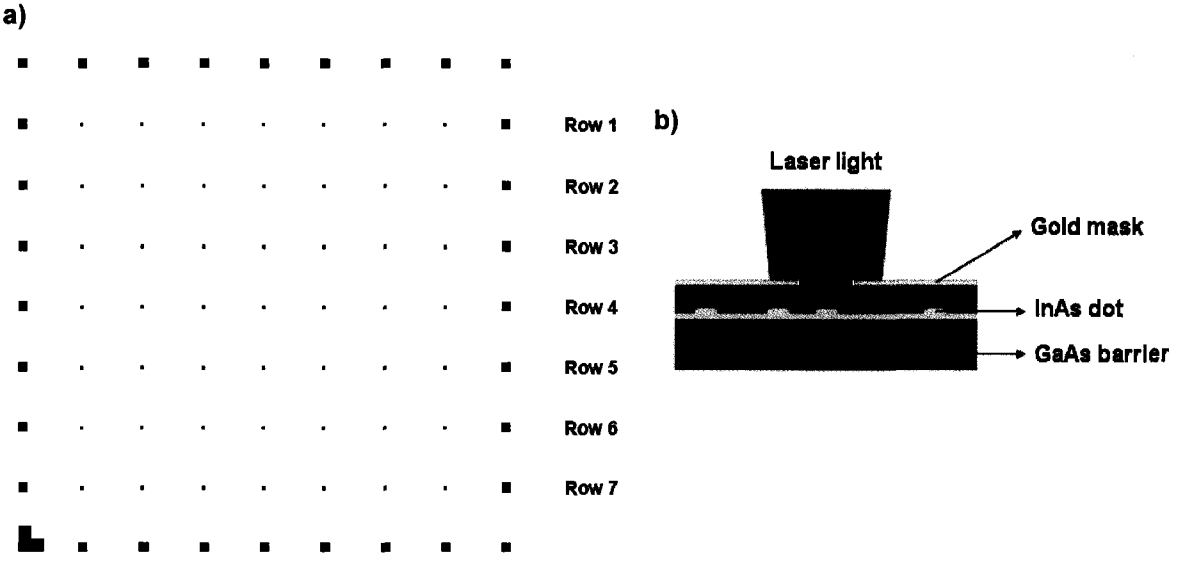

Figure III-4 a) Nano mask pattern and b) the optical isolation of a SQD in a hole. Rows 1 and 3 have 1x1 μm holes, rows 5 and 7 have 2x2 μm holes, and rows 2, 4 and 6 have 0.5x0.5 μm holes.

From the AFM images of the dot surface layer (Figure II-3), it can be estimated that samples from the V0250 wafer have a dot density of ~2-3 per square micron. Therefore, the hole sizes were chosen to be between 0.5x0.5 μm and 2x2 μm. The larger 20x20 μm holes on the edge of the pattern contain many dots and are used for navigation on the sample. In order to measure a SQD, the holes must be investigated one at a time. By analysing the luminescence spectra from a particular hole, it is possible to determine whether the hole contains many dots, a few dots, a single dot or no dot at all. In the next section, PL results are presented for each case. By mapping the mask pattern, one can establish the location of the holes that contain a SQD. These locations were identified using a matrix-like notation in order to locate the same hole in subsequent experiments.

The micro-photoluminescence (Micro-PL) setup used to measure the luminescence of patterned samples is described in Figure III-5. The laser source is now an argon gas laser in single line operation. Since the excited argon ions have many competing decay paths, the emitted photons will have various wavelengths ranging between 300 and 600 nm. By having a prism in front of one of the end mirrors, a specific wavelength can be selected to reflect back into the cavity and stimulate identical emissions. As a result, the prism forces a single line operation and the laser emits at a specific wavelength, which in this case was selected to be the strongest transition intensity line at 514.5 nm. However, the argon ions can still emit photons which will exit the laser cavity at different wavelengths and a band-pass (BP) filter is therefore used to select only the 514.5 nm photons and block the other emission lines. The laser beam is focused onto the sample using a two-mirror design known as a Cassegrain lens. Since the mask pattern has a 400 μm pitch between windows, the laser spot diameter of ~5 μm ensures that only one window is excited at a time. The high numerical aperture of the Cassegrain lens means that a relatively high proportion of the luminescence is collected. The lens also has the advantage of having zero chromatic aberration so that any wavelength between 200 and 2000 nm can be focused or viewed through the lens. This makes it possible to focus white light and collect an image of the sample with a camera. In fact, the setup is constructed such that the collected light can be directed either to the monochromator or a camera. The 0.5 m CVI Digikröm 480 monochromator has a single grating which remains static through measurements since the CCD detector is position-sensitive. Micro-PL measurements were typically taken with a 600 grooves mm^{-1} grating and slit widths of 100 μm. A range of wavelengths is dispersed onto the detector surface and the intensity of each wavelength is measured in parallel. The camera image allows one to locate the large mesa or hole structures on the pattern edge. The large structures are used as a reference and one can then navigate inside the pattern accordingly. The cryostat is placed on top of stages that can be translated horizontally by nano motors. Inside the cryostat, the sample is placed on a copper mount which is cooled to ~10 K from the continuous flow of liquid helium. The vacuum limits heat transfer with the outside environment

while a silicone based thermal compound ensures proper conductivity between the mount and the sample.

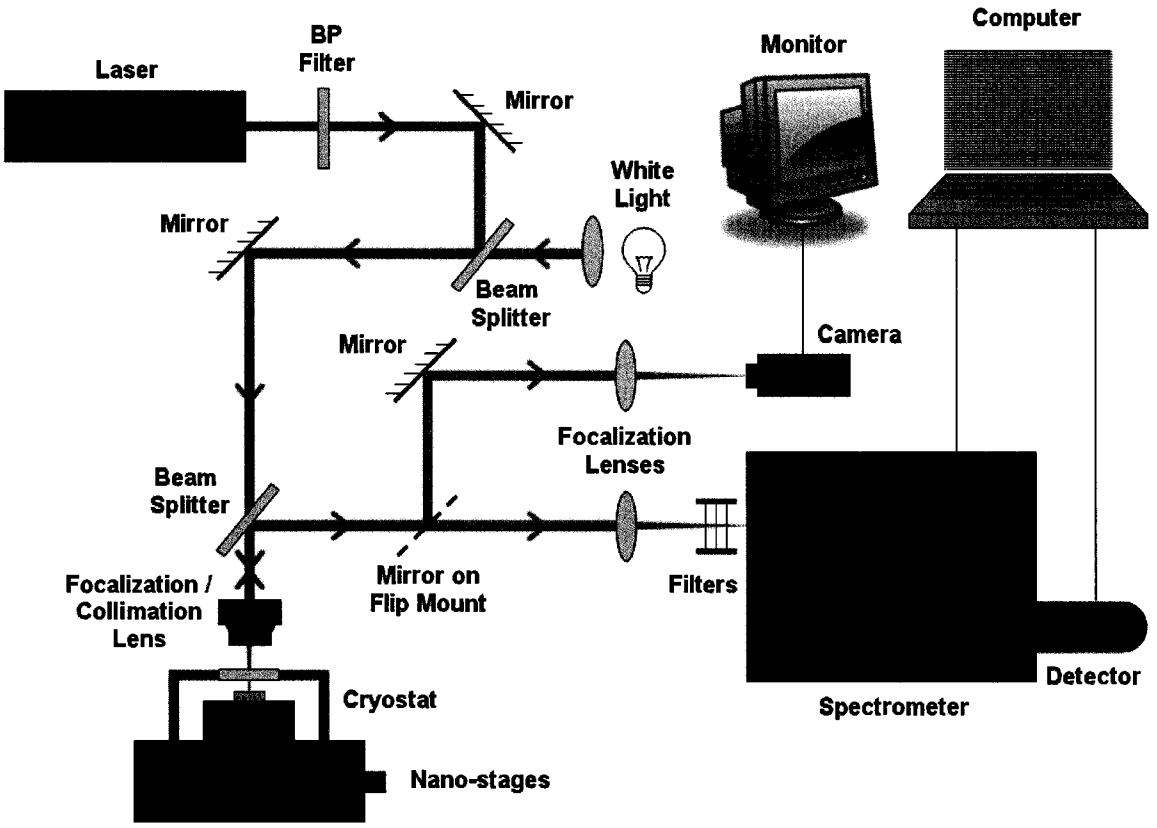

Figure III-5 Micro-PL setup. The laser beam is focalized to a ~5 μm diameter spot size on the sample surface using a Cassegrain lens.

3.2.2 Results and Discussion

The AFM measurements on the surface dot layer, which was grown under the same conditions as the active dot layer, reveal a dot density of ~2-3 dots per square micron. The probability of finding a single dot in a certain area follows a Poisson distribution. It can accordingly be estimated that there is a 33% chance of finding a SQD in a 0.5x0.5 μm hole, a 21% chance for a 1x1 μm hole and a 0.05% chance for a 2x2 μm hole. However, the smallest holes obstruct more light and less

dot luminescence is collected. In such an experiment it is important to maximise the collection since the luminescence emitted by a SQD is relatively weak. For that reason, the 1x1 μm holes were systematically investigated along the sample surface in order to locate SQDs.

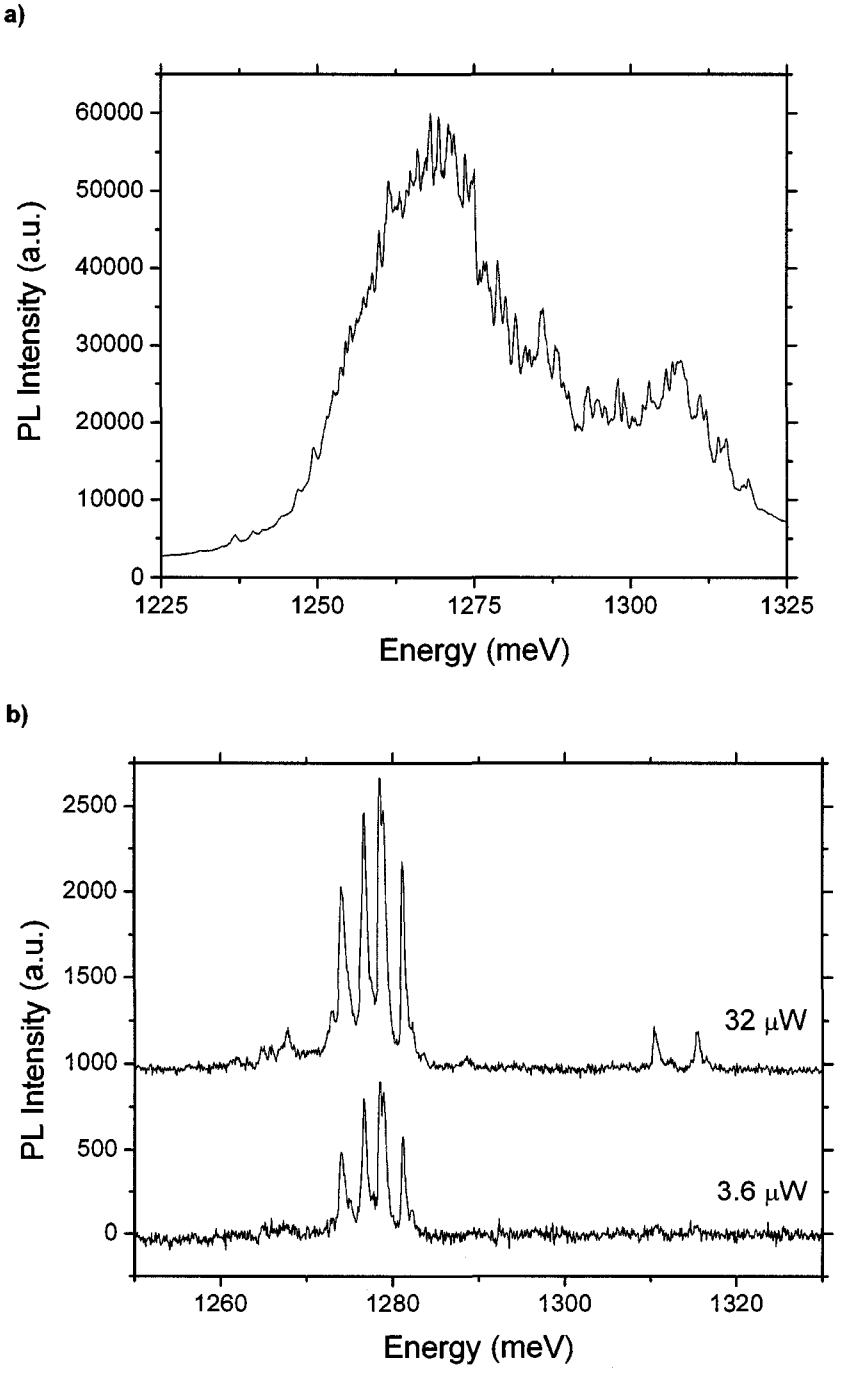

Figure III-6 PL spectra of a) many dots in a 20x20 μm hole and b) a few dots in a 1x1 μm hole.

To determine whether a hole contains a single dot or not, one must be able to distinguish between a spectrum from many dots, a few dots or a single dot. Examples of the first two cases are presented in Figure III-6. The 20x20 μm hole contains a few hundred dots, which is why the PL spectrum resembles a dot ensemble measurement. There is a main peak centered around 1270 meV from the s-shell emission and a secondary peak near 1307 meV from the p-shell emission. Unlike the ensemble measurements, it is possible to observe features from individual dots. In Figure III-6 b), the spectrum from a 1x1 μm hole contains a few dots. At low excitation power, there are four narrow lines in the s-shell energy range, which suggests that the hole contains four dots. When the excitation power is increased, some lines emerge in the p-shell energy range. The four line pattern in the s-shell is unique to that particular hole. For different holes, the number of dominant lines as well as the spacing between them varies. This random variation implies that these lines must originate from different dots which vary slightly in size and composition. Therefore, the measured hole must in fact contain a few dots. Accordingly, one can expect the low excitation power spectrum from a SQD to have one dominant line in the s-shell energy range. Figure III-7 illustrates such an example. Figure III-7 a) presents the excitation power dependence whereas the low power emission is shown in Figure III-7 b). Increasing the power leads to shell filling along with emission from the p-shell and subsequently the d-shell. Furthermore, there is a broadening effect as new emission lines appear at lower energies with respect to each shell. This is most apparent for the s-shell emission, which becomes almost flat at high excitation powers.

Further inspection of the low power PL reveals that the spectrum has more features than one single narrow line. There is a dominant line at 1286.4 meV and a weaker emission line a 1283.9 meV. Moreover, the main line does not have a symmetric shape. The shoulders on each side suggest that there is a very closely spaced line at lower energy and a very weak emission line at higher energy. However, the lines cannot be resolved since this spectrometer has a resolution of ~1 meV. This is confirmed by measurements taken with a higher resolution

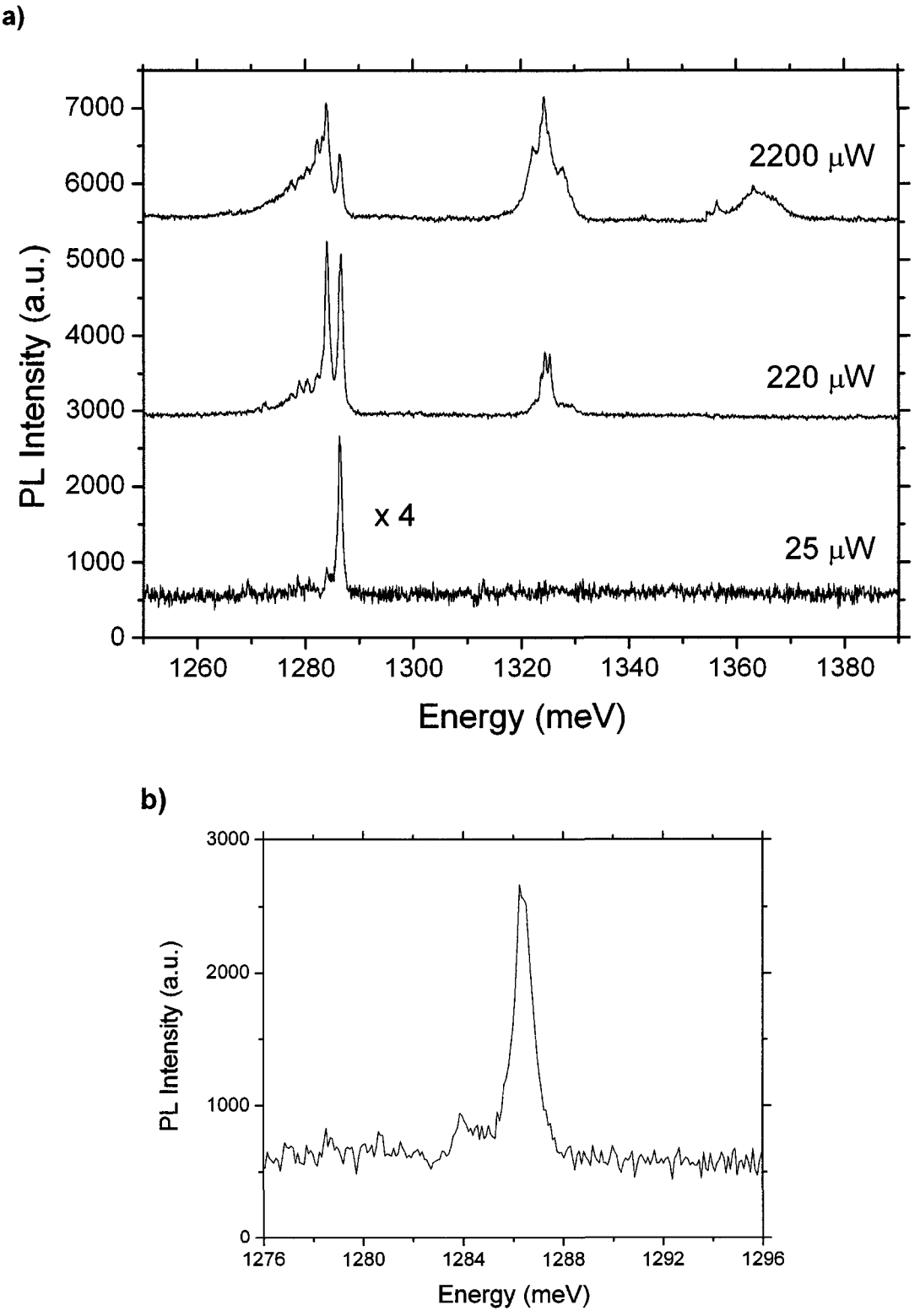

Figure III-7 PL spectra of a SQD in a 1x1 μm hole. Shell filling can be observed in a) the excitation power dependence while b) the low excitation power spectrum has a dominant line in the s-shell.

spectrometer (the M-PL setup described in section 4.1.1). The lines are well resolved in the low power spectrum presented in Figure III-8. There are two closely spaced lines at 1286 meV and 1286.4 meV, and a weak emission line at 1287.8 meV. The lower energy line which could be resolved using the Micro-PL system now has more intensity and it appears at 1283.6 meV. In addition, a very weak emission line can be observed at 1278.4 meV. All of the lines have a very small linewidth as a result the discrete nature of the QD states. The linewidth is resolution limited, with all peaks having a FWHM of ~0.25 meV.

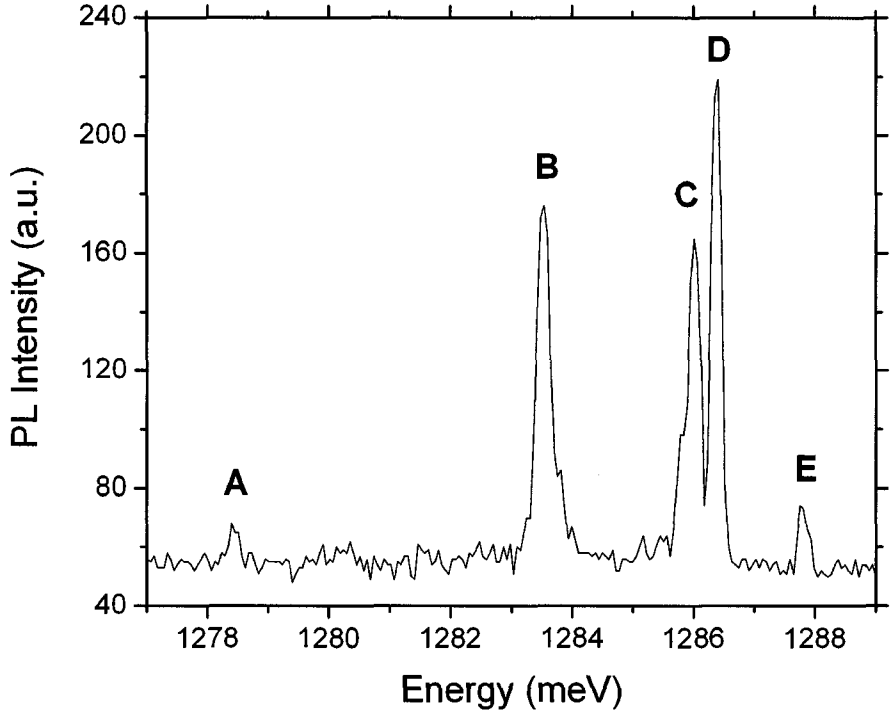

Figure III-8 High resolution SQD PL spectrum at low excitation power. The spectrum contains a few narrow emission peaks.

The presence of a few peaks in the lowest excitation power spectrum could be interpreted as emission from a few dots. However, the particular pattern of lines in the low power spectrum has been observed in many spectra from different holes. The observation of a few lines in low power PL measurements has also been reported in other experiments.[66-72] In the field-effect structures of references 68

and 69, the charge could be tuned and the exciton complexes could therefore be studied in charge neutral or negatively-charged environments. In all of the experiments, the lines are attributed to different exciton complexes and charge states. The four main lines denoted B to E in Figure III-8 form a characteristic pattern which was observed in the spectrum of many different holes. Moreover, reference 72 presents PL results from a few SQDs isolated in mesa structures on a similar sample. Although the relative intensity and position of the peaks vary slightly, the lines are always contained in an energy range of about 4 meV and the spectra exhibit very close similarities. This is strong evidence that each pattern of lines originates from a SQD, and the lines arise from different exciton complexes and charge states. As discussed in chapter II, the QD transition energies are subject to many-body effects and the energy of an emitted photon depends on the particular configuration. The fluctuations in excess charge are due to the statistical nature of carrier capture into a dot.[73] Furthermore, the lines can be assigned to specific states by comparing the pattern to the results of N.I. Cade *et al.* in references 71 and 73, which include a thorough power dependence study and polarization dependent measurements. The lines labelled C and D would then originate from the emission of a single exciton state, with a fine structure splitting of ~0.4 meV due to dot anisotropy. If the dot symmetry is broken, e.g. by dot elongation and strain, the M = ±1 bright exciton states are mixed with one another and the radiative doublet is split by the anisotropic electron-hole exchange energy.[74,75] The lines A and E are associated with charged exciton states, with A having an extra electron with the exciton and E having an extra hole. These three particle states are also referred to as negative and positive trions, respectively. Finally, the B line would originate from the biexciton state, which is not observed in the low power spectrum of reference 71 but appears when the excitation power is increased. It should also be noted that the biexciton peak has a shoulder at higher energy, suggesting the presence of two different peaks which are not resolved. This supports the idea of dot anisotropy, as the biexciton peak would be expected to also have a fine structure splitting. However, it is not clear why the biexciton splitting is smaller than that of the single exciton. The power dependent measurements presented in Figure III-9 corroborate

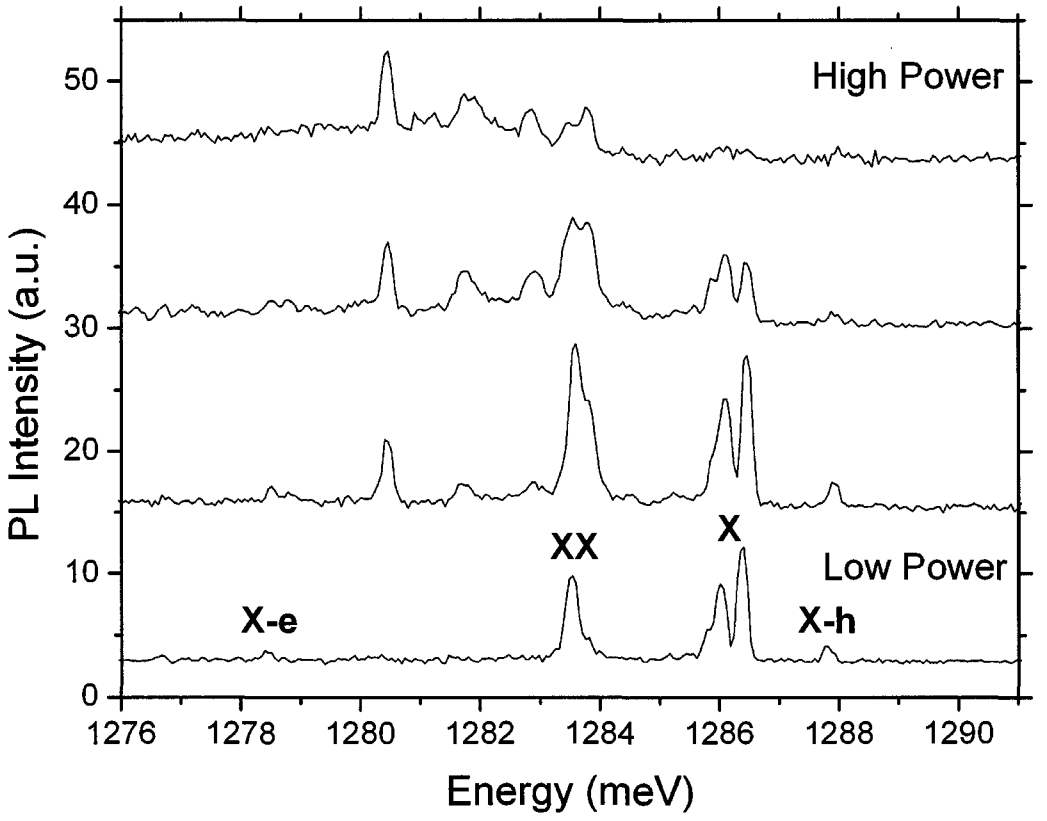

Figure III-9 Power dependence of high resolution PL from a SQD. The single exciton (X) and charged exciton (X-e and X-h) peaks tend to saturate and then decrease in intensity as the excitation power is increased. At high excitation power, the biexciton (XX) peak becomes more intense then all original lines.

with this assignment of the B line. At higher excitation powers, the emission from this peak becomes greater than all of the other original peaks since there is then a higher probability of having two excitons in the dot. All of the other original lines tend to saturate and then decrease in intensity as the excitation power is increased, which supports the attribution to neutral and charged single exciton states. In Figure III-7 b), the biexciton peak at 1283.9 meV is relatively weak, which suggests it might disappear completely at very low excitation power. Due to the limited amount of time available on the high resolution setup and long accumulation times, spectra at even lower excitation power could not be accumulated. Furthermore, the

assignment of charged exciton states is supported by the results of reference 72. The excess of positive charges from the n^+ doped GaAs substrate in the investigated samples leads to more intensity from the positive trion peak while the negative trion peak is not observed. The samples studied in this thesis have a semi-insulating substrate, which explains why both trions are observed with comparable intensities. Additionally, the energy difference between X-h and X is expected to be smaller than between X-e and X.[76] The direct Coulomb interaction leads to a higher recombination energy with the positive charge and a lower energy with the negative charge, but both configurations are redshifted by correlation effects. Thus, the X-h peak is brought closer to X while the X-e peak is further distanced.

A methodical power dependence study of the QD luminescence and polarization-dependent measurements would be required in order to identify the peaks with more certainty. Unfortunately, this was not possible due to the limited time period with the high resolution setup and the long accumulation times needed to measure the weak luminescence. Nonetheless, the observation of the characteristic pattern in many spectra and the similarities with results from other PL experiments on InAs QDs is strong evidence that the peaks are due to different exciton complexes and charge states. Although the peaks cannot be unambiguously identified, the characteristic pattern can be associated to emission from a SQD.

Now that SQDs have successfully been isolated, PL measurements will be taken in magnetic field. The results presented in the following chapter originate from different SQDs. Although the low excitation power spectra with the characteristic peak pattern will not be presented, it should be noted that these measurements were taken in order to verify the presence of only a SQD.

Chapter IV: Quantum Dot Properties in Magnetic Field

The energy shell structure of charge carriers in SAQDs is approximately that of a particle confined in a two-dimensional parabolic potential. Chapter II described how the harmonic oscillator energy shell gives rise to the FD spectrum in a magnetic field. In fact, the shell degeneracy can be lifted by applying a magnetic field perpendicular to the lateral potential plane, and M-PL spectroscopy therefore provides a probe to analyze the energy spectrum of QDs. The M-PL measurements were taken at different excitation powers in order to study the luminescence with different carrier populations.

The experimental technique for M-PL spectroscopy will be described in section 4.1. Subsequently, results will be presented for low and high excitation powers. When the incident light has a low intensity, the splitting of spin states can be observed in the ground state emission. On the other hand, measurements taken with high excitation intensity reveal that the evolution of excited states in magnetic field follows the FD spectrum. However, SO interaction must be added to the FD model to explain the fine structure in the results and a new modified model will accordingly be derived in section 4.2. The theoretical results of the model will then be compared to the experimental results of the M-PL measurements.

4.1 Magneto-Photoluminescence

Applying a magnetic field effectively modifies the electronic properties of a QD. By studying the interaction of the different angular momentum states with the field, one can gain a better fundamental understanding of semiconductor QD systems. As explained in Chapter II, the electronic energy spectrum of QDs is often that of two-dimensional harmonic oscillators, and the emission pattern observed in magnetic field is referred to as the FD spectrum. In this section, the experimental technique for the M-PL measurements is first described before results are presented for different excitation powers. By isolating a SQD, the inhomogeneous broadening is eliminated and the results reveal the fine features of the energy spectrum. However, an intense PL emission from excited states implies the presence of multiple excitons in the QD potential and state filling. When such a multi-exciton system is confined in a small volume, many-body interactions become a significant perturbation to single particle energies. As a result, the energy spectrum will vary depending on the carrier population in the dot.

4.1.1 Experimental Technique

The M-PL measurements were performed with a resistive magnet at the Grenoble High Magnetic Field Laboratory. The optical setup is schematically described in Figure IV-1. As in the SQD PL setup, the 514.5 nm line from an argon ion laser is focused onto the patterned sample and the luminescence is collected before being dispersed in a monochromator and detected by a CCD camera. The sample must now be placed within the narrow bore of a magnet, which makes it impossible to use standard geometric optics for the focalization and collimation of light. Consequently, optical fibres are used to guide the light to and from the sample. The laser beam is coupled to a single-mode fibre which propagates the light to the sample. The excitation light is then focused onto the sample by two aspheric micro-lenses. The laser spot has a diameter of ~10 μm which assures that

the excitation laser illuminates only a single window. A 600 μm core multi-mode fibre is placed directly above the sample surface to collect the dot luminescence. Evidently, the setup is designed such that the focal point of the micro-lenses is under the collection fibre.

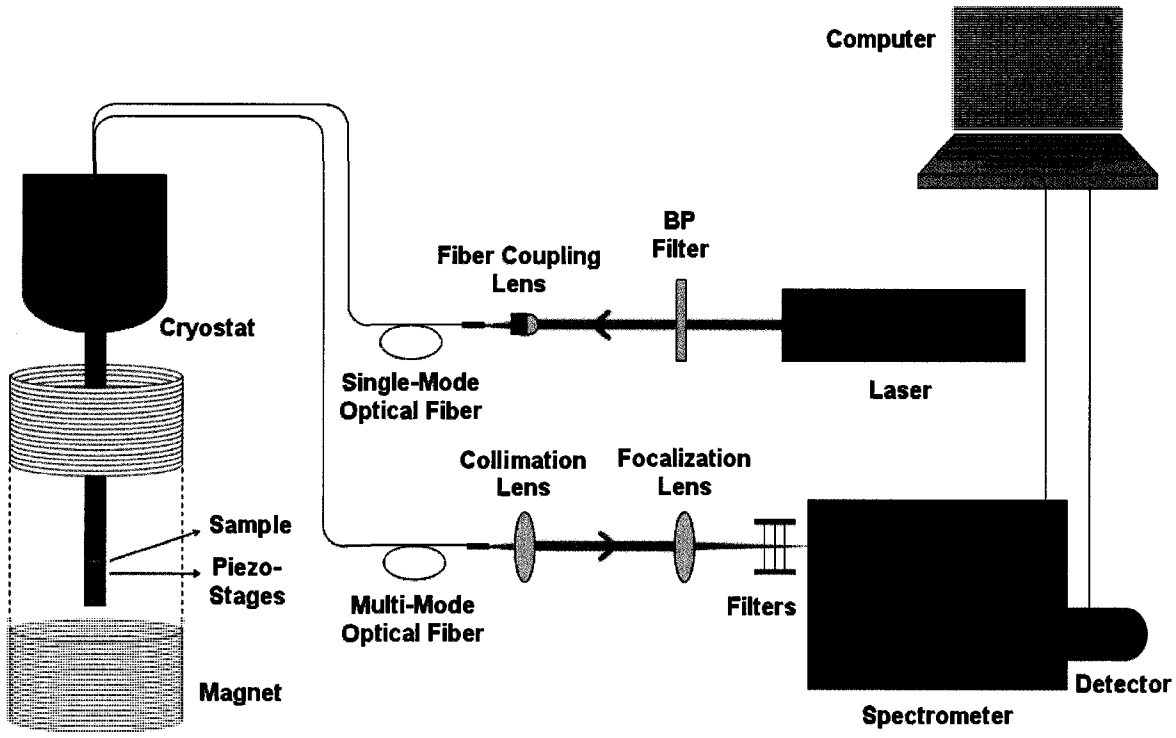

Figure IV-1 M-PL setup. The sample is placed in the narrow bore of a magnet which makes it impossible to use standard geometric optics for the focalization and collimation of light. Optical fibres are therefore used to guide the light to and from the sample.

A picture of the optical fibre setup is shown in Figure IV-2, as well as a picture of the piezo-stages that enable precise positioning of a specific window below the fibre optics. The stages are driven by piezoelectric motors which can deliver accurate movement even in the measurement environment of low temperature and high magnetic field. The motors make use of the piezoelectric effect [55] whereby a material changes its shape when an electric field is applied. The motion of the stages is powered by slip-stick motion, a patented driving technology of Attocube Systems. A guiding rod is quickly accelerated by applying

an appropriate voltage to the piezoelectric actuator such that the inertia of the sliding block overcomes the friction. The guiding rod then moves back to its initial position slowly enough so that the sliding block this time sticks to it and thus makes a net step. By assembling two horizontal steppers and one vertical stepper on top of each other, the positioning unit has three degrees of freedom and the sample can be positioned appropriately under the fibre optics. The x-axis and y-axis stages provide the horizontal movement to place a specific window below the fibre optics while the z-axis stage allows one to focus the excitation light on the sample surface.

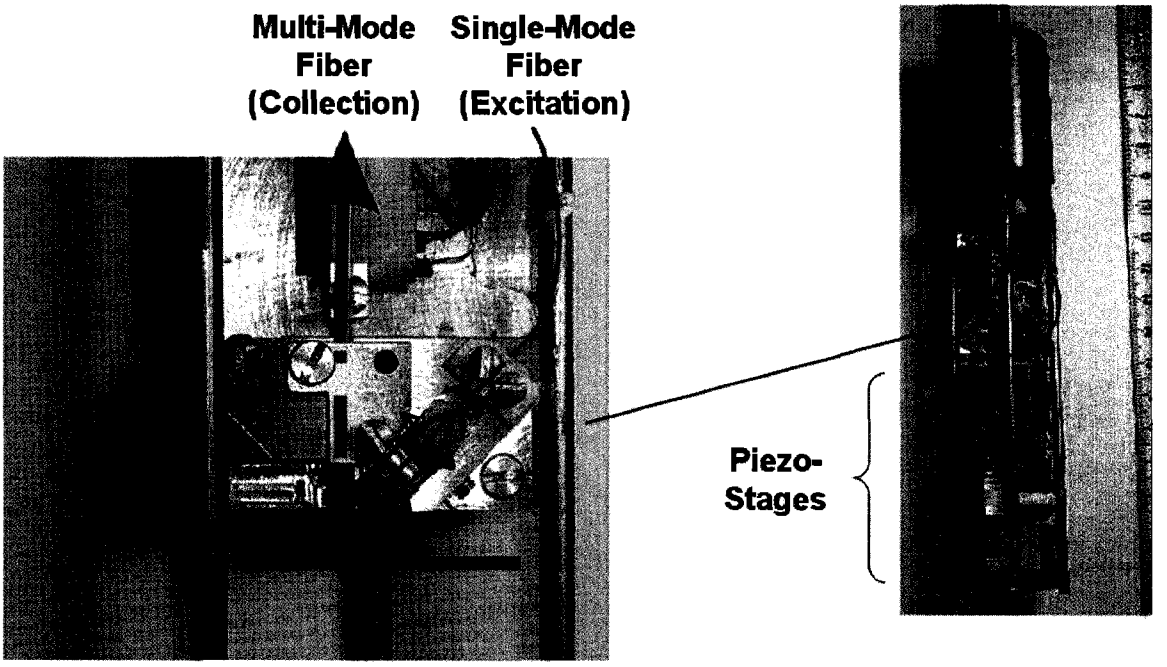

Figure IV-2 Images of piezo-stages and optical fibre setup. The piezo-stages enable precise positioning of a specific window below the fibre optics. (Photo by A. Babinski)

The setup is placed in a non-magnetic steel tube that is mounted in a helium cryostat. The sample can therefore be immersed in liquid helium (4.2 K) during PL measurements. The cryostat is then tightly lowered in the 50 mm diameter bore of the magnet. In this configuration, the magnetic field is applied perpendicular to the plane of the dots (Faraday configuration). The resistive magnet has a power source that can deliver up to 20 MW, which produces a continuous magnetic field up to 28

T. In order to prevent overheating and melting of the copper-based coil, the magnet is cooled by the circulation of deionised and deoxygenized water (see Appendix A). The luminescence which was guided through the collection fibre is collimated before being focalized into the slits of a 1 m double grating monochromator and detected by a liquid nitrogen cooled CCD camera. This spectrometer has a high resolution of ~0.25 meV. Once again, the CCD detector is position-sensitive and the gratings remain static during measurements.

4.1.2 Ground State Emission

The QD system is first measured with a low excitation power. Under these conditions, the rate at which excitons are trapped in the dot is small and the carriers are able to relax to the lowest energy level before recombining radiatively. Hence, the luminescence is comprised of emission from the ground state, or s-shell. Moreover, the low carrier population in the dot limits the number of possible exciton configurations and the transition energies can be resolved in the PL spectra. In fact, the main peaks observed in the spectra presented in Figure IV-3 can be associated to specific exciton complexes and charge states.

Although the PL measurements were taken on a different SQD, the 0 T spectrum shown in Figure IV-3 a) has a peak pattern similar to the one presented in section 3.2.2. Following the same interpretation, the doublet of lines at 1281.7 meV and 1282.3 meV originates from the fine structure splitting of the single exciton state while the brightest peak at 1279.7 meV is associated with the biexciton state, suggesting that the excitation intensity is slightly greater than for the PL measurements of Figure III-8. The charged exciton states have weak emission intensity at 0 T. Nonetheless, these trion states can be associated to the peaks observed at 1276 meV and 1284.2 meV. The extra peaks which are not observed in Figure III-8 can be attributed to configurations containing additional particles due to the greater excitation intensity. Figure IV-3 b) describes the magnetic field evolution

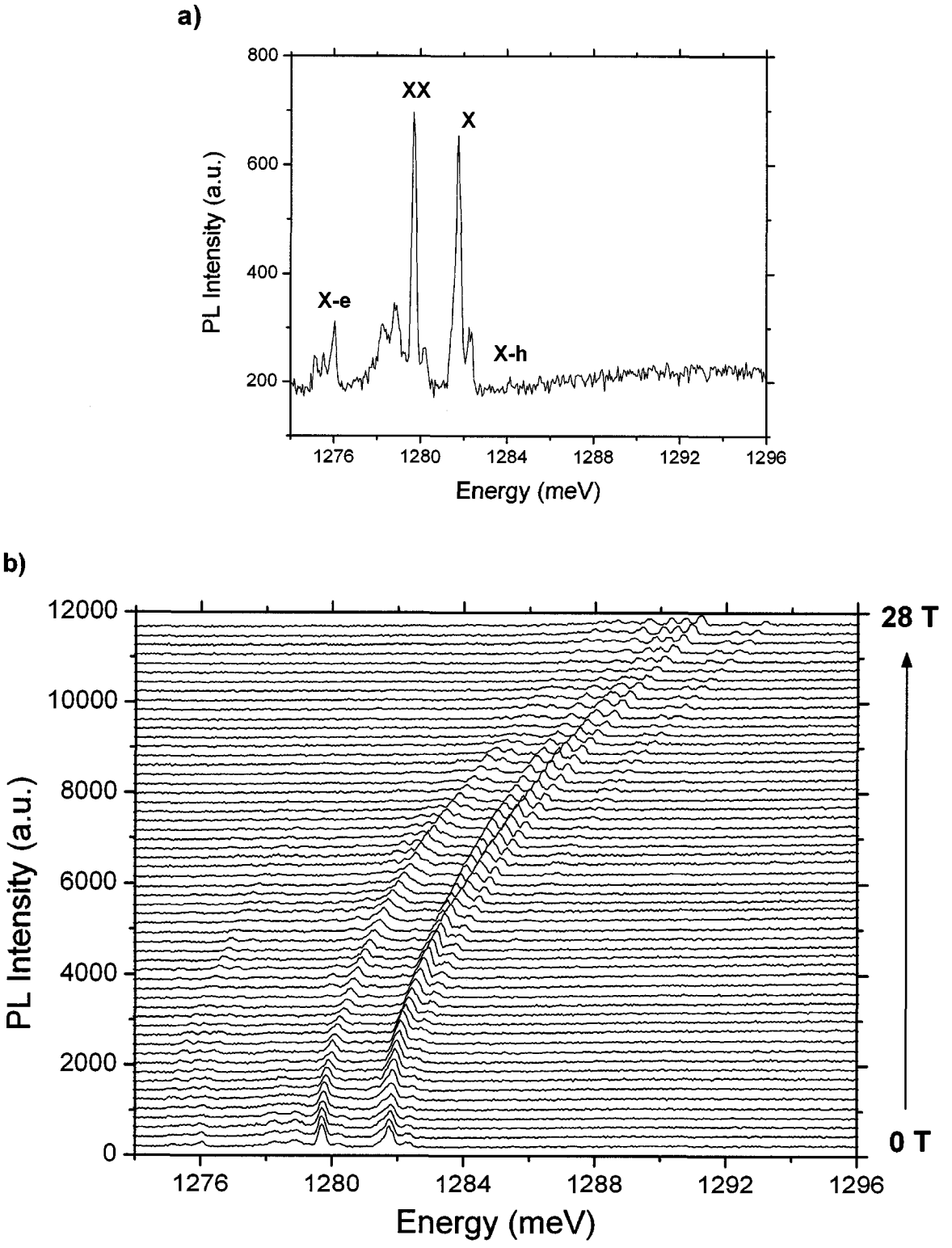

Figure IV-3 Magnetic field evolution of the ground state emission from a SQD. A close-up of the 0 T spectrum is shown in a) while the spectra in b) were measured in magnetic fields up to 28 T. The spectra are presented in a waterfall by offsetting each spectrum for clarity.

of the SQD ground state emission. The PL measurements were taken at 0.5 T increments for magnetic fields ranging from 0 T up to 28 T, and the results are shown in a waterfall by offsetting each spectrum for clarity. A first consequence of the magnetic field is a variation in peak intensities. The biexciton peak intensity decreases with increasing magnetic field, which indicates that the excitation intensity is reduced. This can be caused by a displacement of the piezo-stages in the magnetic field and/or vibrations from the water pumps propagating to the fibre optics setup.

In the external magnetic field, the spectral lines of degenerate states are split into several components. The interaction between the orbital magnetic moment and the magnetic field lifts the shell degeneracy and shifts the orbital states according to the FD spectrum. In addition, the magnetic moment associated with the spin of carriers will also interact with the external field. In fact, the magnetic field exerts a torque on the total magnetic moment $\vec{\mu}$ with a resulting potential energy: [48]

$$U = -\vec{\mu} \cdot \vec{B} \qquad \text{IV-1a}$$

$$\vec{\mu} = -\frac{e\hbar}{2m_e} g\vec{J} = -\mu_B g\vec{J} \qquad \text{IV-1b}$$

where μ_B is the Bohr magneton, $\vec{J}$ is the total angular momentum and g is the g-factor (the Landé g-factor in the case of an electron), which relates the classical magnetic moment of a charged particle to the appropriate angular momentum quantum number. In general, $\vec{J}$ is the sum of the contributions from the orbital angular momentum $\vec{L}$ and the spin angular momentum $\vec{\sigma}$, which are not separately conserved. In fact, the spin couples with the orbit and only the total angular momentum is conserved.[46] The wavefunction of a particle in the periodic potential of a semiconductor consists of the product between a plane wave envelope function and a periodic Bloch function which has the same periodicity as the crystal

potential.[39] In the QD ground state, electrons in the s-type conduction band have zero orbital angular momentum from both the envelope and Bloch function. On the other hand, holes carry orbital momentum even in the ground state since they have a nonzero contribution from the Bloch function of the p-type valence band.[77] Coupling between the conduction and valence bands results in the ground state electrons also carrying nonzero orbital angular momentum.[78] As a result, SO coupling occurs in the QD ground state. However, the details of the coupling will only be considered in the next section, where different orbital states are observed in the PL spectra and the coupling effect is essential for a complete description of the results. Conversely, the spectra in Figure IV-3 contain only emission peaks from the s-shell, and the carriers therefore have the same orbital angular momentum. As a result, the SO interaction can be accounted for by renormalizing the g-factor into an effective value g^*. The total magnetic moment of the exciton can thus be expressed in terms of the total exciton spin $\vec{\sigma}$:

$$\vec{\mu} = -\mu_B g^* \vec{\sigma} \qquad \text{IV-2}$$

The growth of SAQDs implies a lattice mismatch between dot and barrier material, which consequently creates a strained dot material. This strain leads to a significant splitting of the valence band into light and heavy holes having spin $J_h = \frac{1}{2}$ and $J_h = \frac{3}{2}$, respectively.[42] At low temperature, the hole occupies the heavy hole state [79] with a z-axis projection $J_{h,z} = \pm\frac{3}{2}$, whereas the electron spin $S_e = \frac{1}{2}$ has a projection along the z-axis $S_{e,z} = \pm\frac{1}{2}$. The spin angular momentum projections of the heavy hole exciton states are $M = S_{e,z} + J_{h,z}$.[74] The $|M| = 1$ states are optically active (bright excitons) while the $|M| = 2$ states are optically inactive (dark excitons). The electron and hole must therefore have opposite spin for coupling to occur between the exciton state and the light field. For a magnetic field in the z direction, the magnetic potential energy can thus be expressed as:

$$U = \mu_B g^* \vec{\sigma} \cdot \vec{B} = \mu_B g^* MB = \pm \tfrac{1}{2}(g_e^* + 3g_h^*)\mu_B B \qquad \text{IV-3}$$

where g_e^* is the effective g-factor of the electron in the conduction band and g_h^* is the effective g-factor of the heavy hole in the valence band. For uniformity, an effective spin formalism with $S = \frac{1}{2}$ can be used to treat the heavy hole state, and the g-factor can accordingly be rewritten as $3g_h^* \rightarrow g_h^*$. The energy splitting between the two exciton spin states is therefore given by:

$$\Delta E = \left| g_e^* + g_h^* \right| \mu_B B \qquad \text{IV-4}$$

For a given magnetic field, the absolute value of the effective excitonic g-factor $g_{exc}^* = g_e^* + g_h^*$ can be deducted be measuring the energy difference between spin states. The position of each spin state is tracked in Figure IV-4 a) for the single exciton state. It should be noted that the orientation (spin up or down) of each spin state has not been identified. For a free electron in an external magnetic field, the spin up state will increase in energy while the spin down state will decrease in energy with respect to the mean energy value of both states. However, this is not necessarily the case in a semiconductor material where the g-factor value is altered by the SO interaction. In fact, the effective g-factor can take a negative value, in which case the spin states will shift in the opposite direction. Nonetheless, the two spin states which are degenerate at B = 0 T are split progressively as the magnetic field is increased. It is also apparent that both spin states are shifted toward higher energies. This diamagnetic shift is a second order effect due to the additional magnetic moment created by the carrier motion. In fact, the external magnetic field induces a rotation of the charged particles at the cyclotron frequency: [80]

$$\omega_c = \frac{eB}{m^*} \qquad \text{IV-5}$$

where m^* is the effective mass of the carrier in the semiconductor material. This rotational motion creates a magnetic moment anti-parallel to the external field and the resulting magnetic potential energy is therefore positive. More precisely, the diamagnetic shift of the exciton in the QD is given by: [72,81]

$$\Delta E_{diamag} = \frac{e^2}{8}\left(\frac{\left\langle x_e^2 + y_e^2\right\rangle}{m_e^*} + \frac{\left\langle x_h^2 + y_h^2\right\rangle}{m_h^*}\right)B^2 \qquad \text{IV-6}$$

where $\left\langle x^2 + y^2\right\rangle$ is a measure of the spatial extent of the carrier wavefunction in the x-y plane. In Figure IV-4 a), the solid line is a quadratic fit of the mean value between the two spin states, demonstrating the B^2 dependence of the shift throughout the magnetic field range.

In Figure IV-4 b), the energy splitting between the spin states is plotted as a function of field and a g-factor value of $\left|g_{exc}^*\right| = 0.52$ is obtained according to equation IV-4. This effective g-factor value depends on the individual dot. For example, comparably small g-factors were obtained when measuring similar dots (indium flush at 5 nm), while dots with a smaller height (indium flush at 3 nm) had larger g-factor values.[72] The dependence of the g-factor on dot material as well as dot size and shape has been well established experimentally [82-84] and theoretically [85-88]. It occurs from redefining the g-factor in QDs as an effective value which accounts for the spin and orbital angular momentum of the carriers. Since the SO interaction depends on the dot material through the Dresselhaus coupling as well as the dot size and shape through the Rashba coupling, the effective g-factor of the carriers in the ground state is dependent on the particular dot properties. A theoretical model which takes into account the SO coupling to calculate the emission energies from all QD states will be presented in section 4.2.1.

a)

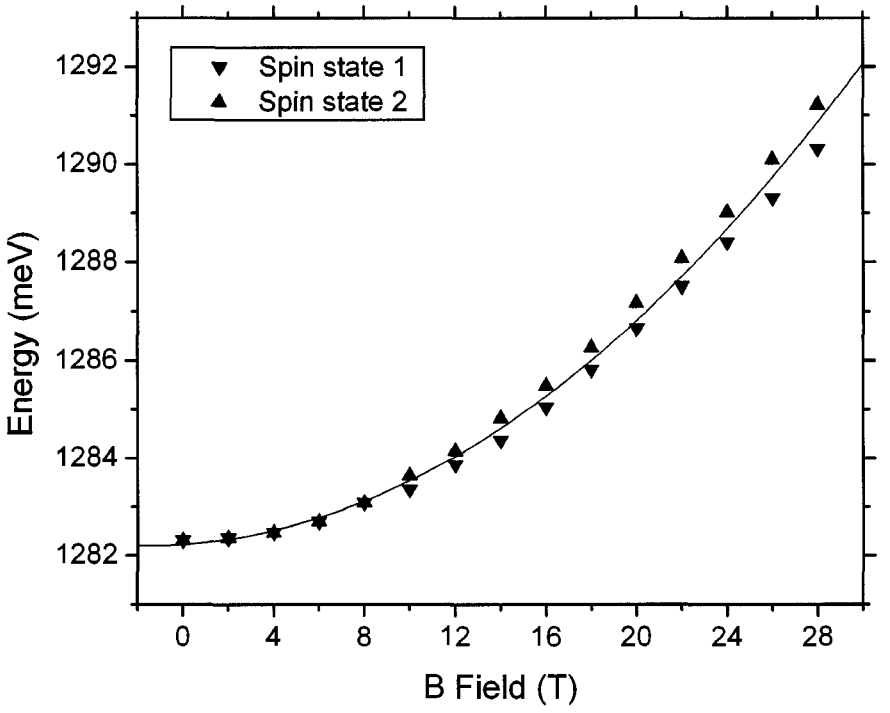

b)

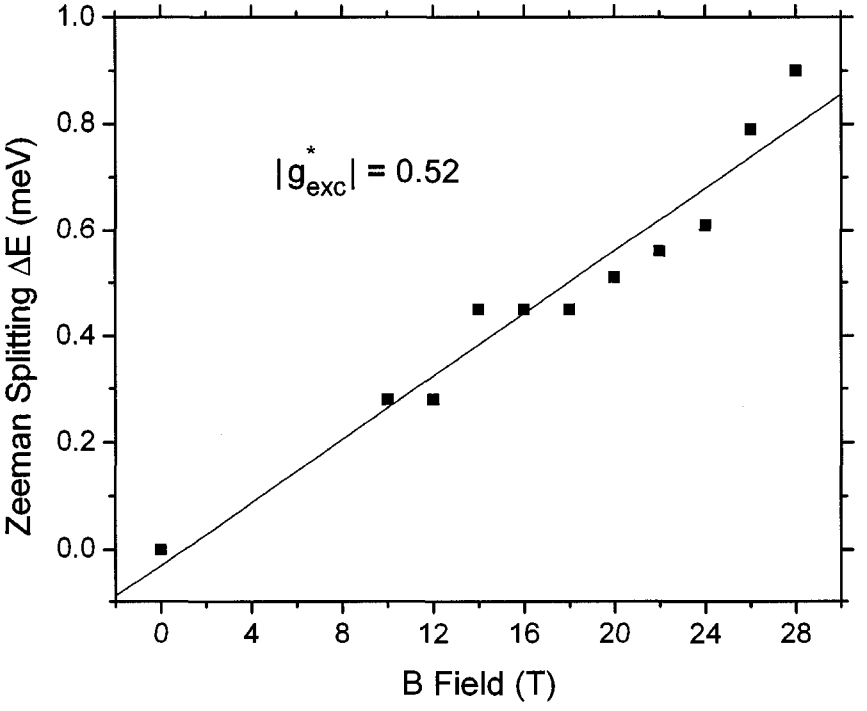

Figure IV-4 Effect of magnetic field on the ground state spin. The results reveal a) the diamagnetic shift and b) the Zeeman spin splitting.

4.1.3 Excited State Emission

In order to observe the QD shell structure, one must detect the emission from the excited states of the QD. These states have degeneracies which are lifted when a magnetic field is applied perpendicularly to the QD plane. At 0 T, the different orbital angular momentum states are grouped in shells according to the total number of quanta from both harmonic oscillators. In the magnetic field, the magnetic moment created by the orbital motion of the carriers interacts with the external field and the resulting potential energy alters the emission energy. As the magnetic field is increased, the states will shift differently depending on their orbital angular momentum. A first series of measurements was taken at high excitation power density in order to detect intense emission from the excited states. The PL spectrum of the investigated SQD is shown in Figure IV-5 without any external magnetic field. The spectrum reveals emission from the first 4 excited states, which are labelled p, d, f and g shells in order of increasing energy, as well as the tail from the WL emission. A high pump power is needed to fill the lower energy states and thus obtain intense emission from the excited states. This inadvertently creates a system of many excitons in the dot, which leads to various occupied state configurations and complex many-body effects. The broadening produced by the multi-exciton system effectively flattens the emission peak from the s-shell, and somewhat flattens the p-shell emission peak. Because of the statistical fluctuations in the dot carrier population, there are many variations of initial and final exciton configurations in which an exciton can recombine radiatively. Hence, there are many possible energies associated with the recombination of an exciton in a particular state. In addition, the s-shell emission intensity is relatively weak since lower energy shells have smaller degeneracies, implying a lower exciton population which translates into a reduced photon generation rate when all shells are filled. For example, a filled s-shell contains 2 excitons whereas a filled d-shell contains 6 excitons. The radiative recombination rate will therefore be greater in the d-shell.

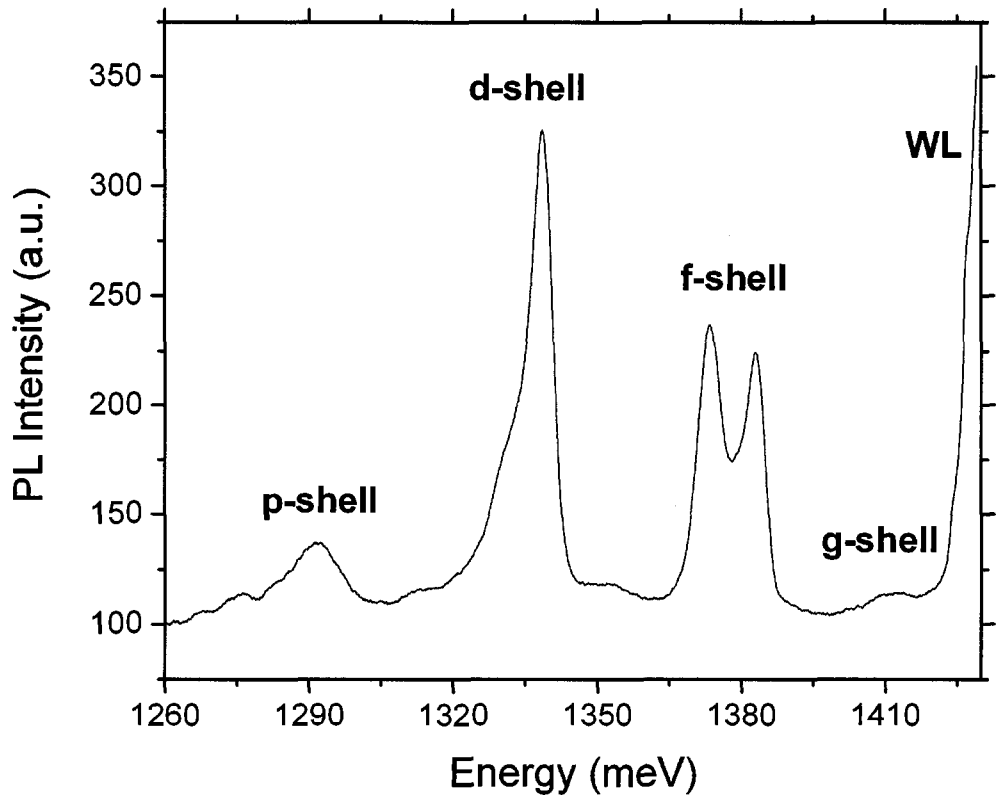

Figure IV-5 High excitation power PL of SQD. The spectrum reveals emission from the first 4 excited states, which are labelled p, d, f and g shells in order of increasing energy, as well as the tail from the WL emission.

Figure IV-6 a) shows the magnetic field evolution of the PL spectrum in the form of a waterfall. The PL spectra were measured at every Tesla up to 28 T. Given the significant broadening from many-body effects, it is difficult to resolve the different peaks in the spectra. For that reason, a second derivative algorithm (see Appendix B) is applied to the data in order to extract the location of each peak. In fact, the peaks are better defined in Figure IV-6 b), for which the spectra are plotted using the second derivative data. It should be noted that the smoothing method used in the second derivative algorithm was also applied to the data of Figure IV-5 and Figure IV-6 a) in order to reduce the noise.

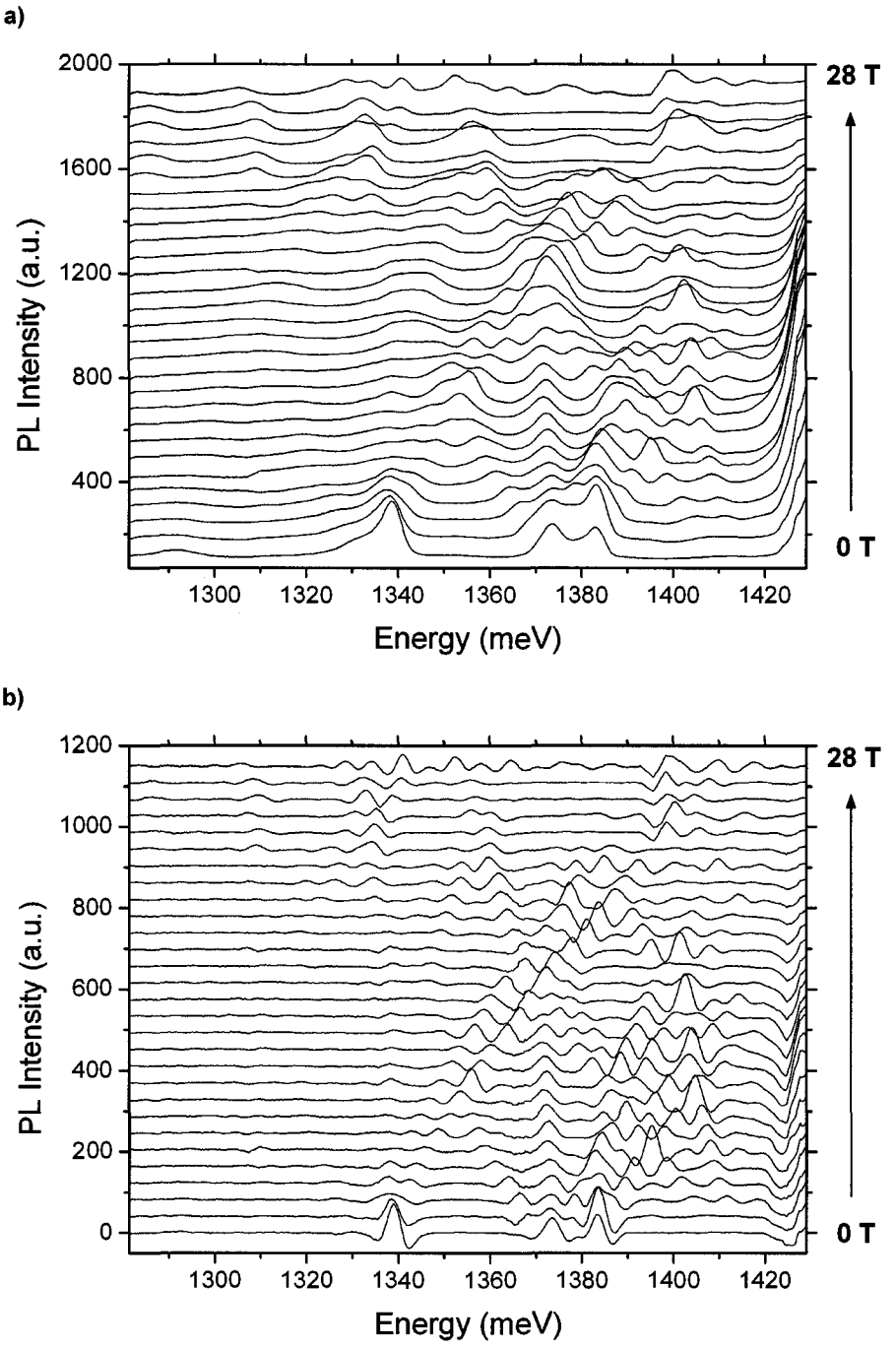

Figure IV-6 Waterfalls of high excitation power M-PL spectra. The results are presented with a) data smoothing only and b) data smoothing with a second derivative algorithm.

The magnetic field evolution of the PL emission can also be presented in the form of a surface plot. Figure IV-7 shows the 0 T PL spectrum on the left and the

surface plot on the right describes the evolution of the emission energy in magnetic fields up to 28 T. The surface plot is formed by building a grid from the series of PL measurements and then displaying the emission intensity on a colour scale. In this case, blue corresponds to the lowest emission intensities while the highest intensities are displayed in yellow. The range of intensities in between the extremes is represented by a scale of blended colours. In order to reveal the weak emission intensities at low emission energies, a different color scale is used for energies below 1335 meV.

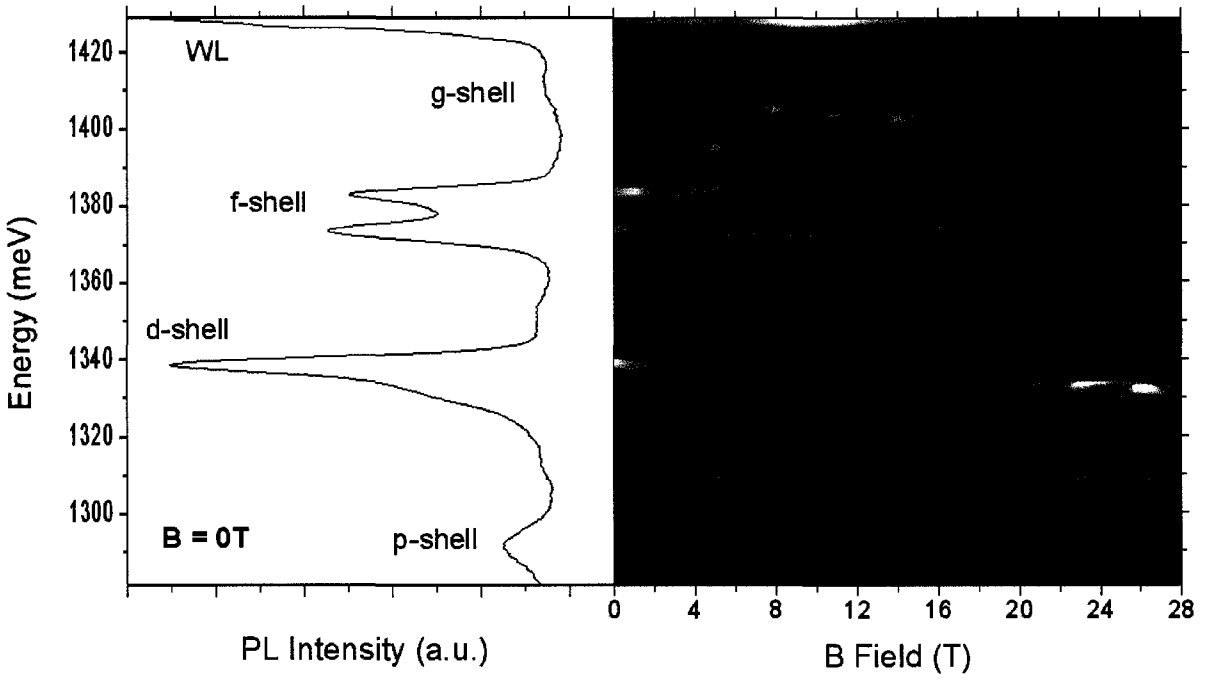

Figure IV-7 Contour plot of high excitation power M-PL next to 0 T PL spectrum. Blue corresponds to the lowest emission intensities while the highest intensities are displayed in yellow.

The assignment of PL peaks to particular shells is confirmed by the number of branches which emerge from the degenerate shell states. In fact, it is clear that the d-shell splits into 3 branches and the f-shell splits into 4 branches, as is expected from the FD model. Only the upper branch of the p-shell and the two lowest branches of the g-shell can be observed in the surface plot. Since the g-shell

is near to the WL continuum, the other states of the g-shell become unbound as the magnetic field is increased. Conversely, the lower branches of higher shells appear in the surface plot as their energy is shifted below the WL continuum. An important difference between the experimental results of Figure IV-7 and the FD spectrum is the presence of different energy peaks within the same shell at zero-field. In fact, a clear zero-field splitting is observed within the d and f shells. The FD model, which implies a perfect parabolic confinement potential, predicts a shell configuration with degenerate states at 0 T. The zero-field splitting can be attributed to potential or size asymmetry in the QD, which breaks the in-plane circular symmetry of the potential.[33] Also observed in the PL spectra is the occurrence of two distinct emission peaks for certain branches. This is most apparent for the two positive angular momentum branches of the f-shell and the positive angular momentum branch of the d-shell. The distinct peaks could be attributed to a Zeeman splitting; however, the splitting is not as significant for other states and considerably larger than the Zeeman splitting observed in the s-shell of similar dots.

Another series of M-PL measurements was taken at intermediate excitation intensity. The laser intensity is once again sufficient to fill the lower energy states and induce recombination in excited states, yet it is set lower than for the previous PL measurements. As a result, the average carrier population in the QD is smaller and there is less fluctuation of exciton configurations. The multi-particle broadening is thus less significant and the peak resolution is improved, particularly in the case of the s and p shells. The zero-field PL spectrum of the SQD is shown in Figure IV-8 and the emission peaks are associated to the 3 lowest energy shells.

The magnetic field was swept up to 26 T and the M-PL measurements were taken at 1 T increments. In this excitation regime, the peaks can be resolved without the second derivative algorithm and the raw data was accordingly used to produce the surface plot of Figure IV-9. The results resemble closely the simple FD spectrum with 1, 2 and 3 branches for the s, p and d shells, respectively. With increasing magnetic field, the lower angular momentum states of the f and g shells

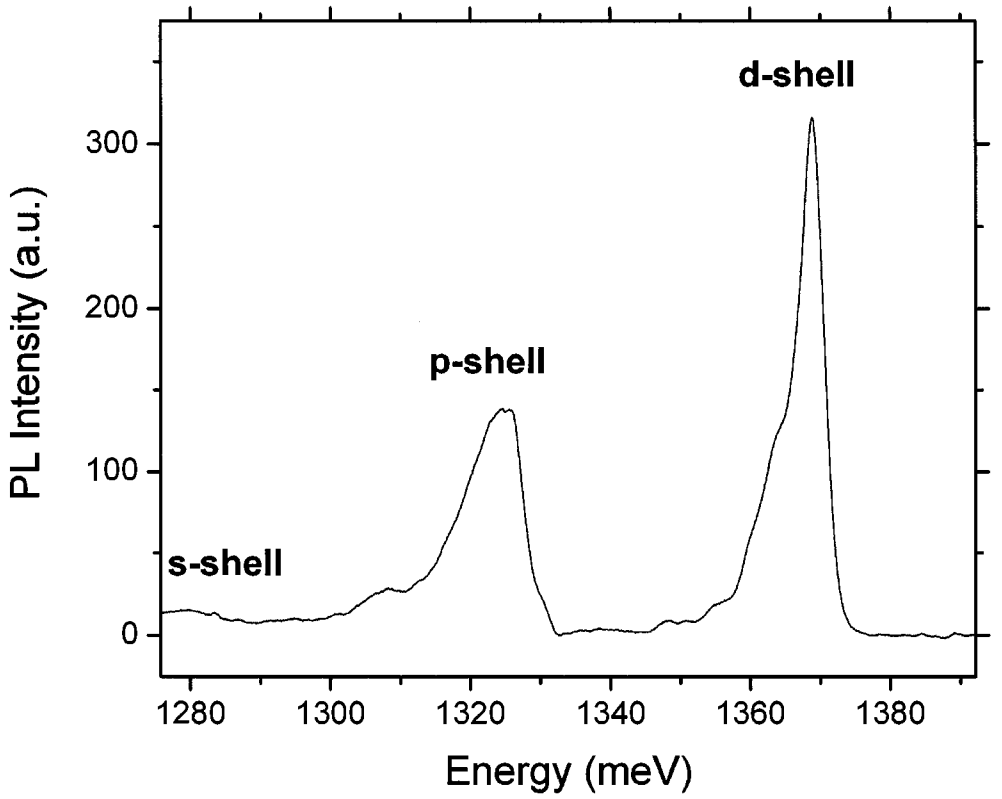

Figure IV-8 Medium power PL spectrum of SQD without an external magnetic field. The spectrum reveals emission from the 3 lowest energy shells, which are labelled s, p and d shells in order of increasing energy.

emerge into the investigated energy range. The spectrum evolution has the characteristic diamond like level crossings and the branches can unambiguously be assigned to specific FD states. However, as with the previous series of M-PL measurements, the branches are not degenerate at zero-field and it is also apparent that each branch consists of two distinct lines whose magnetic field evolution cannot be explained by a simple Zeeman spin splitting. For instance, the upper branches of the p and d shells have two lines that split progressively with increasing field, whereas the lower branches have two lines that seem to converge, which can be seen especially well from the lower branch of the f-shell. The dependence of the splitting on orbital state suggests that this behaviour could be related to SO interaction.

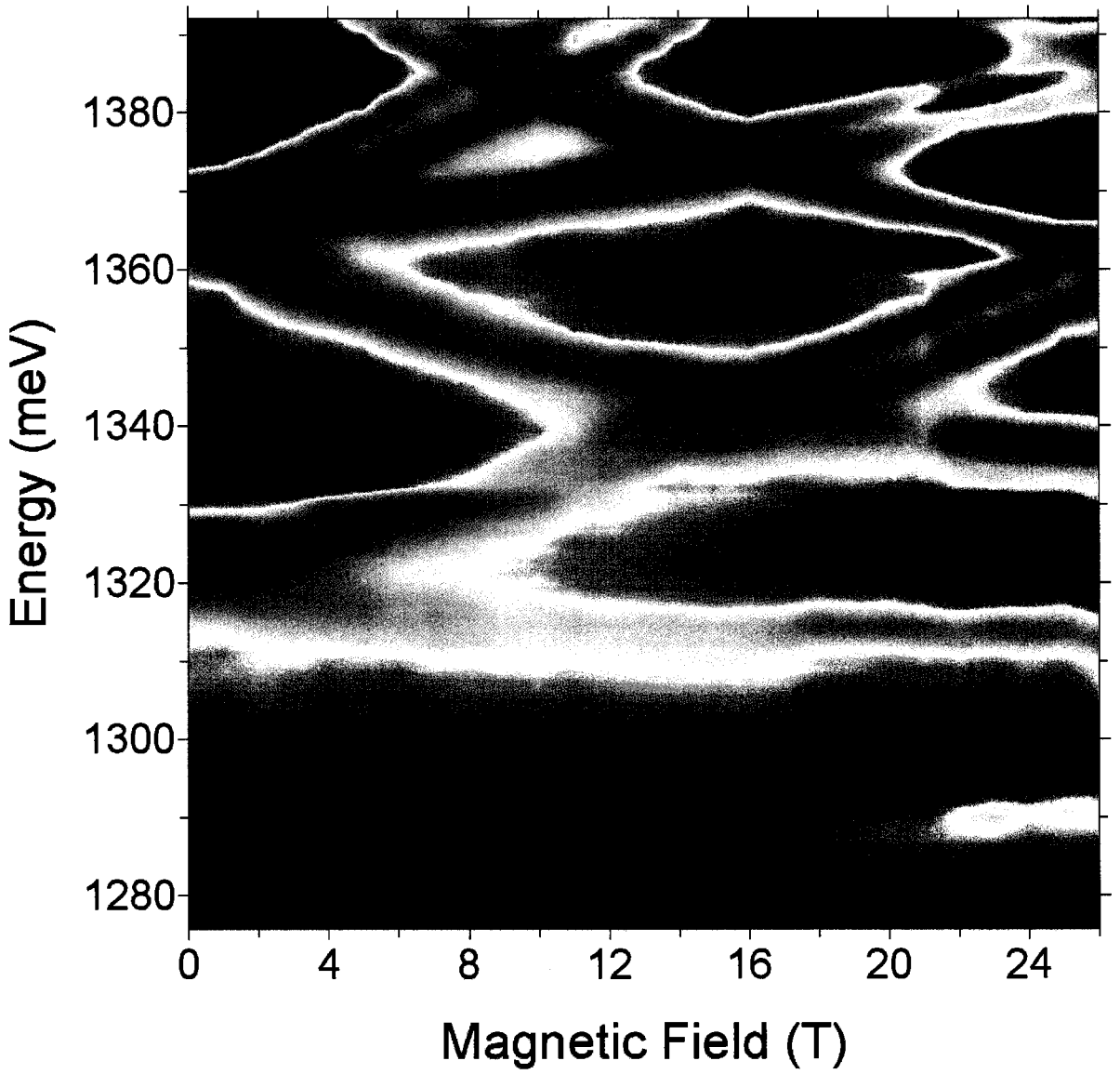

Figure IV-9 Contour plot of M-PL with medium excitation power. The plot is formed by merging 4 spectral windows. In order of increasing intensity, the emission is represented by blue, yellow, orange and red.

Another possible explanation to the splitting of branches in magnetic field would be many-body effects. In such a confined system of charged particles, interactions undoubtedly come into play. Since the doublets are separated by 5-10 meV throughout the magnetic field range and exchange energies are typically within 10 meV, this explanation merits further investigation. Many-body calculations show

that the shifts due to exchange and correlation effects are usually toward lower energies.[51] As the excitation power is increased, the lower energy peak of the doublets would therefore be expected to appear after the higher energy peak. In fact, many-body interactions have a greater impact on the transition energies of a certain state when higher energy states are occupied. In view of that, power dependent PL measurements were taken in static magnetic fields in order to study the effect of carrier population on the PL spectrum. For technical reasons, another QD had to be used for these experiments. A series of M-PL measurements was initially taken at a fixed excitation power to confirm the same splitting behaviour in this particular QD. Although the results presented in Figure IV-10 are not as clear as previous results, mostly because the magnetic field increment is now 2 T, the same dependence of the splitting on orbital state is still apparent. As with the first series of high power measurements, the broadening from many-body interactions effectively flattens the s-shell peak.

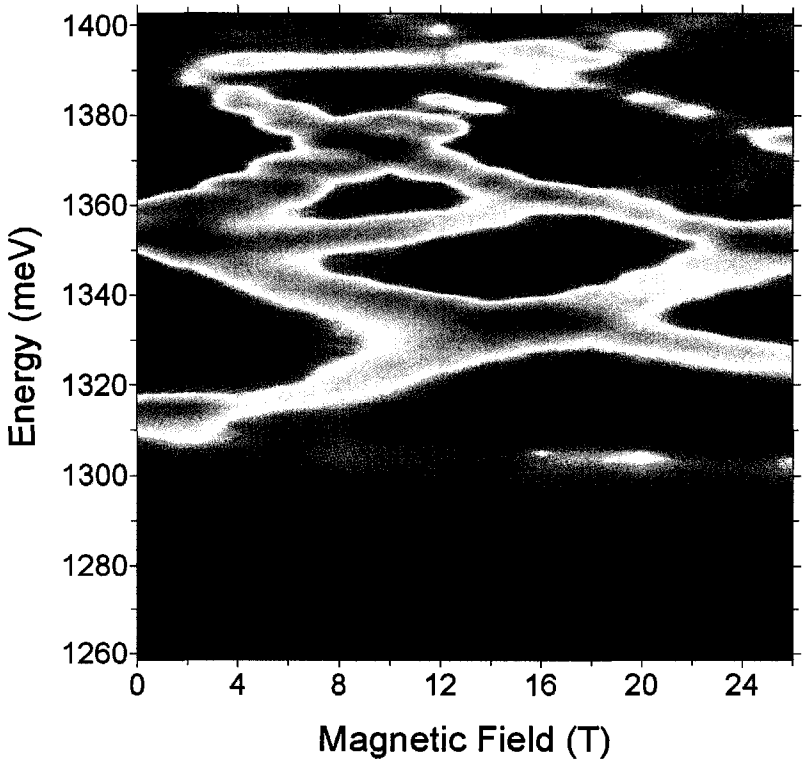

Figure IV-10 Contour plot of M-PL with medium excitation power. The spectra were taken every 2 T.

The power dependent measurements were taken at 3 different magnetic fields. In Figure IV-11 a), the magnetic field is fixed at 6 T and the shell degeneracy has clearly been lifted as each PL peak can be assigned to a different orbital state. In particular, the d+ state is well isolated and it is apparent that it consists of a doublet. The doublet peaks appear in the PL spectrum following the filling of lower states and their emission intensity increases gradually as the excitation power is increased. Moreover, the higher energy peak, which is very weak when the doublet first appears, becomes more intense with respect to the lower energy peak. The same behaviour is observed for the p+ doublet at 22 T, as shown in Figure IV-11 c). At the highest excitation power, the higher energy peak actually becomes more intense than the other peak. At 16 T, new degeneracies are formed as the states cross together. Once again, the power dependence of Figure IV-11 b) demonstrates the same effect. As the excitation power is ramped up, peak intensities increase and the peaks broaden toward lower energies until they become flat. This consistent behaviour is indicative of normal state filling, which suggests that the doublets are not due to many-body effects but rather different spin states. Since adding a simple Zeeman splitting to the FD model cannot explain the increased splitting of upper branches in magnetic field whilst lower branches show reduced splitting, a more sophisticated model including SO interactions must be considered.

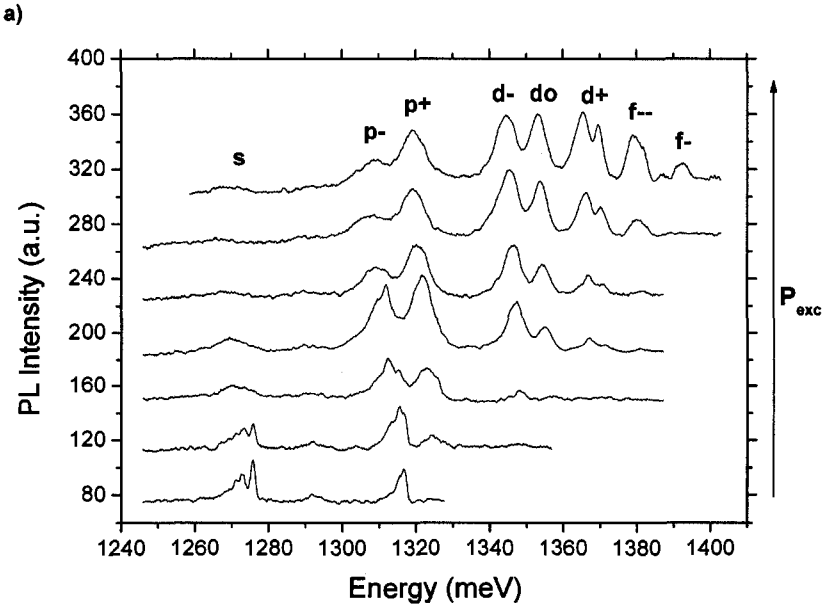

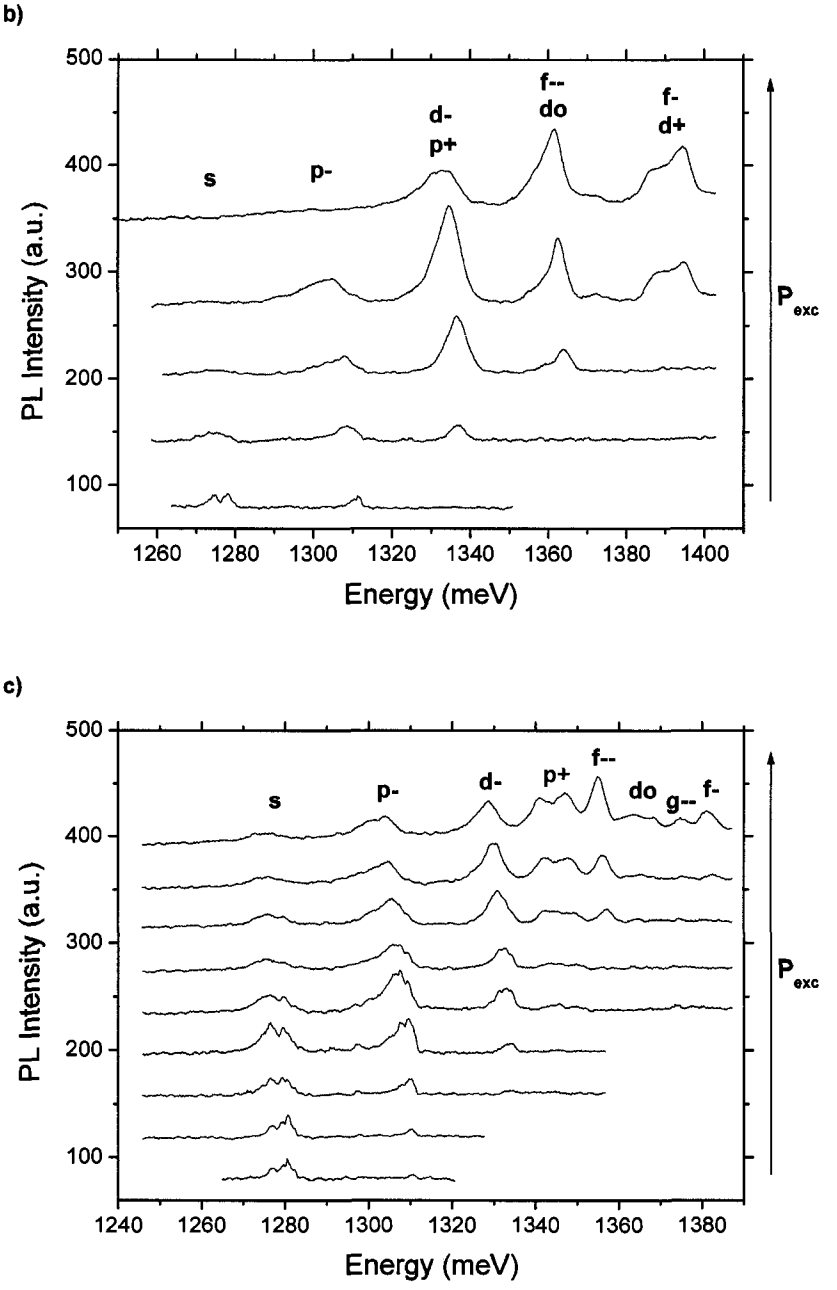

Figure IV-11 Power dependence of PL from a SQD in magnetic field. The spectra were taken at a) 6 T, b) 16 T and c) 22 T.

4.2 Spin-Orbit Interaction

The application of a magnetic field perpendicular to the lateral potential plane of the QD lifts the shell degeneracy and the orbital angular momentum states split according to the FD scheme. By isolating a SQD, the inhomogeneous broadening from a distribution of dot sizes and compositions is eliminated and the fine structure of the spectrum is revealed. As a result, it is apparent that each angular momentum branch consists of two distinct lines whose magnetic field evolution cannot be explained by a simple Zeeman spin splitting. In fact, the splitting clearly depends on the orbital state; with the positive angular momentum branches having lines that diverge with increasing field and the negative angular momentum branches having lines that first converge until they cross. This behaviour, along with the shell splitting at zero-field, can be explained by the addition of SO coupling, Zeeman spin splitting and size anisotropy to the FD model.

4.2.1 Spin-Orbit Model

SO coupling is the interaction of a particle's spin with its motion. The physical origin of the coupling can be understood as a relativistic effect of the particle's orbital motion in a static electric field. From special relativity [46], in the rest frame of a particle moving with velocity $\vec{v}$ in an external electric field $\vec{E}$ there will appear a magnetic field $\vec{B}$ given (to first order in v/c) by:

$$\vec{B} = -\frac{1}{c^2}\vec{v} \times \vec{E} \qquad \text{IV-7}$$

A well-known example is the SO coupling which occurs in atoms as a consequence of interaction between the electron's spin and its motion in the electric field produced by the nucleus' positive charge. This coupling leads to the fine structure splitting of the electron's atomic energy levels. Although there is no

magnetic field in the rest frame of the nucleus, there is one in the rest frame of the electron. The magnetic moment $\vec{\mu} = q\vec{\sigma}/m_e$ associated with the spin of the electron will interact with this magnetic field resulting in a magnetic potential energy:

$$W = -\vec{\mu} \cdot \vec{B} \qquad \text{IV-8}$$

For the electron in the hydrogen atom, the electric field is described by:

$$\vec{E} = -\frac{1}{q}\frac{dV(r)}{dr}\frac{\vec{r}}{r} \qquad \text{IV-9}$$

where $V(r) = -e^2/r$ is the electrostatic energy of the electron. Since the electron velocity is equal to $\vec{p}/m_e$, the magnetic field can be rewritten as:

$$\vec{B} = \frac{1}{m_e q c^2}\frac{1}{r}\frac{dV(r)}{dr}\vec{p} \times \vec{r} \qquad \text{IV-10}$$

From classical mechanics, the angular momentum of a particle is given by $\vec{L} = \vec{r} \times \vec{p}$ which therefore gives:

$$W = \frac{1}{m_e^2 c^2}\frac{1}{r}\frac{dV(r)}{dr}\vec{L} \cdot \vec{\sigma} \qquad \text{IV-11}$$

To a factor of $1/2$, this is the expression for the SO term in the Hamiltonian of the hydrogen atom. The absence of the factor is due to the fact that the motion of the electron around the proton is not rectilinear and uniform which leads to an effect called the Thomas precession.[89]

For a particle in a semiconductor material, the SO interaction occurs as a result of the particle's motion in the electric field produced by the semiconductor. In a zincblende crystal structure such as InAs or GaAs, there are two types of

contributions to the SO coupling: the bulk inversion asymmetry (BIA) which was first considered by Dresselhaus and the structure inversion asymmetry (SIA). The BIA is an intrinsic contribution due to the effective electric field caused by the microscopic crystal potential. The SIA contribution is caused by the inversion asymmetry of the macroscopic, i.e. slowly varying on the scale of the lattice parameter, interface or confinement potential. In the case of a 2D vertical confinement potential, the SIA contribution is known as the Rashba effect. In a QD structure, there is an additional SIA term owing to the inversion asymmetry of the lateral confinement potential. An external electric field, for example from applying gate voltages to the semiconductor structure, will also effect the SIA contribution to the SO coupling. For simplicity, the following will include all SIA contributions in the Rashba term. The electronic SO model was developed by M. Valín-Rodríguez et al. in references 90 (Dresselhaus effect only) and 91 (both SO effects). The main expressions are derived here by generalizing the model to both electron and hole particles. From there, selection rules for optical transitions are considered to determine the excitonic energies which are of interest in PL experiments.

The model neglects all multi-particle effects by considering a single charged particle of effective mass m_β^* confined in the x-y plane by the potential $V^\beta(\mathbf{r})$; where β stands for electron or hole. The dot deformation can be accounted for by considering an anisotropic lateral potential:

$$V^\beta(\mathbf{r}) = \tfrac{1}{2} m_\beta^* (\omega_{\beta x}^2 x^2 + \omega_{\beta y}^2 y^2) \qquad \text{IV-12}$$

The single-particle Hamiltonian contains the confinement energy, the Rashba and Dresselhaus SO terms, and the Zeeman energy:

$$H = H_0 + H_R + H_D + H_Z \qquad \text{IV-13}$$

When the confinement energy is much greater than the SO terms, one may use

unitary transformations yielding an effective diagonal SO term to obtain analytical solutions.[91] As in the FD model, the parabolic lateral potential gives harmonic oscillator solutions, with an added Zeeman energy term. The eigenvalues for each spin η depend on the number of quanta in each oscillator:

$$E^{\beta}_{N_1N_2\eta} = \pm\left[(N_1+\tfrac{1}{2})\hbar\Omega^{\beta}_{1\eta} + (N_2+\tfrac{1}{2})\hbar\Omega^{\beta}_{2\eta}\right] + \tfrac{1}{2}s_\eta g^*_\beta \mu_B B_z \qquad \text{IV-14}$$

where ± has a positive (negative) sign for electrons (holes), g^*_β is the bulklike effective g-factor and $s_\eta = \pm 1$ for $\eta = \uparrow, \downarrow$. The frequencies $\Omega^{\beta}_{k\eta}$ of the two ($k = 1,2$) decoupled oscillators are:

$$\Omega^{\beta}_{k\eta} = \frac{1}{\sqrt{2}}\left[\omega^2_{\beta x} + \omega^2_{\beta y} + \omega^2_{\beta\eta c} \pm \sqrt{(\omega^2_{\beta x} + \omega^2_{\beta y} + \omega^2_{\beta\eta c})^2 - 4\omega^2_{\beta x}\omega^2_{\beta y}}\right]^{\frac{1}{2}} \qquad \text{IV-15}$$

where the upper (lower) sign in ± corresponds to $k = 1\ (2)$. The electron cyclotron frequency has been renormalized to include the SO coupling:

$$\omega_{e\eta c} = \frac{eB_z}{m^*_e} + (\lambda^2_D - \lambda^2_R)\frac{2m^*_e}{\hbar^3}s_\eta \qquad \text{IV-16}$$

where the coupling constants λ_R and λ_D determine the Rashba and Dresselhaus SO strengths, respectively. For the hole, SO coupling leads to the splitting into light and heavy hole states, after which the spin is frozen in one direction and coupling with the particle motion does not occur.[92] As a consequence, the heavy hole states are FD states with the additional size anisotropy and Zeeman spin splitting, i.e.:

$$\omega_{h\eta c} = \frac{eB_z}{m^*_h} \qquad \text{IV-17}$$

As discussed in chapter II, electronic transitions are subject to selection rules that restrict the allowed exciton recombinations to those involving electrons and holes with the same number of quanta in each oscillator. As a result, the electron orbital angular momentum is $L^e = N_1 - N_2$ whereas the hole has opposite orbital angular momentum $L^h = N_2 - N_1$, and the total orbital angular momentum of the exciton is null. In order to conserve total angular momentum, the emitted photon must acquire one unit of angular momentum from the charge carriers' spin. For heavy hole excitons, the hole spin $J_h = \frac{3}{2}$ has a projection along the z-axis $J_{h,z} = \pm\frac{3}{2}$ and the electron spin $S_e = \frac{1}{2}$ has $S_{e,z} = \pm\frac{1}{2}$. The exciton states with total angular momentum projections $M = S_{e,z} + J_{h,z} = \pm 1$ can couple to the light field. The electron and hole therefore have opposite spin projections in the optically active exciton state. The excitonic (X) spectrum is thus built from the difference between electron and hole energies $E^e_{N_1N_2\eta=\uparrow,\downarrow} - E^h_{N_1N_2\eta=\downarrow,\uparrow}$. An offset energy E_0 comprising the QD material energy gap and the vertical confinement energy must also be added to the exciton recombination energy. For an exciton state $|N_1N_2\eta\rangle$, where η is defined as the electron spin, the emission energy is:

$$E^X_{N_1N_2\eta} = E_0 + (N_1 + \tfrac{1}{2})\hbar\Omega^X_{1\eta} + (N_2 + \tfrac{1}{2})\hbar\Omega^X_{2\eta} + \tfrac{1}{2}s_\eta(g^*_e + g^*_h)\mu_B B_z \qquad \text{IV-18a}$$

$$\Omega^X_{k\uparrow} = \Omega^e_{k\uparrow} + \Omega^h_{k\downarrow} \;\; ; \;\; \Omega^X_{k\downarrow} = \Omega^e_{k\downarrow} + \Omega^h_{k\uparrow} \qquad \text{IV-18b}$$

In a strained InAs/GaAs QD, the electron effective mass becomes close to the electron mass in GaAs and the value $m^*_e = 0.067m_e$ is accordingly used in the model.[93,94] Empirical pseudopotential and *ab initio* local density calculations predict a heavy hole mass of $m^*_h = 0.590m_e$.[95] In a semiconductor, the effective g-factor of the electron is altered from the free electron value of $g \cong 2$ as a result of SO coupling. In the bulk material, the interaction of electron motion with the lattice

potential leads to a renormalization of the g-factor. For moving electrons, the crystal electric field yields an effective magnetic field which couples to the spin magnetic moment. These bulklike effects are included in the formula for conduction-band g-factor: [96,97]

$$g = 2 - \frac{2E_p \Delta_{so}}{3E_g(E_g + \Delta_{so})} \qquad \text{IV-19}$$

where Δ_{so} is the SO splitting defining the energy difference between heavy and light hole states, $E_p = 2\langle S|P_x|X\rangle^2 / m_e$ is the Kane energy involving the momentum matrix element between the s-type conduction band and p-type valence band, and E_g is the band gap energy including the vertical confinement energy. For InAs material [94], the parameters are Δ_{so} = 0.39 eV, E_p = 21.5 eV and E_g = 1.243 eV for the measured dot. This gives an effective electron g-factor g_e^* = -0.75 in the dot material. This value does not include the additional SO effects from the dot strain and confinement potential as this coupling intensity is adjusted through the SO constants of the model. Experimental results on similar SAQDs agree with theoretical calculations that suggest a zero g-factor for holes.[77] Accordingly, an excitonic g-factor $g_{exc}^* = g_e^* + g_h^* = -0.75$ is used in the calculations. The deformation ratio $\delta = \omega_{\beta y} / \omega_{\beta x}$, the offset energy as well as the electron and hole potential strength $\hbar(\omega_{\beta x} + \omega_{\beta y})/2$ were adjusted to fit the experimental results. A SO intensity of $\lambda_D^2 - \lambda_R^2$ = -(3.86×10^{-11} eV m)^2 was then obtained by minimizing the divergence between experimental and calculated results (see Appendix C). All of the model parameters are recapitulated in Table IV-1.

Parameter	Description	Value
m_e^*	Electron effective mass	0.067 m_e
m_h^*	Heavy hole effective mass	0.590 m_e
g_{exc}^*	Bulklike effective g-factor of exciton	-0.75
δ	Dot deformation ratio	0.95
$\hbar(\omega_{ex}+\omega_{ey})/2$	Electron potential strength	35.4 meV
$\hbar(\omega_{hx}+\omega_{hy})/2$	Hole potential strength	7.4 meV
E_0	Offset energy from band gap and vertical confinement	1238 meV
$\lambda_D^2-\lambda_R^2$	SO intensity	$-(3.86\times10^{-11}$ eV m$)^2$

Table IV-1 Parameters in the SO model. The effective masses and bulklike effective g-factor were taken from literature while the dot deformation ratio, the potential strengths, the offset energy and the SO intensity were adjusted to fit the experimental results.

4.2.2 Discussion

All the model parameters have now been determined, either from literature or by optimization to fit the experimental results. Figure IV-12 compares the calculated energies (lines) to the experimental results (circles), where experimental peak positions were extracted using a second-derivative algorithm. Although the SO coupling alone will introduce zero-field splitting, adding potential anisotropy to the model was needed to explain the significant separations. However, a single exciton model with potential anisotropy and Zeeman spin splitting alone cannot reproduce the observed results. In order to demonstrate that claim, the evolution of emission energies in magnetic field is illustrated for both models in Figure IV-13. The general behaviour of the model which includes SO coupling is clearly more similar to the

experimental results. The evolution of each doublet depends on the angular momentum of that branch. The branches with zero or positive angular momentum L^e have a doublet separation that gradually increases with field. Moreover, the separation is greater for states with more angular momentum and for same angular momentum states that are in higher energy shells. For the negative angular momentum branches, the lines appear to be initially separated and they converge together with increasing field until they form a unique peak. Furthermore, the separation depends on the orbital state. For fields between 5 and 10 T, the separation is greater as the angular momentum L^e is more negative. The dependence of the splitting on orbital state is a clear indication of SO interaction in the dot.

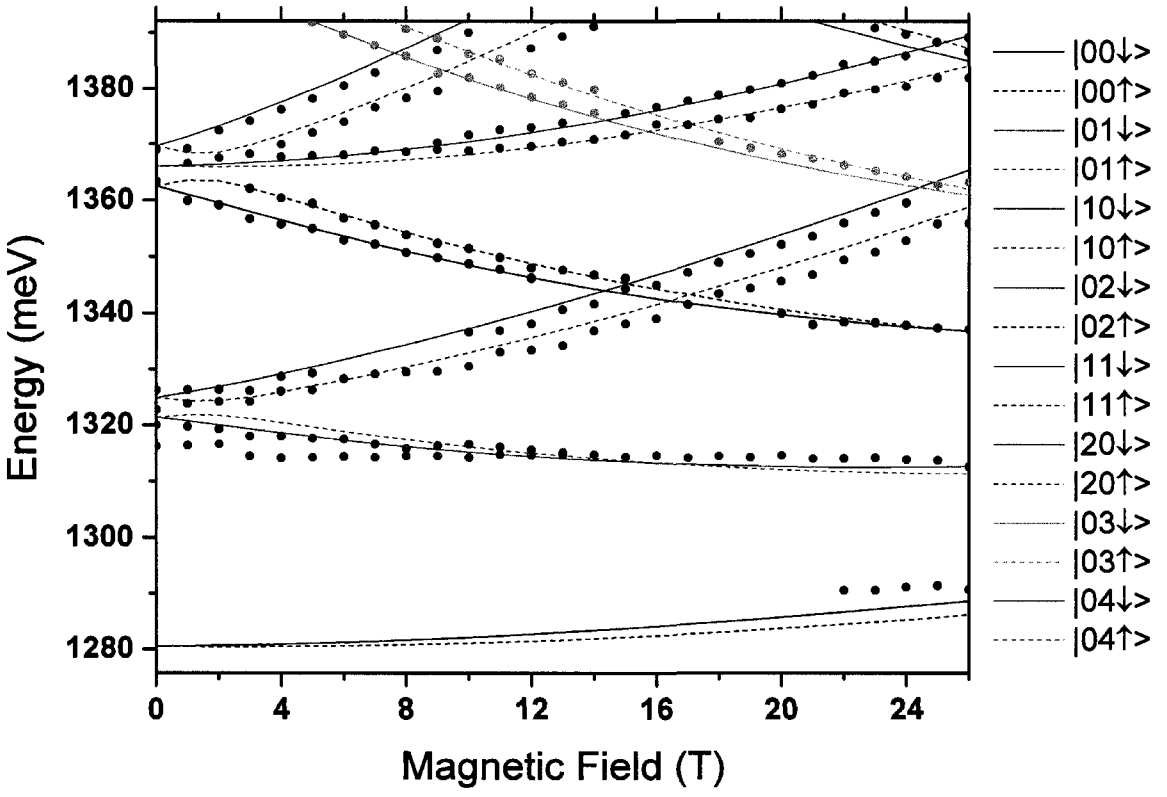

Figure IV-12 Calculated and experimental QD emission energy in magnetic field. Note that the theoretical results would be exactly the same if the sign of both the g-factor and the SO intensity were inversed, except that the spin orientations would all be inversed. The experimental spin states therefore remain ambiguous.

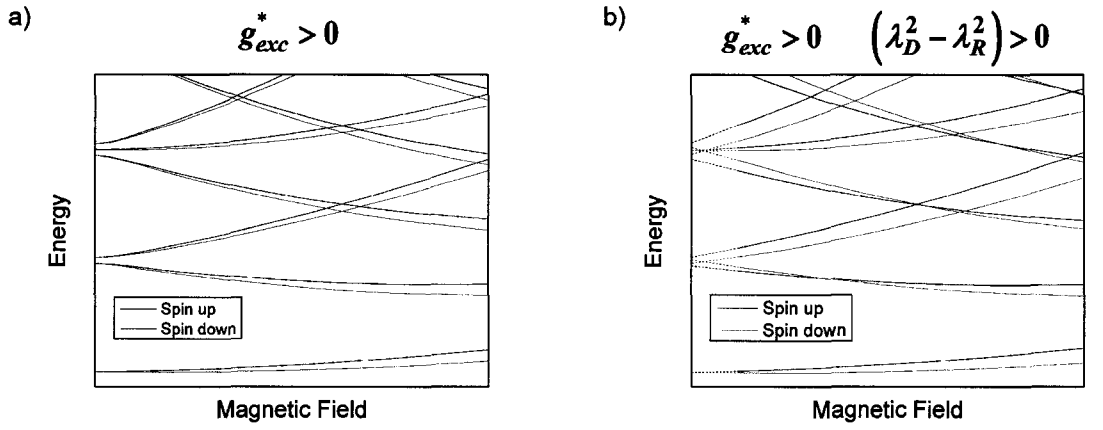

Figure IV-13 Theoretical evolution of the QD emission energy in magnetic field. The energies are calculated according to the FD model with a) a potential anisotropy and Zeeman spin splitting only and b) a potential anisotropy, Zeeman spin splitting and SO coupling.

In general, there is good agreement between experimental and theoretical results. The main features of the M-PL measurements are captured by the single exciton model. The most important discrepancy occurs in the s-shell emission with the experimental peak maxima being at higher energies than the calculated results. However, the s-shell signal is relatively weak and broadened toward lower energies, which might explain the disagreement. The calculated spin splitting in the s-shell (2.5 meV at 26 T) is larger than what is observed in low excitation power measurements (0.6 meV at 26 T). If no additional SO coupling is included in the calculation, the ground state spin splitting is 1.1 meV at 26 T, which suggests that the model should not include SO interaction for the s-shell since the conduction band electrons have zero orbital angular momentum from both the envelope and Bloch function. The bulklike effects on the effective g-factor have been accounted for in the value of g_e^* used in the model. In the QD, the effective g-factor is further modified by SO coupling through the strain and confinement potential. The SO intensity determined from the model calculations is therefore a measure of this added SO coupling. The SO interaction modifies the precessional frequency of the dot particles from the Larmor frequency $\omega_L = |g|\mu_B B/\hbar$ to a different value depending on the orbital state of the particles. The altered precessional energy is

equal to the difference between the spin-up and spin-down particle energies for a given angular momentum state, and its magnetic field dependence is related to the SO intensity. The effective g-factor values reported in the literature are determined from this altered precessional energy which will depend on dot size and shape as a consequence of variation in SO intensity.

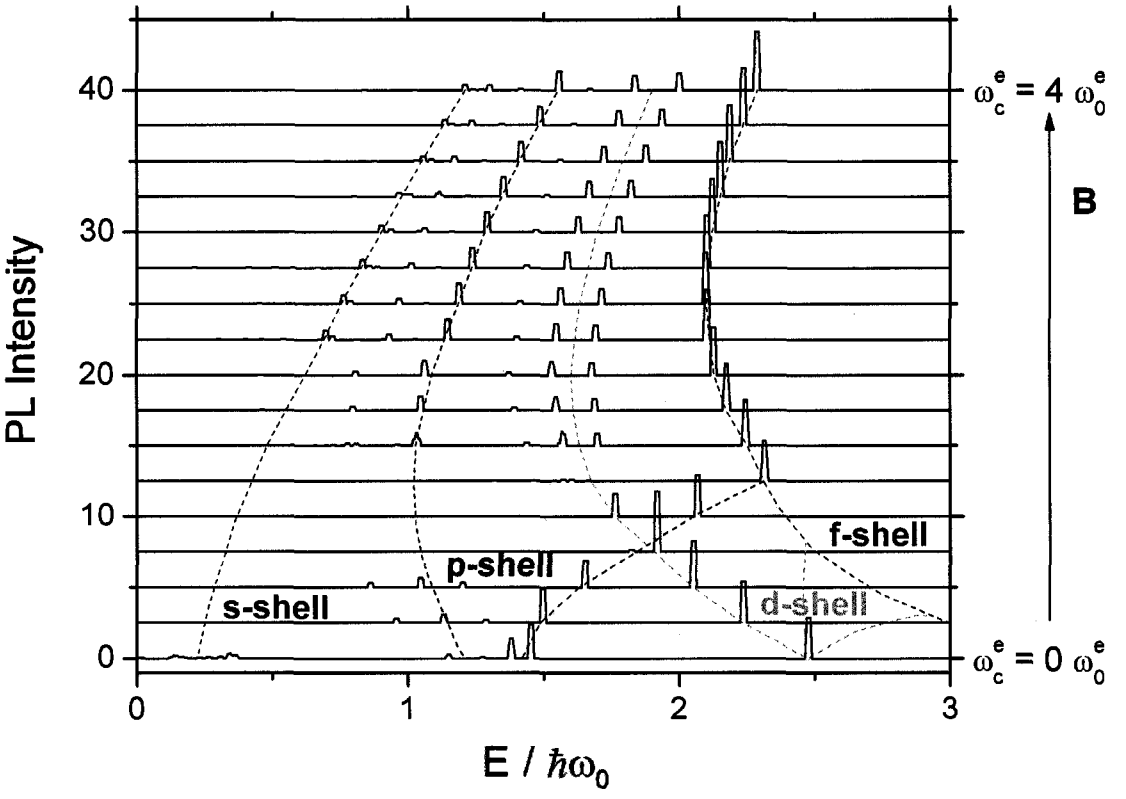

Figure IV-14 Intensity of QD emission from theoretical calculations including many-body effects. The magnetic field dependent spectra were calculated for a QD system initially containing 8 excitons. The peak splittings differ depending on the number of excitons in the QD, but the behaviour observed in experimental results was not reproduced for any number of initial excitons.

Many-body effects do not need to be considered in order to explain the results. It should nonetheless be noted that the broadening observed at high excitation powers is attributed to different exciton complexes and charge states. Conversely, many-body effects could offer another possible explanation to the doublet evolution since the emission lines are separated by 5-10 meV throughout

the magnetic field range and exchange energies are typically within 10 meV. However, the power dependent measurements performed in magnetic field indicate that the doublet states follow a normal filling effect. Moreover, preliminary calculations (see Figure IV-14) reveal that the exchange energy splittings do not have the same behaviour in magnetic field. Correlation energies are not expected to alter the M-PL features significantly as they essentially renormalize all the exciton energies. For those reasons, a more apposite interpretation of the results is that exchange and Coulomb interaction energies are small and they lead to the broadening of peaks (3-4 meV) representing each state $|N_1 N_2 \eta\rangle$. The SQD PL results of section 3.2.2 (see in particular Figure III-8) showed that one can indeed expect a broadening of 3-4 meV from many-body effects. The SO interaction is therefore the higher order effect which can be resolved in the spectra.

It is considered that the largest parameter uncertainty in the theoretical model originates from the effective excitonic g-factor g^*_{exc} in the bulklike dot material. The boundary values of 0 and -5 found in reference 88 for QDs of different geometry emitting at the same ground state energy are therefore used to determine an uncertainty on the SO intensity. For both g^*_{exc} values, the SO intensity is adjusted through a series of iterations in order to minimize the variations between experimental and theoretical results. Boundary values of SO intensity are thus obtained, which can be interpreted as a rough estimate to the uncertainty limits. From that reasoning, the SO intensity is $\lambda_D^2 - \lambda_R^2$ = -((3.9±0.3)×10^{-11} eV m)^2. The negative sign suggests a dominating Rashba term, which is consistent with theoretical [98] and experimental results on InAs quantum wells, with reported values of $\lambda_D^2 - \lambda_R^2$ = -(0.9×10^{-11} eV m)^2 [99] and ratio λ_R / λ_D = 2.15 [100]. The Rashba coupling is due to the SIA, whereas the Dresselhaus coupling is due to the BIA. A lack of symmetry in the lateral confinement potential defining a QD introduces an additional interface electric field not present in quantum wells, and the Rashba term can thus be expected to have an even greater contribution in InAs QDs.

Chapter V: Conclusion

In this project, the electronic properties of QDs were studied by means of optical measurements and theoretical modeling. By applying a magnetic field perpendicular to the lateral potential plane, the shell degeneracy was lifted and M-PL therefore provided a probe to analyze the energy shell structure of QDs. The broadening produced by an inhomogeneous distribution of dot sizes and compositions was eliminated by isolating a SQD. As a result, it was possible to observe effects which have never before been reported. In fact, the experimental results obtained in this project are the first observation of SO coupling effects on the electronic structure of SAQDs.

To begin with, dot ensemble measurements were taken in order to obtain information on the overall dot population of the sample. After annealing, the QD energy levels were shifted toward higher energies and the spacing between energy levels was reduced. The dot ensemble PL spectra contained separate peaks originating from the various QD shells. As the excitation power was increased, state filling lead to increased emission from the excited states. In order to observe the fine structure of individual dots, a mask was used to cover the sample surface, leaving only a pattern of nano holes which allow optical access to the QDs. By mapping the mask pattern, a number of holes were found to contain only a SQD. The high resolution PL spectrum of a SQD contained a few narrow lines even at very low excitation power. These lines were attributed to different exciton complexes and charge states. However, a more thorough power dependence and polarization-dependent measurements would be required in order to identify the peaks with more certainty. Also, field-effect measurements could provide additional information with respect to the nature of each peak. If gate voltages were applied to the semiconductor, one could control the charges inside the QD. Not only could this allow one to verify the origin of the peaks associated with charge states, but it should also make it possible to reduce the number of extra charges within the dot.

In fact, applying an electric field would flush out the unpaired charged particles from the dot layer, thus decreasing the probability of extra charges being captured within the QD potential. Therefore, this proposed gate voltage experiment might reduce the broadening from many-body effects, as less charged particles would result in less possible configurations. Although at this point the peaks cannot be unambiguously identified, the characteristic peak pattern was observed in many spectra. This is strong evidence that the peaks are due to different configurations and the pattern can accordingly be associated to emission from a SQD.

M-PL measurements were taken at different excitation powers in order to study the QD emission with different carrier populations. First, low excitation power measurements were taken in order to obtain only a few emission peaks in the ground state. The magnetic field dependence then revealed the diamagnetic shift and the Zeeman spin splitting of all peaks. In order to observe emission from the excited states, the lower energy states must be filled, which implies the presence of multiple excitons in the QD potential. This multi-exciton system inadvertently leads to many-body interactions which significantly perturb the single particle energies. As a result, the PL spectra which were measured at higher excitation powers had considerable peak broadening. It was determined that each peak could be associated to a specific state and the peak broadening of 3-4 meV was due to many-body interactions. The M-PL results resembled closely the simple FD spectrum with 1, 2, 3 and 4 branches emerging from the s, p, d and f shells, respectively. However, for each series of measurements, it was apparent that each branch consisted of two distinct lines whose magnetic field evolution cannot be explained by a simple Zeeman spin splitting. The results revealed a dependence of spin states on orbital angular momentum. In fact, the positive angular momentum branches had lines that diverged with increasing magnetic field while the negative angular momentum branches had lines that first converged until they crossed. This behaviour is well explained by the effect of SO coupling. In fact, the experimental results could be described by adding SO coupling, Zeeman spin splitting and dot size anisotropy to the FD model. Some of the model parameters were taken from

literature while others were optimized to fit the experimental results. Accordingly, a SO intensity of $\lambda_D^2 - \lambda_R^2$ = -((3.9±0.3)×10^{-11} eV m)^2 was obtained. The negative sign suggests a dominating Rashba term, meaning that the SIA contribution to SO coupling is greater than the BIA contribution. This result is consistent with experiments on InAs quantum wells.

In conclusion, it has been shown that the emission spectrum of a SQD in magnetic field resembles the FD spectrum. By including SO coupling, Zeeman spin splitting and dot size anisotropy to the FD model, the calculated energies are in good agreement with the experimental results. The occurrence of doublets and the dependence of the splitting on orbital state are strong indications of SO interaction in the dot. The SO intensity was calculated and it was determined that the Rashba coupling is dominating.

Bibliography

1. G. E. Moore, *Cramming more components onto integrated circuits*, Electronics, Vol. 38, No. 8, April 19 (1965)
2. R. Compaño, L. Molenkamp, and D. J. Paul (Microelectronics Advanced Research Initiative), *Technology Roadmap for Nanoelectronics*, European Commission's IST Programme on Future and Emerging Technologies (1999 Edition)
3. http://cam.qubit.org (Centre for Quantum Computation, University of Cambridge)
4. K.-J. Lee, J.-S. Park, and H. Shin, *Quantum effects in CMOS devices*, Journal of the Korean Physical Society, Vol. 41, No. 6, pp. 902-907 (2002)
5. R. Dingle and C. H. Henry, *Quantum Effects in Heterostructure Lasers*, U.S. Patent 3 982 207 (1976)
6. Y. Arakawa and H. Sakaki, *Multidimensional quantum well laser and temperature dependence of its threshold current*, Applied Physics Letters, Vol. 40, No. 11, pp. 939-941 (1982)
7. M. Asada, Y. Miyamoto, and Y. Suematsu, *Gain and the threshold of three-dimensional quantum-box lasers*, IEEE Journal of Quantum Electronics, Vol. 22, No. 9, pp. 1915-1921 (1986)
8. C. H. Bennett and G. Brassard, *Quantum cryptography: public key distribution and coin tossing*, Proc. IEEE International Conference on Computers, Systems, and Signal Processing, Piscataway, NJ: IEEE, pp. 175-9 (1984)
9. A. K. Ekert, *Quantum cryptography based on Bell's theorem*, Physical Review Letters, Vol. 67, No. 6, pp. 661-663 (1991)
10. D. P. DiVincenzo, *Quantum computation*, Science, Vol. 270, No. 5234, pp. 255-261 (1995)
11. P. W. Shor, Polynomial-time algorithms for prime factorization and discrete logarithms on a quantum computer, SIAM Journal on Computing, Vol. 26, No. 5, pp. 1484-1509 (1997)
12. D. Bouwmeester, A. Ekert, and A. Zeilinger, *The Physics of Quantum Information*, Berlin: Springer (2000)
13. D. D. Awschalom, D. Loss, and N. Samarth, *Semiconductor Spintronics and Quantum Computation*, Berlin: Springer (2002)
14. T. H. Stievater, X. Li, D. G. Steel, D. Gammon, D. S. Katzer, D. Park, C. Piermarocchi, and L. J. Sham, *Rabi oscillations of excitons in single quantum dots*, Physical Review Letters, Vol. 87, No. 13, 133603 (2001)
15. A. Zrenner, E. Beham, S. Stufler, F. Findeis, M. Bichler, and G. Abstreiter, *Coherent properties of a two-level system based on a quantum-dot photodiode.*, Nature, Vol. 418, No. 6898, pp. 612-614 (2002)
16. H. Htoon, T. Takagahara, D. Kulik, O. Baklenov, A. L. Holmes, and C. K. Shih, *Interplay of Rabi oscillations and quantum interference in semiconductor quantum dots*, Physical Review Letters, Vol. 88, No. 8, 087401 (2002)
17. S. A. Wolf and D. D. Awschalom, *Spintronic: A spin-based electronics vision for the future*, Science, Vol. 294, No. 5546, pp. 1488-1495 (2001)
18. http://nobelprize.org (Nobel Foundation)
19. S. Datta and B. Das, *Electronic analog of the electro-optic modulator*, Applied Physics Letters, Vol. 56, No. 7, pp. 665-667 (1990)

20. Y. A. Bychkov and E. I. Rashba, *Oscillatory effects and the magnetic susceptibility of carriers in inversion layers*, Journal of Physics C, Vol. 17, No. 33, pp. 6039-6045 (1984)

21. G. Dresselhaus, *Spin-orbit coupling effects in zinc blende structures*, Physical Review, Vol. 100, No. 2, pp. 580-586 (1955)

22. J. Schliemann, J. C. Egues, and D. Loss, *Nonballistic spin-field-effect transistor*, Physical Review Letters, Vol. 90, No. 14, 146801 (2003)

23. L. Wissinger, U. Rössler, R. Winkler, B. Jusserand, and D. Richards, *Spin splitting in the electron subband of asymmetric GaAs/$Al_xGa_{1-x}As$ quantum wells: The multiband envelope function approach*, Physical Review B, Vol. 58, No. 23, pp. 15375-15377 (1998)

24. A. V. Moroz and C. H. W. Barnes, Effect of the spin-orbit interaction on the band structure and conductance of quasi-one-dimensional systems, Physical Review B, Vol. 60, No. 20, pp. 14272-14285 (1999)

25. C.-M. Hu, J. Nitta, T. Akazaki, H. Takayanagi, J. Osaka, P. Pfeffer, and W. Zawadzki, Zero-field spin splitting in an inverted $In_{0.53}Ga_{0.47}As/In_{0.52}Al_{0.48}As$ heterostructure: Band nonparabolicity influence and the subband dependence, Physical Review B, Vol. 60, No. 11, pp. 7736-7739 (1999)

26. D. Richards and B. Jusserand, *Spin energetics in a GaAs quantum well: Asymmetric spin-flip Raman scattering*, Physical Review B, Vol. 59, No. 4, pp. R2506-R2509 (1999)

27. E. Silveira, M. K. Kelly, C. E. Nebel, G. Bohm, G. Abstreiter, and M. Stutzmann, *Spin splitting in GaAs quantum wire structures*, Physica E, Vol. 2, No. 1-4, pp. 929-932 (1998)

28. C. F. Destefani et al., *Spin-orbit coupling and intrinsic spin mixing in quantum dots*, Physical Review B, Vol. 69, No. 12, 125302 (2004); *Spin-orbit and electronic interactions in narrow-gap quantum dots*, Physical Review B, Vol. 70, No. 20, 205315 (2004); *Anisotropic electron g factor in quantum dots with spin-orbit interaction*, Physical Review B, Vol. 71, No. 16, 161303 (2005)

29. M. Valín-Rodríguez et al., Electronic spin precession in semiconductor quantum dots with spin-orbit coupling, Physical Review B, Vol. 66, No. 23, 235322 (2002); Zeeman energy and anomalous spin splitting in lateral GaAs quantum dots., European Physical Journal B, Vol. 39, No. 1, pp. 87-92 (2004); Model for spin-orbit effects in two-dimensional semiconductors in magnetic fields, Physical Review B, Vol. 73, No. 23, 235306 (2006)

30. J. Lee, H. N. Spector, W. C. Chou, and C. S. Chu, *Rashba spin splitting in parabolic quantum dots*, Journal of Applied Physics, Vol. 99, No. 11, pp. 113708 (2006)

31. S. Raymond, S. Studenikin, A. Sachrajda, Z. Wasilewski, S. J. Cheng, W. Sheng, P. Hawrylak, A. Babinski, M. Potemski, G. Ortner, and M. Bayer, *Excitonic energy shell structure of self-assembled InGaAs/GaAs quantum dots*, Physical Review Letters, Vol. 92, No. 18, 187402 (2004)

32. A. Babinski, M. Potemski, S. Raymond, J. Lapointe, and Z. R. Wasilewski, *Emission from a highly excited single InAs-GaAs quantum dot in magnetic fields: An excitonic Fock-Darwin diagram*, Physical Review B, Vol. 74, No. 15, 155301 (2006)

33. A. Babinski, S. Raymond, J. Lapointe, and Z. R. Wasilewski, *Fock-Darwin spectrum of a single InAs/GaAs quantum dot*, physica status solidi (c), Vol. 3, No. 11, pp. 3748-3751 (2006)

34. P. K. Bhattacharya and N. K. Dutta, *Quantum Well Optical Devices and Materials*, Annual Review of Materials Science, Vol. 23, pp. 79-123 (1993)

35. A. Y. Cho and J. R. Arthur, *Molecular beam epitaxy*, Progress in Solid State Chemistry, Vol. 10, No. Part 3, pp. 157-191 (1975)

36. D. Bimberg, M. Grundmann, and N. N. Ledentsov, *Quantum Dot Heterostructures*, Chichester, England: Wiley (1999)

37. E. Bauer, *Phaenomenologische theorie der kristallabscheidung an oberflaechen,* Zeitschrift für Kristallographie, Vol. 110, pp. 372-394 (1958)

38. Z. R. Wasilewski, S. Fafard, and J. P. McCaffrey, *Size and shape engineering of vertically stacked self-assembled quantum dots*, Journal of Crystal Growth, Vol. 201-202, pp. 1131-1135 (1999)

39. C. Kittel, *Introduction to Solid State Physics*, 8th Edition, Hoboken, NJ: Wiley (2005)

40. G. Bastard, Wave Mechanics Applied to Semiconductor Heterostructures, New York: Wiley (1988)

41. E. O. Kane, *Semiconductors and Semimetals*, Volume 1, New York: Academic Press (1966)

42. F. Boxberg and J. Tulkki, *Theory of the electronic structure and carrier dynamics of strain-induced (Ga, In)As quantum dots*, Reports on Progress in Physics, Vol. 70, No. 8, pp. 1425-1471 (2007)

43. D. Morris, N. Perret, and S. Fafard, *Carrier energy relaxation by means of Auger processes in InAs/GaAs self-assembled quantum dots*, Applied Physics Letters, Vol. 75, No. 23, pp. 3593-3595 (1999)

44. L. Jacak, P. Hawrylak, and A. Wojs, *Quantum Dots*, Berlin: Springer (1998)

45. F. Vallée and F. Bogani, *Coherent time-resolved investigation of LO-phonon dynamics in GaAs*, Physical Review B, Vol. 43, No. 14, pp. 12049-12052 (1991)

46. C. Cohen-Tannoudji, B. Diu, and F. Laloë, *Mécanique Quantique*, Paris: Hermann (1977)

47. S. Raymond, *Zero-Dimensional Properties of Self-Assembled Islands*, Ph.D. Thesis, University of Ottawa (1997)

48. L. Marchildon, *Mécanique Quantique*, Brussels: De Boeck Université (2000)

49. A. J. Williamson, A. Franceschetti, and A. Zunger, *Multi-excitons in self-assembled InAs/GaAs quantum dots: A pseudopotential, many-body approach*, Europhysics Letters, Vol. 53, No. 1, pp. 59-65 (2001)

50. S. Tarucha, D. G. Austing, T. Honda, R. J. van der Hage, and L. P. Kouwenhoven, *Shell filling and spin effects in a few electron quantum dot*, Physical Review Letters, Vol. 77, No. 17, pp. 3613-3616 (1996)

51. P. Hawrylak, *Excitonic artificial atoms: Engineering optical properties of quantum dots*, Physical Review B, Vol. 60, No. 8, pp. 5597-5608 (1999)

52. J. C. Slater, *Quantum Theory of Atomic Structure*, Volume 2, New York: McGraw-Hill (1960)

53. V. Fock, *Bemerkung zur quantelung des harmonischen oszillators in magnetfeld*, Zeitschrift für Physik A, Vol. 47, No. 5-6, pp. 446-448 (1928)

54. C. G. Darwin, *The diamagnetism of the free electron*, Proceedings of the Cambridge Philosophical Society, Vol. 27, 86 (1930)

55. http://en.wikipedia.org (Wikipedia, Wikipedia Foundation)

56. R. Leon, Y. Kim, C. Jagadish, M. Gal, J. Zou, and D. J. H. Cockayne, *Effects of interdiffusion on the luminescence of InGaAs/GaAs quantum dots*, Applied Physics Letters, Vol. 69, No. 13, pp. 1888-1890 (1996)

57. C. Lobo, R. Leon, S. Fafard, and P. G. Piva, *Intermixing induced changes in the radiative emission from III--V quantum dots*, Applied Physics Letters, Vol. 72, No. 22, pp. 2850-2852 (1998)

58. R. Leon, S. Fafard, P. G. Piva, S. Ruvimov, and Z. Liliental-Weber, *Tunable intersublevel transitions in self-forming semiconductor quantum dots*, Physical Review B, Vol. 58, No. 8, pp. R4262-R4265 (1998)

59. S. Fafard and C. N. Allen, *Intermixing in quantum-dot ensembles with sharp adjustable shells*, Applied Physics Letters, Vol. 75, No. 16, pp. 2374-2376 (1999)

60. A. Babinski, J. Jasinski, R. Bozek, A. Szepielow, and J. M. Baranowski, *Rapid thermal annealing of InAs/GaAs quantum dots under a GaAs proximity cap*, Applied Physics Letters, Vol. 79, No. 16, pp. 2576-2578 (2001)

61. P. Harrison, Quantum Wells, Wires and Dots: Theoretical and Computational Physics, Chichester, England: Wiley (2000)

62. S. Grosse, J. H. H. Sandmann, G. von Plessen, J. Feldmann, H. Lipsanen, M. Sopanen, J. Tulkki, and J. Ahopelto, *Carrier relaxation dynamics in quantum dots: Scattering mechanisms and state-filling effects*, Physical Review B, Vol. 55, No. 7, pp. 4473-4476 (1997)

63. S. Raymond, X. Guo, J. L. Merz, and S. Fafard, *Excited-state radiative lifetimes in self-assembled quantum dots obtained from state-filling spectroscopy*, Physical Review B, Vol. 59, No. 11, pp. 7624-7631 (1999)

64. S. Fafard, Z. R. Wasilewski, C. N. Allen, D. Picard, M. Spanner, J. P. McCaffrey, and P. G. Piva, *Manipulating the energy levels of semiconductor quantum dots*, Physical Review B, Vol. 59, No. 23, pp. 15368-15373 (1999)

65. A. Wojs and P. Hawrylak, Theory of photoluminescence from modulation-doped self-assembled quantum dots in a magnetic field, Physical Review B, Vol. 55, No. 19, pp. 13066-13071 (1997)

66. D. Hessman, P. Castrillo, M.-E. Pistol, C. Pryor, and L. Samuelson, *Excited states of individual quantum dots studied by photoluminescence spectroscopy*, Applied Physics Letters, Vol. 69, No. 6, pp. 749-751 (1996)

67. L. Landin, M. S. Miller, M.-E. Pistol, C. E. Pryor, and L. Samuelson, *Optical studies of individual InAs quantum dots in GaAs: Few-particle effects.*, Science, Vol. 280, No. 5361, pp. 262-264 (1998)

68. J. J. Finley, P. W. Fry, A. D. Ashmore, A. Lemaître, A. I. Tartakovskii, R. Oulton, D. J. Mowbray, M. S. Skolnick, M. Hopkinson, P. D. Buckle, and P. A. Maksym, *Observation of multicharged excitons and biexcitons in a single InGaAs quantum dot*, Physical Review B, Vol. 63, No. 16, 161305 (2001)

69. M. Baier, F. Findeis, A. Zrenner, M. Bichler, and G. Abstreiter, *Optical spectroscopy of charged excitons in single quantum dot photodiodes*, Physical Review B, Vol. 64, No. 19, 195326 (2001)

70. E. S. Moskalenko, K. F. Karlsson, P. O. Holtz, B. Monemar, W. V. Schoenfeld, J. M. Garcia, and P. M. Petroff, *Influence of excitation energy on charged exciton formation in self-assembled InAs single quantum dots*, Physical Review B, Vol. 64, No. 8, 085302 (2001)

71. N. I. Cade, H. Gotoh, H. Kamada, T. Tawara, T. Sogawa, H. Nakano, and H. Okamoto, *Charged exciton emission at 1.3 mu m from single InAs quantum dots grown by metalorganic chemical vapor deposition*, Applied Physics Letters, Vol. 87, No. 17, 172101 (2005)

72. A. Babinski, G. Ortner, S. Raymond, M. Potemski, M. Bayer, W. Sheng, P. Hawrylak, Z. Wasilewski, S. Fafard, and A. Forchel, *Ground-state emission from a single InAs/GaAs self-*

assembled quantum dot structure in ultrahigh magnetic fields, Physical Review B, Vol. 74, No. 7, 075310 (2006)

73. N. I. Cade, H. Gotoh, H. Kamada, H. Nakano, and H. Okamoto, Fine structure and magneto-optics of exciton, trion, and charged biexciton states in single InAs quantum dots emitting at 1.3 mu m, Physical Review B, Vol. 73, No. 11, 115322 (2006)

74. M. Bayer, G. Ortner, O. Stern, A. Kuther, A. A. Gorbunov, A. Forchel, P. Hawrylak, S. Fafard, K. Hinzer, T. L. Reinecke, S. N. Walck, J. P. Reithmaier, F. Klopf, and F. Schäfer, *Fine structure of neutral and charged excitons in self-assembled In(Ga)As/(Al)GaAs quantum dots*, Physical Review B, Vol. 65, No. 19, 195315 (2002)

75. V. D. Kulakovskii, G. Bacher, R. Weigand, T. Kümmell, A. Forchel, E. Borovitskaya, K. Leonardi, and D. Hommel, *Fine structure of biexciton emission in symmetric and asymmetric CdSe/ZnSe single quantum dots*, Physical Review Letters, Vol. 82, No. 8, pp. 1780-1783 (1999)

76. D. V. Regelman, E. Dekel, D. Gershoni, E. Ehrenfreund, A. J. Williamson, J. Shumway, A. Zunger, W. V. Schoenfeld, and P. M. Petroff, *Optical spectroscopy of single quantum dots at tunable positive, neutral, and negative charge states*, Physical Review B, Vol. 64, No. 16, 165301 (2001)

77. W. Sheng and A. Babinski, *Zero g factors and nonzero orbital momenta in self-assembled quantum dots*, Physical Review B, Vol. 75, No. 3, 033316 (2007)

78. C. E. Pryor and M. E. Flatte, *Landé g factors and orbital momentum quenching in semiconductor quantum dots*, Physical Review Letters, Vol. 96, No. 2, pp. 026804 (2006)

79. H. W. van Kesteren, E. C. Cosman, W. A. J. A. van der Poel, and C. T. Foxon, *Fine structure of excitons in type-II GaAs/AlAs quantum wells*, Physical Review B, Vol. 41, No. 8, pp. 5283-5292 (1990)

80. K. Gottfried and T.-M. Yan, *Quantum Mechanics: Fundamentals, 2nd Edition*, New York: Springer (2003)

81. I. E. Itskevich, M. Henini, H. A. Carmona, L. Eaves, P. C. Main, D. K. Maude, and J. C. Portal, *Photoluminescence spectroscopy of self-assembled InAs quantum dots in strong magnetic field and under high pressure*, Applied Physics Letters, Vol. 70, No. 4, pp. 505-507 (1997)

82. I. Hapke-Wurst, U. Zeitler, R. J. Haug, and K. Pierz, *Mapping the g factor anisotropy of InAs self-assembled quantum dots*, Physica E, Vol. 12, No. 1-4, pp. 802-805 (2002)

83. G. Medeiros-Ribeiro, E. Ribeiro, and H. Westfahl Jr, *g-factor engineering and control in self-assembled quantum dots.*, Applied Physics A, Vol. 77, No. 6, pp. 725-729 (2003)

84. M. Bayer, V. B. Timofeev, T. Gutbrod, A. Forchel, R. Steffen, and J. Oshinowo, *Enhancement of spin splitting due to spatial confinement in $In_xGa_{1-x}As$ quantum dots*, Physical Review B, Vol. 52, No. 16, pp. R11623-R11625 (1995)

85. T. Darnhofer and U. Rössler, *Effects of band structure and spin in quantum dots*, Physical Review B, Vol. 47, No. 23, pp. 16020-16023 (1993)

86. A. A. Kiselev, E. L. Ivchenko, and U. Rössler, *Electron g factor in one- and zero-dimensional semiconductor nanostructures*, Physical Review B, Vol. 58, No. 24, pp. 16353-16359 (1998)

87. S. J. Prado, C. Trallero-Giner, A. M. Alcalde, V. Lopez-Richard, and G. E. Marques, *Influence of quantum dot shape on the Landé g-factor determination*, Physical Review B, Vol. 69, No. 20, 201310 (2004)

88. T. Nakaoka, T. Saito, J. Tatebayashi, and Y. Arakawa, *Size, shape, and strain dependence of the g factor in self-assembled In(Ga)As quantum dots*, Physical Review B, Vol. 70, No. 23, 235337 (2004)

89. L. H. Thomas, *The Kinematics of an Electron with an Axis*, Philosophical Magazine, Vol. 3, pp. 1-22 (1927)

90. M. Valín-Rodríguez, A. Puente, L. Serra, and E. Lipparini, *Spin switching in semiconductor quantum dots through spin-orbit coupling*, Physical Review B, Vol. 66, No. 16, 165302 (2002)

91. M. Valin-Rodriguez, A. Puente, and L. Serra, Spin splitting and precession in quantum dots with spin-orbit coupling: The role of spatial deformation, Physical Review B, Vol. 69, No. 8, 085306 (2004)

92. W. Sheng and P. Hawrylak, *Spin polarization in self-assembled quantum dots*, Physical Review B, Vol. 73, No. 12, 125331 (2006)

93. A. Wojs, P. Hawrylak, S. Fafard, and L. Jacak, *Electronic structure and magneto-optics of self-assembled quantum dots*, Physical Review B, Vol. 54, No. 8, pp. 5604-5608 (1996)

94. I. Vurgaftman, J. R. Meyer, and L. R. Ram-Mohan, *Band parameters for III--V compound semiconductors and their alloys*, Journal of Applied Physics, Vol. 89, No. 11, pp. 5815-5875 (2001)

95. M. A. Cusack, P. R. Briddon, and M. Jaros, *Absorption spectra and optical transitions in InAs/GaAs self-assembled quantum dots*, Physical Review B, Vol. 56, No. 7, pp. 4047-4050 (1997)

96. S. Zwerdling, B. Lax, L. M. Roth, and K. J. Button, *Exciton and magneto-absorption of the direct and indirect transitions in germanium*, Physical Review, Vol. 114, No. 1, pp. 80-89 (1959)

97. L. M. Roth, B. Lax, and S. Zwerdling, *Theory of optical magneto-absorption effects in semiconductors*, Physical Review, Vol. 114, No. 1, pp. 90-104 (1959)

98. G. Lommer, F. Malcher, and U. Rossler, *Spin splitting in semiconductor heterostructures for $B \to 0$*, Physical Review Letters, Vol. 60, No. 8, pp. 728-731 (1988)

99. J. Luo, H. Munekata, F. F. Fang, and P. J. Stiles, *Effects of inversion asymmetry on electron energy band structures in GaSb/InAs/GaSb quantum wells*, Physical Review B, Vol. 41, No. 11, pp. 7685-7693 (1990)

100. S. D. Ganichev, V. V. Bel'kov, L. E. Golub, E. L. Ivchenko, P. Schneider, S. Giglberger, J. Eroms, J. De Boeck, G. Borghs, W. Wegscheider, D. Weiss, and W. Prettl, *Experimental separation of Rashba and Dresselhaus spin splittings in semiconductor quantum wells*, Physical Review Letters, Vol. 92, No. 25, 256601 (2004)

101. F. Debray, H. Jongbloets, W. Joss, G. A.-M. Martinez, G., E. A.-M. Mossang, E., P. A.-P. Petmezakis, P., J. C. A.-P. Picoche, J.C., A. A.-P. Plante, A., P. A.-R. Rub, P., P. A.-S. Sala, P., and P. A.-W. Wyder, P., *The Grenoble High Magnetic Field Laboratory as a USER FACILITY*, IEEE Transactions on Applied Superconductivity, Vol. 12, No. 1, pp. 674-677 (2002)

Appendix A: Images of Magnet Setup

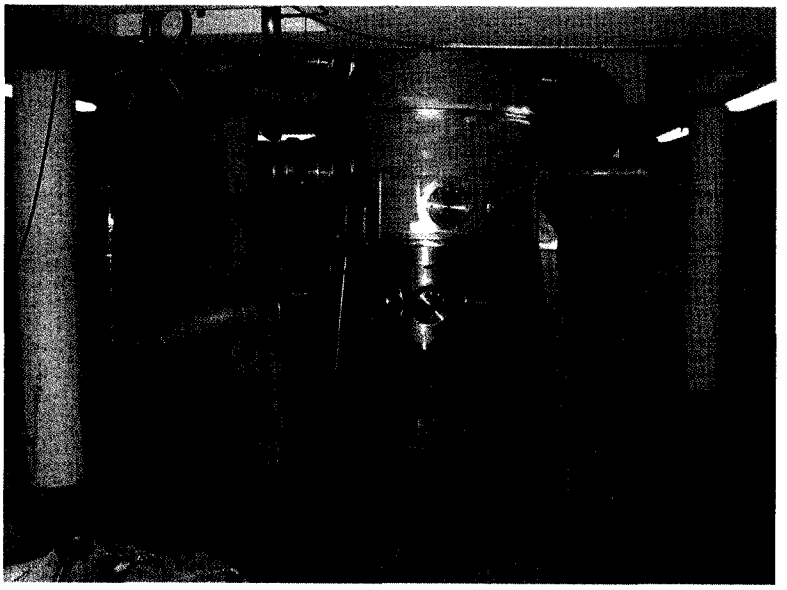

Magnet casing with water pipes (basement level)

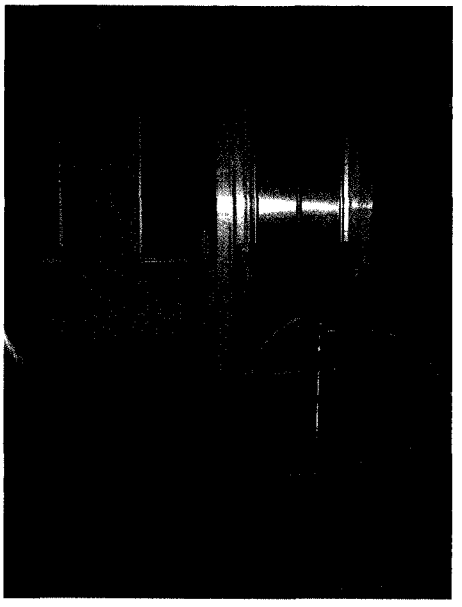

Top of cryostat with tube inserted in magnet (floor level)

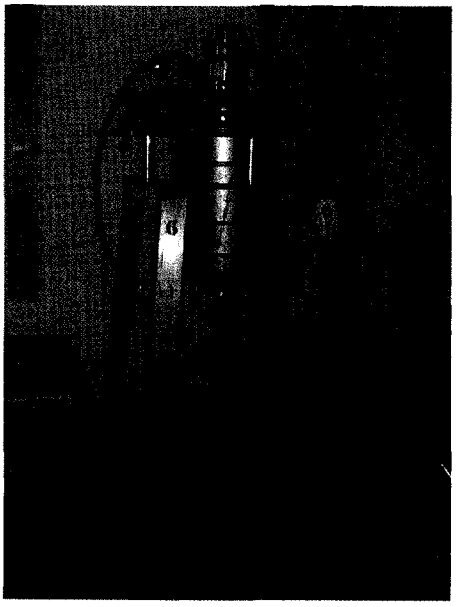

Liquid helium cryostat

Three centrifugal pumps deliver a maximum water flow rate of 1000 m^3/h to cool the resistive magnet. Demineralised water in a closed circuit is used to minimize leakage current and optimize the field stability. The magnet can yield steady fields up to 30 T with a power consumption of 20 MW.[101]

Appendix B: Codes for Data Processing

```
// Script code for smoothing + 2nd derivative

%B=Deriv20; //enter worksheet name
N=28; //number of columns to be processed (alternate X and Y)
for(ii=1;ii<N;ii+=2){
%D=%(%B,@C,ii); //returns the ii-th column name
%A=%(%B,@C,ii+1);
curve.x$=%B_%D; // x-column
curve.data$=%B_%A; // y-column
curve.result$=%B_%A;
curve.smoothpts=20;  //number of smooth points
curve.i1=1; //enter starting and ending number of rows to process
curve.i2=2405; //set number of rows
curve.adjave(); // smoothing
curve.derivdeg=1; //1-first derivative, 2- second derivative
curve.deriv();
curve.adjave();
curve.deriv();
curve.adjave();
%B_%A=-%B_%A};  //adjust the sign of the second derivative
type -b "the calculation is done";


// Script code for smoothing only

%B=SmoothOnly20; //enter worksheet name
N=28; //number of columns to be processed (alternate X and Y)
for(ii=1;ii<N;ii+=2){
%D=%(%B,@C,ii); //returns the ii-th column name
%A=%(%B,@C,ii+1);
curve.x$=%B_%D; // x-column
curve.data$=%B_%A; // y-column
curve.result$=%B_%A;
curve.smoothpts=20;  //number of smooth points
curve.i1=1; //enter starting and ending number of rows to process
curve.i2=2405; //set number of rows
curve.adjave()}; // smoothing
type -b "the calculation is done";


// Script code for averaging overlaping data sets

%D=P250mW; //enter name of worksheet with original data (columns in order)
%E=P250; //enter name of worksheet for results (2 columns)
N1=1; N2=10; //number of columns to be processed (alternate X and Y)
R1=1; R2=508; //number of rows to be processed
R=33; //number of rows to be averaged

for(jj=N1;jj<=N1+1;jj+=1){
for(ii=R1;ii<=(R2-R);ii+=1){
%(%E,jj,ii)=%(%D,jj,ii);
};
for(ii=R2+1-R;ii<=R2;ii+=1){
T=R2-ii;
L=%(%D,jj,ii)*(T+0.5)/R;
H=%(%D,jj+2,ii-(R2-R))*(R-T-0.5)/R;
%(%E,jj,ii)=(L+H);
};
};

for(jj=(N1+2);jj<=(N2-2);jj+=2){
for(ii=R+1;ii<=(R2-R);ii+=1){
%(%E,1,ii+(jj-1)*(R2-R)/2.0)=%(%D,jj,ii);
};
for(ii=R2+1-R;ii<=R2;ii+=1){
```

```
T=R2-ii;
L=%(%D,jj,ii)*(T+0.5)/R;
H=%(%D,jj+2,ii-(R2-R))*(R-T-0.5)/R;
%(%E,1,ii+(jj-1)*(R2-R)/2.0)=(L+H);
};
};

for(jj=(N1+3);jj<=(N2-2);jj+=2){
for(ii=R+1;ii<=(R2-R);ii+=1){
%(%E,2,ii+(jj-2)*(R2-R)/2.0)=%(%D,jj,ii);
};
for(ii=R2+1-R;ii<=R2;ii+=1){
T=R2-ii;
L=%(%D,jj,ii)*(T+0.5)/R;
H=%(%D,jj+2,ii-(R2-R))*(R-T-0.5)/R;
%(%E,2,ii+(jj-2)*(R2-R)/2.0)=(L+H);
};
};

jj=(N2-1);
for(ii=R+1;ii<=R2;ii+=1){
%(%E,1,ii+(jj-1)*(R2-R)/2.0)=%(%D,jj,ii);
};

jj=N2;
for(ii=R+1;ii<=R2;ii+=1){
%(%E,2,ii+(jj-2)*(R2-R)/2.0)=%(%D,jj,ii);
};

type -b "the calculation is done";


// Script code for removing spikes

%D=P135; //enter name of worksheet with original data (2 columns)
%E=P135spikes15; //enter name of worksheet for results (2 columns)
R1=1; R2=2408; //number of rows to be processed
%V=15; //maximum variation allowed

%(%E,1,R1)=%(%D,1,R1);
%(%E,2,R1)=%(%D,2,R1);
%lastY=%(%D,2,R1);
jj=R1;

for(ii=R1+1;ii<=R2;ii+=1){

%dif=abs(%(%D,2,ii)-%lastY);

if(%dif<%V){
jj+=1;
%(%E,1,jj)=%(%D,1,ii);
%(%E,2,jj)=%(%D,2,ii);
%lastY=%(%D,2,ii);
};
};

type -b "the calculation is done";
```

Appendix C: Code for Spin-Orbit Model Calculations

```
/* Spin splitting in QDs with SO coupling and spatial deformation of dot.
  Noninteracting single particles model from M. Valin-Rodriguez et al., PRB 69, 085306 (2004).
  This version calculates the energy difference between the electron state (including SO coupling and the hole sate (without SO coupling).
  A grid search algorithm is used to optimize the model parameters.
  Author: Martin Vachon */


#include <iostream>
#include <fstream>
#include <math>
#include <string>
#include <stdlib>
using namespace std;

double** getexp();
double diffcal(double **data, double **exp);
double** energycal(float me, float ge, float mh, float gh, float lambda, float hwe, float hwh, float beta, float Eo, int Enum, int Bnum, float
Bint);
double omegacal (float B, float me, fbat lambda, int k, int s, float wx, float wy);
void writeheaders (int Enum);
void writedata (double **data, int Enum, int Bnum);


int main () {

 // Bnum = number of magnetic fields (number of rows in data array = Bnum)
 // Bint = interval between magnetic fields (B starts at 0)
 // Enum = number of energy states (number of columns in data array = Enum + 1)
 // Energy states go from (0,0,-) to (0,0,+) to (0,1,-) ... until Enum is reached
 // +/- is for spin up/down electron
 // data = array containing calculated data
 // exp = array containing experimental data

 int Bnum, Enum;
 float Bint;
 double **data; // must adjust array size in function energycal
 double **exp;
 double diff;
 Bnum = 27;
 Bint = 1.0;
 Enum = 22;

 // me = Electron effective mass (units of m)
 // ge = Electron g-factor
 // lambda = SO intensity (from coupling constants)
 // lambda = lambdaD^2 - lambdaR^2 (eV^2 * m^2)
 // hw = Centroid value or h(wx+wy)/2 (energy spacing between shells) (eV)
 // beta = Deformation factor (beta = wy / wx)

 float me, ge, mh, gh, lambda, hwe, hwh, beta, Eo, muB;
 me = 0.067;
 ge = 1.5;
 hwe = 0.0353;
 mh = 0.59;
 gh = 0.0;
 hwh = 0.0074;
 lambda = 15.2e-22;
 beta = 0.95;
 Eo = 1238;

 double a[6][100];
 // The number of rows in the array is chosen arbitrarily large to include
 // all iteration values.

 a[0][0]=ge,a[1][0]=lambda,a[2][0]=hwe,a[3][0]=hwh,a[4][0]=beta,a[5][0]=Eo;
```

```
// Initial parameter values.

double a1, a2;
// Different values of the same parameter during iterations.
double X1, X2, X3=0, Xswitch, Xlast=10;
// Values of chi-squared during iterations.
double delta;
// Iteration step for current parameter.
// The step is chosen to be 1/10000 of the parameter value before iterations.

int i, j, ite;

exp = getexp();

// Begin grid search algorithm
for (j = 1 ; j < 100 && fabs(Xlast-X3) > 5; j++) {

Xlast = X3;
cout << "j = " << j << endl;

for (i = 0 ; i < 6 ; i++) {
  a[i][j] = a[i][j-1];
}

for (i = 0 ; i < 6 ; i++) {

delta = a[i][j]/1000;

data = energycal(me,a[0][j],mh,gh,a[1][j],a[2][j],a[3][j],a[4][j],a[5][j],Enum,Bnum,Bint);
X2 = diffcal(data,exp);

cout << "initial chi-squared =" << X2 << endl;

a2 = a[i][j];
a[i][j] = a[i][j] + delta;

data = energycal(me,a[0][j],mh,gh,a[1][j],a[2][j],a[3][j],a[4][j],a[5][j],Enum,Bnum,Bint);
X3 = diffcal(data,exp);

if ( X3 > X2 ) {
  delta = -delta;
  a2 = a[i][j];
  a[i][j] = a[i][j] + delta;
  Xswitch = X2;
  X2 = X3;
  X3 = Xswitch;
}

ite = 0;

while ( X3 < X2 ) {

  a1 = a2;
  a2 = a[i][j];
  a[i][j] = a[i][j] + delta;

  X1 = X2;
  X2 = X3;

  data = energycal(me,a[0][j],mh,gh,a[1][j],a[2][j],a[3][j],a[4][j],a[5][j],Enum,Bnum,Bint);
  X3 = diffcal(data,exp);

  if (ite > 500) {
    cout << "Unsuccessful iteration" << endl;
    break;
  }

ite++;
}
```

```
 a[i][j] = a[i][j] - delta * ( (X3-X2) / (X3-2*X2+X1) + 1/2 );

 data = energycal(me,a[0][j],mh,gh,a[1][j],a[2][j],a[3][j],a[4][j],a[5][j],Enum,Bnum,Bint);
 X3 = diffcal(data,exp);

 cout << "ite =" << ite << endl;
 cout << "a" << i << " = " << a[i][j] << endl;
 cout << "chi-squared =" << X3 << endl;

 }
 }

 writeheaders(Enum);
 writedata(data,Enum,Bnum);

 return 0;
}


double** getexp() {

 // Function getexp creates an array with the experimental data

 double **exp;
 exp = new double*[27];
 int i;

 double temp0[14] = {0,1316.36,1320.13,1322.86,1326.37,1363.35,0,1368.99,1368.99,0,0,0,0,0};
 exp[0] = new double[14];
 for ( i = 0 ; i < 14 ; i++ ) {
  exp[0][i] = temp0[i];
 }
 double temp1[14] = {0,1316.54,1319.84,1323.98,1326.43,1359.94,0,1369.24,1369.24,1366.64,0,0,0,0};
 exp[1] = new double[14];
 for ( i = 0 ; i < 14 ; i++ ) {
  exp[1][i] = temp1[i];
 }
 ...
 double temp26[14] = {1290.68,1312.73,1312.73,1355.93,1363.22,1337.23,1337.23,1382.1,1389.27,0,0,1363.22,1363.22,1386.78};
 exp[26] = new double[14];
 for ( i = 0 ; i < 14 ; i++ ) {
  exp[26][i] = temp26[i];
 }

 return exp;
}


double diffcal(double **data, double **exp) {

 // Function diffcal calculates the sum of the squares of (exp points - calculated points)

 double diff;
 int i;

 diff = 0.0;

 for ( i = 0 ; i <= 26 ; i++ ) {
  if ( exp[i][0] != 0 ) {
   diff = diff + pow((data[i][2]-exp[i][0]),2);
  }
 }
 for ( i = 0 ; i <= 26 ; i++ ) {
  if ( exp[i][1] != 0 ) {
   diff = diff + pow((data[i][4]-exp[i][1]),2);
  }
 }
 ...
 for ( i = 0 ; i <= 26 ; i++ ) {
  if ( exp[i][13] != 0 ) {
```

```
    diff = diff + pow((data[i][22]-exp[i][13]),2);
   }
  }

  return diff;
}


double** energycal(float me, float ge, float mh, float gh, float lambda, float hwe, float hwh, float beta, float Eo, int Enum, int Bnum, float
Bint) {

  // Function energycal calculates the emission energy for specified parameters

  // hbar = Planck's constant (eV * s)
  // muB = Bohr magneton (eV / T)

  float hbar, muB;
  hbar = 6.5821e-16;
  muB = 5.7884e-5;

  // B = Magnetic field in z direction
  // N1,N2 = Number of quanta in each oscillator
  // s = Spin state (+1 or -1)
  // shell = Number of states in shell
  // state = Counter for states
  // data = Array containing calculated energies

  float B;
  int N1, N2, s, shell, state;
  double **data;
  double Ee, Eh;
  data = new double*[27]; // Number of rows

  double wxe, wye, wxh, wyh;

  wxe = 2 * hwe / ( hbar * ( 1 + beta ) );
  wye = beta * wxe;

  wxh = 2 * hwh / ( hbar * ( 1 + beta ) );
  wyh = beta * wxh;

  for ( int i = 0 ; i < Bnum ; i++ ) {
   data[i] = new double[23]; // Number of colomns
   B = i * Bint;
   data[i][0] = B;
   s = 1;
   shell = 0;
   state = 0;
   for ( int j = 1 ; j <= Enum ; j++ ) {
    s = s * -1;
    state = state + 1;
    if ( state % (shell+1) == 0 ) {
     shell = shell + 2;
     N1 = -1;
     state = 1;
    }
    if ( (j+1) % 2 == 0 ) {
     N1 = N1 + 1;
     N2 = (shell/2) - N1 - 1;
    }
    Ee = Eo + 1000 * ( (N1 + 0.5)*hbar*omegacal(B,me,lambda,1,s,wxe,wye) + (N2 + 0.5)*hbar*omegacal(B,me,lambda,2,s,wxe,wye) +
0.5*s*ge*muB*B );
    Eh = -1000 * ( (N1 + 0.5)*hbar*omegacal(B,mh,0.0,1,-s,wxh,wyh) + (N2 + 0.5)*hbar*omegacal(B,mh,0.0,2,-s,wxh,wyh) +
0.5*s*gh*muB*B );
    data[i][j] = Ee - Eh;
   }
  }
  return data;
}
```

```
double omegacal (float B, float me, fbat lambda, int k, int s, float wx, float wy) {

 // Function omegacal calculates the value of capital omega for specified values of k and s

 // k = Oscillator number (k = 1 or 2; (1,2))
 // e = Electron charge (C)
 // m = Electron mass (kg)
 // hbar = Planck's constant (eV*s)

 float e, m, hbar;
 double w, omega, wx2, wy2, w2, w3;
 e = 1.6022e-19;
 m = 9.1094e-31;
 hbar = 6.5821e-16;

 w = ( e * B / ( me * m ) ) + ( lambda * 2 * me * m * s / pow(hbar,3) ) / e;

 w2 = pow(w,2);
 wx2 = pow(wx,2);
 wy2 = pow(wy,2);
 w3 = wx2 + wy2 + w2;

 if ( k == 1 ) {
  omega = sqrt( w3 + sqrt( pow(w3,2) - 4 * wx2 * wy2 ) ) / sqrt(2);
 }
 else if ( k == 2 ) {
  omega = sqrt( w3 - sqrt( pow(w3,2) - 4 * wx2 * wy2 ) ) / sqrt(2);
 }

 return omega;
}


void writeheaders (int Enum) {

 // Function writeheaders writes data headers to the EvsB.txt file

 // N1,N2 = Number of quanta in each oscillator
 // s = Spin state (+1 or -1)
 // shell = Number of states in shell
 // state = Counter for states
 // Hstring = State in the format (N1 N2 s)

 int N1, N2, s, shell, state;
 int N1temp, N2temp, stemp;
 char Hstring[8];

 s = 1;
 shell = 0;
 state = 0;

 ofstream myfile("EvsB.txt");

 if (myfile.is_open()) {
  myfile << "B Field";
  for ( int j = 1 ; j <= Enum ; j++ ) {
   s = s * -1;
   state = state + 1;
   if ( state % (shell+1) == 0 ) {
    shell = shell + 2;
    N1 = -1;
    state = 1;
   }
   if ( (j+1) % 2 == 0 ) {
    N1 = N1 + 1;
    N2 = (shell/2) - N1 - 1;
   }
   cout << N1 << N2 << s << "\n";
   N1temp = N1;
```

```
    N2temp = N2;
    stemp = s;
    strcpy (Hstring,"(");
    char buf[5];
    itoa(N1temp, buf, 10);
    strcat (Hstring,buf);
    strcat (Hstring," ");
    itoa(N2temp, buf, 10);
    strcat (Hstring,buf);
    strcat (Hstring," ");
    itoa(stemp, buf, 10);
    strcat (Hstring,buf);
    strcat (Hstring,")");
    myfile << ",";
    myfile << Hstring;
   }
   myfile << "\n";
   myfile.close();
  }
  else {
   cout << "Unable to open file to write data";
  }
}


void writedata (double **data, int Enum, int Bnum) {

 // Function writedata writes data points to the EvsB.txt file

 ofstream myfile;
 myfile.open ("EvsB.txt", ios::out | ios::app);

 if (myfile.is_open()) {
  for ( int B = 0 ; B < Bnum ; B++ ) {
   myfile << data[B][0];
   for ( int i = 1 ; i <= Enum ; i++ ) {
    myfile << ",";
    myfile << data[B][i];
   }
   myfile << "\n";
  }
  myfile.close();
 }
 else {
  cout << "Unable to open file to write data";
 }
}
```